

REMOTE
OPTICAL EXCITATION AND SENSING
OF
STRUCTURAL VIBRATION



A thesis submitted by
ALEKSEI RYBKIN
for
the degree of
Master of Science

Optical Technology Research Laboratory
Victoria University of Technology
1998



FTS THESIS

621.3678 RYB

30001005477296

Rybkin, Aleksei

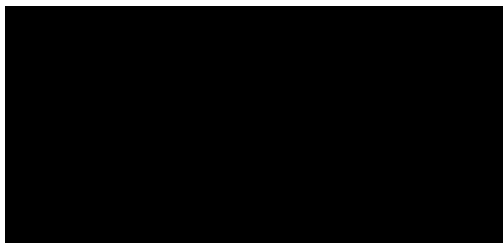
Remote optical excitation
and sensing of structural
vibration

Declaration

I, Aleksei Rybkin, declare that the thesis titled,

REMOTE OPTICAL EXCITATION AND SENSING OF STRUCTURAL

VIBRATION, is my own work and has not been submitted previously, in whole or in part, in respect of any other academic award.



A.Rybkin, dated the 8th of December 1998.

Acknowledgments

I would most like to thank my supervisor, former Director of Optical Technology Research Laboratory at Victoria University of Technology, Professor David Booth, for guidance, support and discussion in all matters of this research. I would like to thank my former supervisor Dr. Nigel Perry for guidance and encouragement at the early stage of this work. I wish to thank all the other academics, technicians, administrative staff and fellow postgraduate students in the department for their willing assistance and friendship.

I am grateful to Victoria University of Technology for the provision a Postgraduate Scholarship.

Finally, I would like to pay tribute to my family for their understanding and support throughout my research.

Abstract

This thesis is concerned with non-contact techniques for optical excitation of mechanical vibrations in structures and with the use of non-contact fibre optic interferometers for the measurement of parameters which characterise these mechanical vibrations. Taken together, the excitation and sensing systems provide a method for fully remote non-destructive testing (NDT) of structures, which can sense changes in any parameter which affects the vibrations. The technique is applicable to a wide range of structures but is particularly suitable for use with delicate structures or structures for which the use of conventional excitation and sensing techniques would load the structure and modify the parameters being measured. The ultimate usefulness of this NDT technique depends on the accuracy with which important vibrational parameters such as resonant frequency and damping can be measured.

In this thesis, transverse mechanical vibrations are thermoelastically excited in structures using sinusoidally modulated 800 nm laser diodes with peak-to-peak powers of the order of 25 mW. The vibrations are sensed using a modified form of a fibre optic Mach-Zehnder interferometer, which uses a 2 mW He-Ne laser source. The interferometer senses changes in optical path between the partially reflecting unpolished surface of the vibrating structure and the end of an optical fibre placed at a distance of 100 - 150 mm from the surface.

The measurements have been made using a very lightly damped structure (a high Q cantilever) under three separate environmental noise conditions. Data was collected for the resonant frequency and also for the related loss-dependent parameters of half-power bandwidth and damping factor for the first 5 vibrational modes. A number of ways of making these measurements were tried and the advantages and disadvantages of each were identified. The thesis identifies the accuracy with which each of the vibrational mode parameters can be determined and the origin of the effects, which are responsible for the ultimate limitation on this accuracy.

Table of Contents

	Page
Declaration	I
Acknowledgments	II
Abstract	III
Table of Contents	V

Chapter 1: Introduction

1.1	Non-destructive testing of structures.....	1-2
1.2	Vibration analysis in NDT.....	1-3
1.3	The excitation of mechanical vibrations using laser sources.....	1-6
1.4	The Aim of the research.....	1-8

Chapter 2: Review of previous work and vibration analysis

background

2.1	Introduction.....	2-2
2.2	Summary of previous works.....	2-3
2.3	Sensing systems.....	2-10
2.4	Thermoelastic bending of a structure.....	2-17
2.5	Vibration analysis background.....	2-19
2.5.1	Differential equation of motion for elastic bar.....	2-22
2.5.1.1	Resonance frequency and temperature shift.....	2-28
2.5.2	Equation of motion for Single Degree of Freedom structure	2-29
2.5.2.1	Response function for Single Degree of Freedom system....	2-34
2.5.2.2	Energy flow in an oscillator.....	2-38

Chapter 3: Experimental arrangement

	Page
3.1 Introduction.....	3-2
3.1.1 The set-up diagram and description.....	3-2
3.2 Optical excitation system.....	3-4
3.2.1 Diode Laser for photothermal excitation of vibrations.....	3-4
3.2.2 Power Supply and Temperature Controller.....	3-5
3.3 Optical detection system.....	3-8
3.3.1 Interferometric sensor and homodyne technique.....	3-9
3.3.2 Signal processing.....	3-14
3.3.3 Detection electronics circuitry and feedback control operation.....	3-15
3.4 The Interferometer calibration procedure and performance.....	3-19

Chapter4: Experimental results and discussion

4.1 Introduction.....	4-2
4.1.1 Response function in vibration analysis and processing of measured data.....	4-3
4.1.2 The accuracy of resonant frequency measurement.....	4-4
4.2. Description of the procedure used for measurements.....	4-6
4.3 Response measurements with a rigid cantilever securely fastened to the mounting bench.....	4-10
4.3.1 Response measurements under favourable laboratory (Conditions A).....	4-11
4.3.1.1 Resonance measurements for Mode1.....	4-12
4.3.1.2 Resonance measurements for Modes 2-5.....	4-19
4.3.1.3 Vibration parameters obtained using Lorentzian fits for Modes 1-5.....	4-24
4.3.1.4 Decay time measurements by waveform sampling: Modes 1-3.....	4-26

	Page
4.3.1.5 Variations in resonant frequency due to temperature changes.....	4-35
4.3.2 Daytime measurements under less favourable laboratory conditions (Conditions B and C).....	4-36
4.4 Measurements with increased damping.....	4-44
4.5 Summary.....	4-50

Chapter5: Conclusion

5.1 Conclusion.....	5-2
---------------------	-----

List of symbols.....	S-1
-----------------------------	------------

References.....	R-1
------------------------	------------

Chapter 1

INTRODUCTION

Content:	Page
1.1 Non-destructive testing of structures.....	1-2
1.2 Vibration analysis in NDT.....	1-3
1.3 Excitation of mechanical vibrations using laser sources.....	1-6
1.4 The Aim of the research.....	1-8

1.1 Non-destructive testing of structures

Components of machines, vehicles and structures are frequently subjected to repeated loads, also called cyclic loads, and the resulting cyclic stresses can lead to microscopic physical damage to materials involved. Even at stresses well below a given material's ultimate strength, this damage can accumulate with continued cycling until it develops into a crack or other damage that leads to failure of the component. This process of accumulating damage and finally failure due to cyclic loading is called fatigue (Dowling 1993).

The costly and common causes of mechanical failure in industry are excessive deformation and cracking in components due to material inhomogeneities. When viewed at a sufficiently small scale, all materials are anisotropic and inhomogeneous. As a result of such non-uniform microstructure, stresses are distributed in a non-uniform manner and regions of most severe stress are usually the points where fatigue damage starts. It is frequently necessary to check and test the article during its service life in order to monitor changes, such as possible fatigue damage.

The types of test used can be broadly classified into two categories:

- (a) Tests to establish the properties of the material, and
- (b) Tests to determine the structural integrity of the material or component.

The tests in the first category are generally of a destructive type. They are performed on samples of a material and the test-piece is damaged or broken in the process. The tests in the second category are of a non-destructive nature and are

used to detect the presence of internal or surface flaws in a material or a component. By their very nature, these tests do not damage the parts being tested. The rapid growth in the use of non-destructive testing methods and techniques in the past years has resulted from demands by industry for improved quality. Nearly every property of the materials to be inspected has been made the basis for some method or technique of non-destructive testing. The coin-tap test (McGonnagle, 1961) is probably the best known local method of non-destructive testing. The region of structure to be tested is tapped with the coin and the operator listening to the resulting sound can detect the difference in 'ringing' between good and defective structures. The defective areas sound duller than good areas due to resonant frequency shifts and more rapid sound decay due to acoustic losses and stiffness changes at the defect.

1.2 Vibration analysis in NDT

Objects have a set of natural resonant mechanical vibration frequencies. These natural frequencies are functions of the size, shape, mass, elastic properties, and mode of vibration produced in the specimen. For specimens of simple shape, it is possible to derive relations between the various dimensional and structural parameters and the frequencies for simple modes of vibration. When the specimen has a complex shape, such relations cannot be derived mathematically and an empirical relationship is normally found (Bray and McBride 1992).

Vibrational analysis for non-destructive testing purposes is called modal analysis. Many of the techniques developed in the field of modal analysis and dynamic property measurement methods over the past 20 years have sought to measure the

modal frequencies of a structure accurately and to explain observed shifts in those frequencies in terms of defect or damage to the structure. There are two practical limitations in the usual application of modal analysis for non-destructive testing (Ewins, 1995):

- (a) Imprecise impulsive excitation techniques (traditionally, impulsive heating, impact or shaking) which allow the energy delivered to the test structure to vary between successive trials.
- (b) Invasive vibration sensing or excitation methods which significantly load lightweight structures by physical contact during vibration. These can require special preparation or modification of the structure's surface and can alter the modal frequencies being measured.

The natural mechanical vibration frequencies are a function of shape, physical properties and boundary conditions. The dependence on shape includes the geometrical design of structure and the dimensional factors such as length, width and thickness. The relevant physical properties include modulus of elasticity, density and Poisson's ratio for the material of the structure. Boundary conditions refer to the type of support or the way in which the structure is constrained. Changes in any of the above properties of a structure will generally cause a change in natural frequency of the modal vibrations. Detection of these frequency shifts can be used to reveal underlying changes in one or more of these structural properties (Bray and McBride 1992).

Many types of flaws, defects and damage in structures of different shapes directly affect its stiffness or elasticity (Duggan 1964). A loss of stiffness is detectable, as a decrease in the observed resonance frequency of the structure for modes, which do not have a node at the damage location.

The NDT technique, in which the test structure is caused to vibrate in one of its natural or resonant mechanical modes, is known as resonance vibration testing. This resonance vibration testing generally involves measurement of either the natural frequencies of the structure being evaluated or the rate of attenuation (or damping) of vibrations in the structure (Bray and McBride 1992). The data obtained from these tests are a function of the physical configuration and composition of the sample and can therefore be analysed for property determination and flaw detection purposes. Conventionally the excitation is usually accomplished by mechanical coupling of the test structure to a subsidiary vibrator, such as a piezoelectric transducer or an electromagnetic (or electrodynamic) vibrator. The electromagnetic methods are convenient for exciting small vibrations in magnetic materials, and the induced current methods are useful for non-magnetic metals having good conductivity. Since no physical contact is required between the test structure and excitation system, the structure is free to vibrate at its own natural frequency. For magnetic material, the region of maximum vibration amplitude is positioned to bridge the poles of an electromagnetic coil carrying alternating current. The resonant frequency may be found by varying the frequency of the alternating current to obtain maximum vibration amplitude. Non-magnetic metals with good conductivity can be set into vibration by passing an alternating

current through a coil placed near the test sample. The small induced currents in the sample produce a reaction between the magnetic field of the coil and that of the induced current. This reaction produces an alternating force on the test sample and causes it to vibrate. Continuous excitation has several advantages for resonant vibration testing of materials. It permits:

- a) Detection of the natural frequency of vibration in structures (including those having high damping)
- b) Examination of the mode of vibration with sound or vibration pick-ups
- c) Excitation of a single natural frequency at one time so that the fundamental frequency is not masked by other modes or overtones
- d) Less critical attention to the damping introduced to the supports.

Piezoelectric accelerometers, capacitance and strain gauges are the most commonly used conventional devices to measure vibration parameters (Allocca and Stuart 1984).

1.3 Excitation of mechanical vibrations using laser sources

The advent of the laser has produced a light source of high enough power that considerable heating effects have been generated when the light is absorbed. Lasers have the ability to produce a very wide range of powers, pulsewidths and wavelengths. Since this power can be delivered to a very small area of a target,

lasers provide very flexible sources of localised excitation and heating. When a laser beam of high power density ($\sim 10^7$ W/cm²) impinges on an opaque metal surface, the light energy is absorbed in a thin layer of material. The absorbed light causes a rapid rise in the surface temperature to its vaporisation temperature in a time short compared to the pulse duration. A small portion of the surface material is rapidly ejected as a molten spray and vapour (Ready J.F., 1965). This results in an impulsive reaction to the irradiated structure, which causes it to oscillate. The disadvantages of the ablative laser excitation are that significant damage can be done to the surface of the structure and the impulse generated by the excitation may not be repeatable if there is cumulative damage.

Philp and Booth (1994) found that the simple structure could be excited by a laser beam of sub-ablative power density without any damage to the irradiated surface at all. It has been shown that the heat generated at the surface due to the absorption of light even lower than the material ablation threshold causes a localised thermal expansion, which in turn causes a localised bending moment. This localised bending moment is sufficient enough to induce time dependent angular displacement or flexure of a structure along the biggest dimension. The vibration amplitude of the structure is normally smaller than the amplitude excited by the ablative technique because the absorbed energy is simply lower. The relatively large structure (as a 300 mm×12 mm×3 mm cantilever) has been successfully driven to mechanical vibration using repetitive pulses from a low-power diode laser. It was shown that the structure could be set in steady state forced vibration if the modulation frequency of the diode laser was matched to one of the natural

resonance frequencies of the structure. This required that the excitation point at the surface be positioned at an antinode of the bending moment profile for the selected vibration mode.

Since the magnitude of structural response depends critically on the difference between the excitation and resonant frequency, by measuring the displacement amplitude as function of driving frequency in the resonance region the response curve of the vibration mode can be plotted. The resonance frequency is identified as a peak of the response curve with maximum amplitude, which corresponds to the natural resonance frequency of a particular mode for structure. The half-power bandwidth can be also determined from the response curve of a particular mode by obtaining the damping ratio. The accuracy of this technique depends on how accurately the peak magnitude can be measured and the frequency resolution of equipment obtainable for the measurement. The optical excitation and optical sensing technique permits:

- (a) Remote non-contact excitation and detection of very small displacements
- (b) Low cost support instrumentation.

1.4 The Aim of the research

The purpose of the work described in this thesis is to extend the work of Philp (1993) by carrying out a more careful set of measurements of the modal frequencies of some suitable structure in order to determine just how accurately the

modal frequencies can be determined using a well-designed experimental system. The accuracy with which modal frequencies can be measured will ultimately determine the limitations of the optical excitation and sensing technique for non-destructive testing applications.

Philp's modal frequency measurements were found to be limited by the accuracy of the simple oscillator used to drive the laser diode excitation system (± 0.5 Hz). The experimental arrangement used in this thesis will use a very high stability oscillator to try to remove this limitation and then try to see exactly what physical effects are responsible for any limitation to the ultimate modal frequency resolution, which can be achieved. Such limitations could arise from the fundamental Q of the mechanical resonance being excited (dependent on vibrational energy loss) or could arise from extraneous environmental vibrational noise effects, such as those produced by building vibration, acoustic noise and air currents, which can shift or broaden the measured mechanical resonance frequencies.

Clearly the limitations will be a function of not just the magnitude of the noise but also the magnitude of the signal (ie signal to noise ratio) and the overall sensitivity of the measurement system. Rather than attempt to improve performance by brute force methods such as using laser powers which are orders of magnitude greater than those used by Philp, we have chosen to continue to use moderate power laser diodes for excitation as these are cheap, simple to use and compatible with highly practical experimental systems. We have, however, chosen to increase the sensitivity of the interferometric detection system as the one used by Philp was

clearly capable of significant improvement without any change to the basic practicality of the system. A new interferometer system has been constructed which is based on the more common shorter-wavelength He-Ne transition at 633 nm and uses couplers designed for this wavelength together with lower noise silicon detectors. The change of wavelength alone gives an increase in displacement sensitivity of more than a factor of two compared to the 1523 nm laser source used by Philp. The interferometer has also been improved by the use of lower noise electronic circuitry. The overall effect of these changes has been to improve the noise equivalent displacement of the system by roughly an order of magnitude while at the same time increasing the bandwidth by a similar factor.

The specific aims of this research are to assess the suitability of low-power resonant optical excitation and sensing systems for modal analysis applications by:

- Constructing an optical system suitable for making non-contact measurements of the modal frequencies and other modal oscillation parameters of transverse mechanical vibrations in small to medium sized structures. This system will comprise:
 - (a) A modulated optical beam with an accurately controllable modulation frequency.
 - (b) A sensitive fibre optic interferometer.
 - (c) A low-noise signal detection and recording system.

- Investigating the advantages and disadvantages of alternative ways of making measurements of modal oscillation parameters, which can be used to characterise a structure (modal frequency, resonance bandwidth and damping).
- Using the optical system to determine the accuracy with which measurements can be made of modal oscillation parameters for a high- Q structural resonance.
- Determining the origin of the effects, which are responsible for the ultimate limitations with which modal oscillation parameters can be measured.

This optical excitation technique may be used to supplement the resonance vibration testing in the field of NDT.

Chapter 2

REVIEW OF PREVIOUS WORK

AND

VIBRATION ANALYSIS BACKGROUND

Content	Page
2.1 Introduction.....	2-2
2.2 Summary of previous works.....	2-3
2.3 Sensing systems.....	2-10
2.4 Thermoelastic bending of a structure.....	2-17
2.5 Vibration analysis background.....	2-19
2.5.1 Differential equation of motion for elastic bar.....	2-22
2.5.1.1 Resonance frequency and temperature shift.....	2-28
2.5.2 Equation of motion for Single Degree of Freedom structure	2-29
2.5.2.1 Response function for Single Degree of Freedom system....	2-34
2.5.2.2 Energy flow in an oscillator.....	2-38

2.1 Introduction

Bell (1880) first discovered that when a periodically interrupted beam of sunlight shines on a solid in an enclosed cell, an audible sound could be heard by means of a hearing tube attached to the cell. In the time the photoacoustic effect was regarded as a curiosity of no practical value. More than 70 years later the advent of the laser with diverse heating effects has revived interest of the phenomenon. Since White (1963) first suggested the generation of acoustic pulses by laser irradiation of metal surface, a variety of workers (Rosencwaig and Gersho 1976; Scruby *et al.* 1980; Charpentier *et al.* 1982; Aadmont and Murphy 1982) have made contributions towards understanding the generation process and characterising the resultant field. It was shown by Rosencwaig and Gersho (1976) that the primary source of the acoustic signal arises from the periodic heat flow from the solid to the surrounding gas as a result of extremely rapid light absorption by solid, which causes an oscillatory motion of a narrow layer of gas at the solid-gas boundary, that produces detected acoustic signal. It was found that the photoacoustic signal depends on the amount of absorbed light energy and thermal properties of the solid, and it is ultimately governed by the magnitude of thermal diffusion length normal to sample surface. Since the thermal diffusion length depends on the chopping frequency, the photoacoustic technique enables one to obtain optical absorption spectra on any type of solid or semisolid material, whether it be crystalline, powder, amorphous, gel, etc. This capability is based on the fact that only the absorbed light is converted to sound. A one-dimensional model for thermal depth profiling was developed by Opsal and Rosencwaig (1982), that provided the expressions for the temperature at the surface of the sample and

for the thermoelastic response beneath the surface. Furthermore Aamodt and Murphy (1982) reported the specific cases where 3-D thermal diffusion effects are important.

2.2 Summary of previous works

With rapid growth of interest in photoacoustic spectroscopy, the photoacoustic technique has been applied to a large range of problems, in particular, to measure accurately thermal diffusivity of different materials (Charpentier *et al.* 1982). The observation of unwanted phenomena was reported, which related to transverse thermal expansion and temperature gradient through the thickness of the sample (rear surface excitation). The mechanical vibration due to thermoelastic bending (called the "drum effect") was observed in the thermal diffusivity measurement of a clamped plate sample. In the experiments the sample (0.5 mm thin metal plate) mounted horizontally on the top of the cell was uniformly illuminated by a 450W Xe-arc lamp. The polychromatic beam was modulated by a frequency-stabilised mechanical chopper, whose frequency could be varied from a few Hertz to a few kHz. A capacitive microphone was used in measurements, with a sensitivity of 50 mV/Nm⁻¹. A lock-in amplifier was used to analyse the magnitude and the phase of the detected signal. Mechanical resonance was observed at several frequencies for many samples of different metals. It was found that at frequencies greater than the characteristic frequency f_c (defined as the inverse of thermal diffusion time), the signal decreases very fast with increasing frequency and the "drum effect" can dominate the photoacoustic signal.

The influence of thermoelastic bending on photoacoustic signal generation was examined theoretically and experimentally in connection with the thermal diffusivity measurement of metals (Rousset *et al.* 1983). In the experiment, the sample, which was sensitive to thermoelastic bending only, was simply supported between two rigid circular knife edges illuminated by a mechanically modulated (a few Hz - a few kHz frequency-stabilised chopper) Xe source. The modulated light was absorbed by the sample (thin plate-0.5 mm), instantly converted into thermal energy and induced thermoelastic bending. The deflections of the sample surface due to the “drum effect” were measured by detecting the deviation of a He-Ne laser beam. The probe beam deviation was read on a position sensor (silicon detector) placed at a distance from the sample. The signals were processed by a lock-in amplifier and recorded. It was found that for the geometrically thin uniformly illuminated sample the response of structure to thermal excitation is characterised by the frequency f_c , which is the inverse of thermal diffusion time. It was shown that the amplitude of thermoelastic bending is independent of modulation frequency at low frequencies (thermally thin sample), while at higher frequencies (thermally thick sample) the amplitude decreases as an inverse of frequency. The theoretical model was developed, which analytically explained thermoelastic bending of solids, using the thermoelasticity equations, the effect is essentially due to a temperature gradient inside of the sample and normal to the side of the greatest dimension of the sample. It was shown that the effect of thermoelastic bending can be used to obtain values of thermal diffusivity for metals directly. Later Rousset *et al.* (1985) developed the technique for non-destructive detection of delamination in layered materials based on photothermal bending effect. In experiments the surface of a material was heated by a focused laser pulse with 0.1-1.0 J an incident power

to a few degrees above the ambient temperature. The induced thermoelastic displacement was detected by a laser interferometer. It was shown that the detectability of defects depends on the relative dimensions of the laser radius, the size of the delamination and the layer thickness.

Hane *et al.* (1988) developed a photothermal probing technique for detection of flexural vibration caused by thermoelastic bending. The vibration of a clamped plate sample was generated by a focused irradiation of modulated laser light. The flexural vibration caused by thermoelastic bending was sensed by the deflection of the probe beam. A 12 mm diameter, 80 μm thick glass plate was fixed around its circumference. The front surface was coated by sputtering with 30 nm thick chromium. A 25 mW of maximum power, 830 nm wavelength diode laser (heating laser) was used to generate the thermal wave. The laser diode was modulated by the rectangular wave signal. The laser beam was focused on the front surface of the plate through the microscopic objective ($10\times$, 0.25 N.A.) with the spot size of the beam $\sim 25 \mu\text{m}$. The deflection of probe beam was measured by a position sensor. The signal was processed by a lock-in amplifier (NF-U575). As found thermoelastic bending is proportional to temperature moment, and its amplitude was saturated at modulation frequency lower than characteristic frequency, while at higher than characteristic frequency it decreases as inverse of modulation frequency. They found that the thermoelastic bending effect can be useful for non-destructive testing of platelike samples using vibration analysis technique.

The thermoelastic bending effect of a layered plate was further examined theoretically and experimentally on the basis of the bending moment and thermal

wave propagation (Hane and Hattori 1990). In experiments the front surface of the sample was irradiated spatially uniformly by chopped laser light. A 25 mW, 830 nm laser diode was modulated rectangularly. The extremely rapid sub-surface conversion of the absorbed light into heat causes the non-uniform temperature distribution across the sample thickness, which induces thermoelastic bending of a sample. The flexural bending of a sample was measured by deflection of a probe beam. It was shown that the thermoelastic bending is proportional to the temperature moment and depends on the modulation frequency. The amplitude of bending moment M_t (measured for two-layer system: 15 μm aluminium sheet and 100 μm thick borosilicate glass) decreases nearly as inverse of modulation frequency f_c^{-1} for frequencies higher than characteristic frequency f_c while increases almost linearly with the decreasing of modulation frequency below f_c and has a very gentle slope around the value f_c . The amplitude and phase signals around f_c and in the region lower than f_c change considerably with increasing thickness of aluminium layer.

Since Venkatesh and Culshaw (1985) reported the vibrations of microresonant structures optically activated and detected, the effects of photothermal excitation of silicon microresonators have been actively investigated for potential use with fibre optics sensors (Andres *et al.* 1986; Greenwood 1988; Zhang *et al.* 1989; Walsh and Culshaw B. 1991). As resonance frequency of silicon microresonators vary in response to changes in environmental parameter of the interest (such as pressure, temperature etc), it can be used as output signal of a sensor. The modulated signal can be readily transmitted through the fibre optic link over considerable distances.

The advantages include immunity to both fluctuations in the intensity transmittance of the link from the sensor and electromagnetic interference, yet structures are intrinsically safe and chemically inert. The structures are extremely small and could be readily interfaced with a fibre optic link by bonding to the fibre tip. For this reason it is necessary that the length of microresonator is to be close to the diameter of the cladding (about several hundreds of micrometers). The width of typical microresonator is about 5-10 μm , which coincides with the core diameter of the single mode fibre (Churenkov 1993). Therefore, the microresonator width is equal to or less than the illuminated spot size, that is time dependent temperature distribution can be described by the one-dimensional heat flow equation. The photothermal drive mechanism and the dependence of resonant frequency of layered microresonators on temperature was investigated by Churenkov (1993) and Walsh and Culshaw (1991). The temperature stability was found to be a major problem of microresonator sensors. On the one hand, the variations of the temperature of illuminated region of a microresonator excite a transverse oscillation. On the other hand, the variations of the temperature at which the transducer works cause drift of the longitudinal beam tension, which consequently causes a shift of the natural frequency of the microresonator. The difference in linear expansion coefficients of a bulk resonator beam, the coating and the mounting can result in resonance frequency drift with variations of the ambient temperature. The resonance frequency is also dependent on the temperature changes of Young's modulus, density and linear sizes. It was shown that the fundamental frequency has been reduced with increase of incident power, and also the metal film thickness deposited upon silicon beams had increased the temperature sensitivity of the microresonators. These resonant sensors can be very

sensitive and versatile, allowing the measurement of a variety of variables such as pressure, acceleration, mass, viscosity etc (Lee *et al.* 1994; Tudor *et al.* 1988).

In the experiments with single and dual laser irradiation of structures Philp *et al.* (1995) found that the excitation of transverse mechanical vibrations was effective when the period of the thermoelastic excitation approximates the period of the natural resonant frequencies of the structure. The resulting vibrations of the samples were detected using small non-contact fibre optic sensor and recorded by Digital Signal Analyser (DSA 602 Tektronics). The shifts in resonant frequencies resulted from the structural defects (small slots which simulated cracks and surface flaws) have been demonstrated using Modal Analysis technique. It was shown that the laser excitation technique used in conjunction with fibre optic sensors offers the potential for an NDT application with totally non-contact excitation and sensing of vibration signatures (Philp and Booth 1991; Philp *et al.* 1995). Later Philp and Booth (1994) reported successful experiments where low power laser diodes and an optical fibre interferometer were used for remote optical excitation and sensing of mechanical vibrations. An unpolished 300 mm×12 mm×3 mm cantilever was used as a test structure. It was clamped by one end in a vice jaws and it was allowed to vibrate in horizontal plane, that its weight would not affect the characteristics of vibration. The small portion of light reflected from the natural surface of a cantilever was used by interferometric sensor and there was only requirement that the surface of the cantilever has to be aligned approximately perpendicular to the interferometer beam. The first five resonance frequencies of a cantilever in the range of 26-1469 Hz were excited and measured. The measurement accuracy of resonance frequencies was effectively limited by the stability ± 0.5 Hz of the TTL

oscillator used. It was found that the efficiency of optical excitation has been maximised at characteristic frequency f_c , which is the modulation frequency of laser with period of oscillation cycle sufficient for the temperature difference between the front and rear surfaces of the structure just to reach its maximum value when the laser is on, and just to relax to zero when the laser is off. The characteristic frequency f_c for a thin plate of thickness h and thermal diffusivity k is given by

$$f_c = \frac{k}{h^2}$$

The calculated characteristic frequency f_c of the aluminium cantilever (with thickness $h=3$ mm) is approximately 10 Hz. However, for the cantilever chosen, all resonance frequencies were greater than 10 Hz. For that reason the response of the system was decreased rapidly for frequencies of excitation above the characteristic frequency f_c of the structure. This problem can be partially overcome using multiple laser diodes for excitation. The practical application of the technique can be used for complex structures: firstly, by using higher power laser diodes, secondly, by improving the sensitivity of the technique operating the interferometer at 632.8 nm and thirdly, by reducing the noise level in the detection electronic by using silicon detectors.

Recently this technique (Philp and Booth 1994) has been successfully applied for determining of mechanical stress in vacuum-deposited thin metallic films on glass substrates (Askraba *et al.* 1996). The test samples, thin circular glass plates (42 mm diameter, 0.1 mm thick) were coated with chromium and attached by gluing to a thin metal rod in the centre. The interferometer (1523 nm wavelength) with an improved low noise detection electronics was used as a sensor. A laser

diode (15 mW 810 nm) was square wave modulated by a TTL driver to excite vibration of the sample. Since the stress in the glass-metal film structure affects the curvature, which in turn causes the shift in resonance frequencies of a wafer, it can be accurately determined by measuring this shift in resonance frequencies. It was found that the resonance frequency shift is directly proportional to “the product of stress by thickness of a metal film.”

2.3 Sensing systems

Most vibration measuring systems are based on the sensing devices, which are called transducers. Transducers convert the measurand into a useable electrical signal. There have been developed many methods used in vibration measurements. Examples include strain gauges (Ready 1974), capacitance variation with proximity (Adams and Bacon 1973), microphones (Adams and Coppendale 1976), piezoelectric transducers or accelerometers (Nagy *et al.* 1978). Currently the piezoelectric type of transducer is by far the most popular and widely used means of measuring the parameters of interest in modal analysis. It does not normally matter which quantity the displacement, the velocity or the acceleration is actually measured, because these quantities are interrelated by simple differentiating and integrating operations. The current tendency to prefer the use of acceleration sensitive devices has two reasons: accelerometers can be made mechanically smaller and their frequency range is wider. If the measured result is wanted in terms of velocity or displacement, rather than in terms of acceleration, use can be made of electronic integrators at the output of the accelerometer. It should be noted that for given application the accelerometer must be chosen with as high sensitivity as possible, on the other hand the higher the sensitivity, the larger and

heavier the transducer. But the addition of even a small transducer to the structure imposes additional and unwanted forces on the structure. Therefore a mechanical transducer mounted on a test structure may significantly affect the accuracy of vibration properties measurements, because of weight and lack of sensitivity. The optical transducers by nature are non-contact and of high accuracy. Many optical techniques have been developed for detection of structural vibrations; examples include: Doppler velocimetry (Buchhave 1975; Laming *et al.* 1986), the holography technique (Aprahamian and Evensen 1970), laser probe beam deflection (Hane *et al.* 1988; Jenkins *et al.* 1995) a variety of non-interferometric fibre optic sensors (Chitnis *et al.* 1989; Philp *et al.* 1995) and a number of the interferometric techniques (Deferrary and Andrews 1966; Deferrary *et al.* 1967; Pernick 1973; Jackson *et al.* 1980; Lewin *et al.* 1985; Philp and Booth 1994)

Jenkins *et al.* (1995) used the method of optical beam deflection to measure the modal shapes of a cantilever. The cantilever of length 23,5 mm, width 2 mm and thickness 0.5 mm was clamped to a micrometer-driven stage with 25mm of travelling range. The cantilever was driven into resonant oscillatory motion using

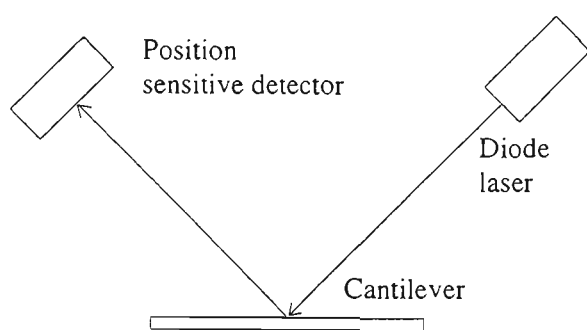


Figure 2.01: The end view of the optical arrangement

the PZT actuator, bonded to the aluminium surface of the cantilever. The laser spot was traversed along the cantilever using the micrometer translation stage. Light

from a diode laser at 670nm was focused onto the surface of the cantilever beam and the position sensitive detector was placed so that the diverging laser beam nearly fills the detector. The PZT amplified signal from the photodetector was sampled by analog-digital converter and analysed using Fast Fourier transform. The displacement was measured by the lock-in-amplifier at each point along the cantilever length. Using this method, the modal shape of each of the cantilever's first four vibration modes were investigated by driving the piezoelectric actuator at the modal frequency previously determined. The method is experimentally simple and non-intrusive, it permits a high degree of spatial resolution along the cantilever length (limited by the wavelength of the laser beam) and its displacement resolution was ultimately limited by shot noise of the detector. The main disadvantage of the technique is that it cannot differentiate between the displacement of the cantilever and its localised curvature.

A fibre optic vibration sensor (proximity sensor) was developed as a non-invasive non-contact alternative to the strain gauges and accelerometer (Philp *et al.* 1995). The intensity modulated proximity sensor was constructed from a 50/125 μm multimode communication grade directional coupler, modulated 820 nm LED light source and a PIN photodiode detector module. The sensor was designed to detect small proximity variations between the unpolished reflective surface and the end of the sensing fibre. Vibrations of amplitude greater than 1mm for mirrored surfaces and 4mm for unpolished aluminium or steel were detected when the sensor was located approximately 50mm from the vibrating surface. The sensor output was reasonably linear for vibration amplitudes up to about 0.2 mm. The area

illuminated by the sensor was approximately $7 \times 10^{-3} \text{ mm}^2$, which is very much smaller than that of the strain gauge bridge ($\sim 100 \text{ mm}^2$). Hence the fibre sensor allowed much greater spatial resolution and more accurate resonance frequency determination. This optical proximity sensor was used to investigate the modal frequencies of cantilevers in an electromagnetically noisy environment, which restricted the use of some standard electrical detectors.

Bulk and fibre-optic interferometric sensors are extremely sensitive devices since they respond to optical path changes, which are the small fractions of a wavelength (Dakin and Culshaw 1989). The basic concept is in the optical phase modulation resulted from the interference of signal and reference beams, which is converted into a time varying irradiance function, observable as a fringe pattern. A photodetector monitors the light intensity variation at a point in the pattern and provides electrical signals for subsequent processing. Since the photodetector signal is proportional to the normalised light intensity, the linear displacement amplitude can be determined from the temporal frequency characteristics of the output signal. Two signal processing techniques have been actively used in optical interferometry: homodyne and heterodyne. An optical configuration involving the interference of two light beams with essentially the same optical frequency is called a homodyne system. The homodyne method is particular simple and inexpensive for measurement of vibration displacements of simple harmonic motion. The heterodyne method is more complex and suitable for measurement of non-sinusoidal motion.

Deferrary et al. (1967) described four homodyne experimental methods for measuring vibration displacements at a point on a transducer face in air or water. The technique utilised a Michelson interferometer with CW laser light source. This method has the advantages: the ability to make displacement measurements in the range 0.1-6000 Å and higher, in frequency range 100 Hz-20 KHz; the capability to probe into otherwise an inaccessible area over which are desired; the ability to scan an area by making measurements at points whose diameter could be on the order of 0.1 mm; no added mass owing to instrumentation as is the case with an accelerometer; no interference with the acoustic field as might happen for example with a capacitance device; the capability for making displacement measurements of a point, on a diffuse surface. A simplified model considered the current measured at the output of the photomultiplier tube as a result of the homodyning action between the two split portions of one monochromatic ray in a Michelson interferometer with perfectly reflecting mirrors that were lined up optically without error. The term homodyne efficiency was introduced to account for:

- a) The finite diameter of the laser beam
- b) The lack of monochromaticity of the actual laser source
- c) The slight, but typical misalignment of optics in the practical set-up.

It was found that a diffuse surface has much lower Signal-to-Noise ratio S/N for a given laser intensity. In order to prevent the decrease of homodyne efficiency one would normally choose a polished surface for small vibration displacements. The vibration isolation and quiet surroundings are required for measurements of small displacements as phototube shot noise is the ultimate limitation of sensitivity of the technique.

Linear vibration motion yields a phase change that is spatially uniform but harmonic in time. Unfortunately, phase changes induced by other extraneous effects (such as non-sinusoidal or rotational motion) may considerably disturb the homodyne measurement. In order to verify the measurement of linear vibration amplitude Pernick (1973) developed a new self-consistent technique (modified over the methods mentioned above). This technique was based upon a comparison among a number of independent simultaneous optical phase measurements at neighbouring frequencies which are proportional to the Bessel functions of different orders. As the refraction index n is arbitrarily chosen the value of the phase change and associated displacement can be directly established. Independent measurements of phase change were obtained by using several choices for n together with associated filtered output signals at the harmonic frequencies of $(n-1)\cdot\omega_0$, $n\omega_0$, $(n+1)\cdot\omega_0$. With such an experimental system the amplitude measurement could be read directly.

The sensitivity, particularly with fibre interferometers, produces its own problems in that fluctuations in ambient parameters (particularly temperature: Musha *et al.* 1982) randomly affect path difference between the two beam paths of the interferometer and the output signal undergoes unpredictable fading (Dandridge 1991; Jackson and Jones 1989; Sheem *et al.* 1982). As long as the phase shift due to the measurand is detected, the changes in source intensity and frequency, the polarisation states of the interfering beams also cause unpredictable variations (Sudarshanam 1992).

In order to detect surface vibrations induced by low power diode laser excitation of structure, an improvement in detection sensitivity of about three orders of magnitude over that of the proximity sensor was required. To achieve this improvement, a stabilised fibre-optic interferometer was constructed by Philp and Booth (1994) which exhibited a resolution of a few nanometres (see Figure 3.04 for experimental arrangement). A 1523 nm He-Ne laser source was chosen for interferometer because it has a very long coherence which is suitable for the use with long air paths and because its compatibility with standard 1550 nm single-mode couplers. The light from the laser was launched into one input arm of a single-mode 2x2 directional coupler, which divided into signal and reference branches. The beam reflected from the vibrating surface was coupled back into the coupler to give modulated light in the signal arm. The optical power in the reference arm was attenuated using a few small radius turns of the fibre to match the optical power to that of the signal arm and thus formed high-contrast interference. Any change in separation between the sensing fibre tip and the vibrating surface varied the path length of the signal branch with respect to the reference branch, causing intensity modulation of the output. A fibre-air-fibre optical path was incorporated into interferometer design to enable non-contact surface vibration detection. The optical path from fibre to open-air, and back again into a fibre after specular reflection, significantly reduced optical power in the signal arm (reducing the SNR) and so limited the output sensitivity to 1.2×10^{-2} rad over a 30 KHz bandwidth (7×10^{-5} rad/Hz) at 100 Hz.

2.4 Thermoelastic bending of a structure

As stated earlier light absorbed by the solid is partly converted into heat by interaction with electrons. The light energy absorbed by an electron is distributed and passed on to the lattice in the same processes, which govern the transfer of heat (Carslaw and Jaeger 1959). The distribution occurs so rapidly that we can regard the optical energy as being instantaneously turned into heat at the point at which the light was absorbed. The heated region undergoes thermal expansion and thermoelastic stresses generate elastic waves which propagate deep within the sample. The differential equation for heat flow in a semi-infinite slab (half-space) of material with a boundary plane at $z=0$ (the metal surface) was given by

$$\nabla^2 T(x, y, z, t) - \frac{1}{k} \frac{\partial T(x, y, z, t)}{\partial t} = -\frac{U(x, y, z, t)}{K}, \quad 2.01a$$

where $T(x, y, z, t)$ is the temperature distribution, $U(x, y, z, t)$ is the heat produced per unit volume per unit time, k and K are the thermal diffusivity and thermal conductivity, respectively (Ready 1971). If it is assumed that the absorbed flux density is a function of radial position r , measured in the x - y plane from the z axis, and that it is Gaussian in nature Ready (1971) has shown that the solution of Eq. 2.01a is:

$$T(r, z, t) = \frac{I_{\max}}{K} r_s^2 \left(\frac{k}{\pi} \right)^{\frac{1}{2}} \times \int_0^t \frac{w(t-t') dt'}{(t')^{\frac{1}{2}} (4kt' + r_s^2)} \exp\left(\frac{-z^2}{4kt'} - \frac{r^2}{4kt' + r_s^2} \right), \quad 2.02$$

where I_{\max} is the absorbed power per unit area at the centre of the Gaussian spot of the radius r_s , $w(t)$ is the normalised laser pulse shape and r radial position of absorbed flux density.

For many cases of practical interest, the problem can be regarded as one - dimensional, that is, the transverse dimensions of the laser beam are large

compared to the depth to which heat is conducted during the time of the laser pulse. Then the dependence on the x and y coordinates drops out and the heat flow equation becomes (Ready, 1971)

$$\nabla^2 T(z, t) - \frac{1}{k} \frac{\partial T(z, t)}{\partial t} = -\frac{U(z, t)}{K}, \quad 2.01b$$

The light is absorbed at the surface of a metal with an absorption coefficient α_s .

The heat production for one-dimensional case was given by

$$U(z, t) \equiv I(t) \left(\frac{1}{\delta} \right) e^{-\alpha_s z}, \quad 2.03$$

where $I(t)$ is $(1-\Gamma)$ times the irradiance incident on the surface (where Γ is the surface reflectivity) and the spatial pulse shape is uniform. For metals the real part of the dielectric constant ϵ is negative, and the penetration depth δ is related to the skin depth δ_s for penetration of an electric field into the metal by

$$\delta = \delta_s / 2 = c / 2 \omega_{c0} (-\epsilon)^{1/2}, \quad 2.04$$

where c and ω_{c0} are, respectively, the velocity and angular frequency of the light. For a typical metal, with absorption coefficient of the order of 10^5 to 10^6 cm^{-1} , if the laser pulse is flat in time and uniform over the x - y plane, temperature distribution can be written:

$$T(0, t) = \left(\frac{2I_0}{K} \right) \left(\frac{kt}{\pi} \right)^{1/2}. \quad 2.05$$

Eq. 2.05 is useful in estimating approximate surface temperature rises for a broad variety of cases.

The mechanical effect resulted from the heating of the front surface of cantilever can be calculated by division the beam into a number of thin layers (Philp 1993). It

was found that the thermal expansion produces a thermal strain $\varepsilon_s(\chi)$ given by

$$\varepsilon_s(\chi) = \Delta L_t / L = \alpha_t \Delta T(\chi), \quad 2.06$$

where L is the length of the cantilever beam, ΔL_t is the linear thermal expansion, α_t is thermal expansion co-efficient, $\Delta T(\chi)$ is the temperature of each layer above the temperature of the rear surface. The equivalent force $P(\chi)$ which would produce the same bend and strain as this thermal expansion is

$$P(\chi) = \varepsilon_s(\chi) b E \delta h, \quad 2.07$$

for a cantilever of given length (L), width (b), thickness (h) and Young's modulus (E). The moment of this force $M(\chi, t)$ about the mid-plane is

$$M(\chi, t) = \chi P(\chi) = \alpha_t b E \delta h \chi \Delta T(\chi, t). \quad 2.08$$

Then the total thermally-induced bending moment $M(t)$ for the entire beam is

$$M_t(t) = \alpha_t b E \int_{-\frac{h}{2}}^{\frac{h}{2}} \Delta T(x, t) x dx, \quad 2.09$$

where α_t is the thermal expansion co-efficient, $\Delta T(x, t)$ is the temperature of a layer.

2.5 Vibration analysis background

A treatment of structural vibration and modal analysis is contained in very many standard texts (Main 1993, Nashif *et al.* 1985, Vierck 1979) and most of the details need not be repeated in this thesis. However, some of the concepts and results are critical to an understanding of this thesis and hence need to be discussed. The treatment below is intended to summarise the major relevant parts of the theory in a way, which provides a basis for discussing the experimental results, which follow in subsequent chapters. The description is restricted to the case of transverse

mechanical vibrations of a structure.

Any structure with mass and elasticity possesses one or more natural frequencies of vibration. The natural frequencies are the result of cyclic exchanges of kinetic and potential energy within the structure. The kinetic energy associated with velocity of structural mass, while the potential energy is associated with storage of energy in the elastic deformations of a resilient structure. The rate of energy exchange between the potential and kinetic forms of energy determines the natural frequency.

A linear structure is one in which the deformation is proportional to load, or whatever excitation is causing the structure to vibrate. In a linear structure this proportionality applies regardless of the direction, magnitude or distribution of the load. For a linear structure, it can be shown that the natural resonant vibration frequency of the structure is independent of the amplitude of vibration (Blevins 1979). There is always some damping (energy loss) in real structures, which will make free vibrations decay with time, and there is some amplitude beyond which the structure no longer behaves linearly. For real structures the concept of natural resonant frequency must be tempered by some knowledge of the differences between the ideal mathematical model and the actual structure. The discrepancies between a linear model and a real structure are often due to neglected linear and non-linear effects. Some linear effects (which are often neglected) are the effect of shearing deformation in slender structures and the effect of surrounding fluid. Non-linear effects (which are often neglected) are plasticity due to yielding and the vibration amplitude dependence on damping (Blevins 1979). The simple linear theory (which neglects these effects) represents a very good approximation to the

conditions, under which the experimental part of this work was carried out, in particular, the optical excitation of transverse vibration with very small displacements of the order of tens of nanometres. Another point, which needs to be made clear is that optical excitation of a structure in the thermoelastic (non-ablative) regime causes vibration by inducing the structure to bend. Thus the vibration is most appropriately described in terms of thermally-induced bending moments and angular displacements rather than the more usual discussion based on forces and linear displacements (Philp 1993). However, the interferometric vibration detection system detects linear displacements at a point and it is more convenient to use this in the discussion of experimental results. The measured linear displacements are of course proportional to the angular ones and the two treatments are completely analogous (both give rise to second order differential equations but the physical meaning of the various constants are different in the two cases). In the discussion which follows in this section, a treatment in terms of forces and displacements is used to illustrate the essential physics as this is simpler, more familiar to most readers and can more easily be referred to in standard texts. The results derived are quite general and apply equally well to vibrations induced by bending moments. Experiments described in subsequent chapters were carried out using simple cantilever beams as these are convenient targets for which the various modal vibration properties are easily calculated. For this reason, the discussion below is described mostly in terms of these structures. During transverse vibration, the beam flexes perpendicular to its own axis to alternately store potential energy in the elastic bending of the beam and then release it into the kinetic energy of transverse flexural vibrations. The general assumptions used in the beam analysis are:

- (a) The beam is uniform along the span;
- (b) The beam is composed of a linear, homogeneous, isotropic elastic material;
- (c) The beam is slender - the dimensions of the beam cross section are much less than the length of the beam or the distance between vibration nodes; shear deformation is not considered;
- (d) Only deformations normal to the undeformed beam axis are considered, plane sections remain plane;
- (e) No axial loads are applied to the beam;
- (f) The centre of the beam cross section coincides with the centre of mass (ie., the plane of vibration is also a plane of symmetry of the beam) so that rotation and translation of the beam are uncoupled.

When a beam is subjected to externally applied transverse forces, both shearing forces and bending moments will exist; the result is that the beam will deflect. Deflection will occur due to both the shearing force and the bending moment, but in practical cases the deflection due to shear can generally be neglected compared with that due to bending.

2.5.1 Differential equation of motion for elastic bar

The general equation for transverse free vibration of a uniform prismatic beam has been derived by Timoshenko *et al.* (1974). A prismatic beam has been drawn in the x - y plane, which is assumed to be a plane of symmetry for any cross section. If y represents the transverse displacement of a typical segment of the beam dx , x is the distance of dx from the left-hand end. Fig. 2.02 shows a free body diagram of an element of the length dx with internal and inertial actions upon it. In Fig. 2.02

ρ is the density of material, E is the Young's modulus of the material, $I_x(x)$ is the moment of inertia of the cross section of the beam \mathbf{A} , with reference to its neutral axis, the transverse shear force $V_s(x)$ is positive upward, the bending moment $M(x)$ is positive clockwise. The dynamic equilibrium conditions for the element of the

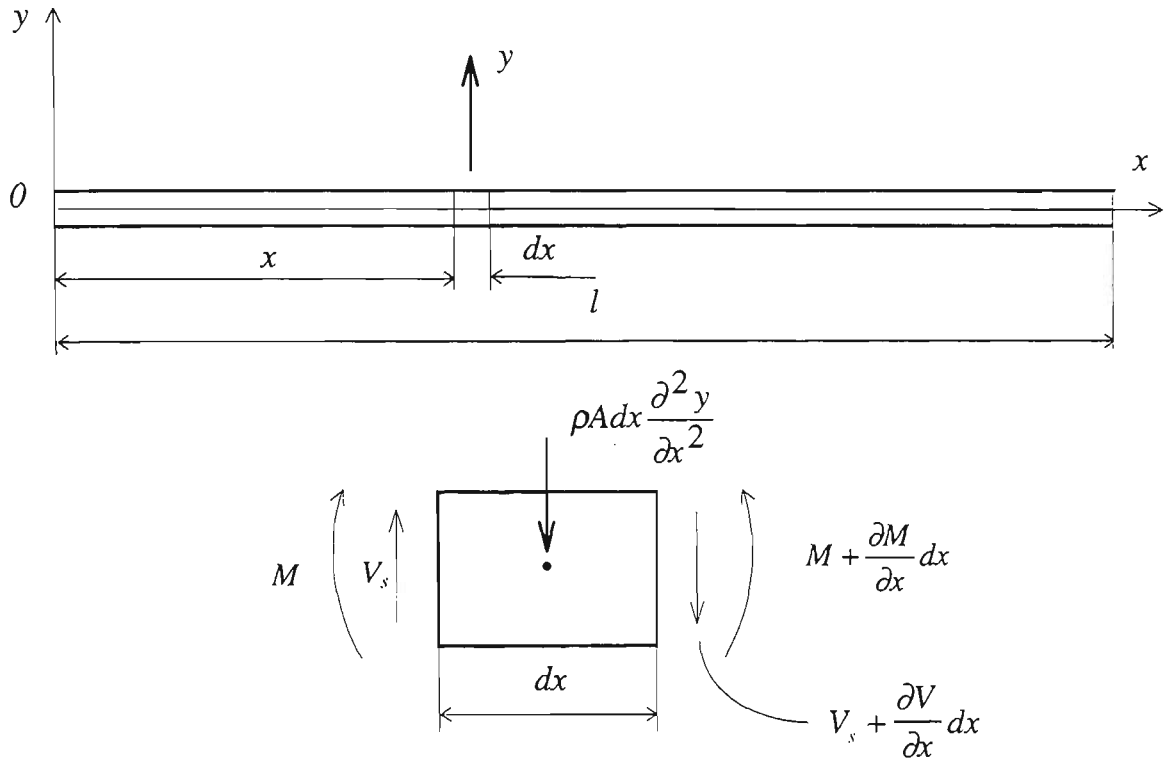


Figure 2.02: The forces and moments of a vibrating cantilever

beam between x and $x+dx$ can be written for vertical forces and for the moments:

$$V_s - \left(V_s + \frac{\partial V}{\partial x} dx \right) - \rho A dx \frac{\partial^2 y}{\partial t^2} = 0. \quad 2.12$$

And the moment equilibrium condition gives:

$$M + \frac{\partial M}{\partial x} dx = M + V_s dx + \rho A dx \frac{dx}{2}. \quad 2.13$$

By neglecting the higher-order term $(dx)^2$ and substituting V_s from Eq. 2.12 into Eq.

2.13 produces

$$\frac{\partial^2 M}{\partial x^2} dx = -\rho A dx \frac{\partial^2 y}{\partial t^2}. \quad 2.14$$

From flexural theory

$$M = EI_r \frac{\partial^2 y}{\partial x^2}, \quad 2.15$$

and using this expression in Eq. 2.14, we obtain

$$\frac{\partial^2}{\partial x^2} \left(EI_r \frac{\partial^2 y}{\partial x^2} \right) dx = -\rho A dx \frac{\partial^2 y}{\partial t^2}. \quad 2.16$$

Eq. 2.16 is the general equation for transverse vibration of a beam. The flexural rigidity EI_r does not vary for the prismatic beam with x and Eq. 2.16 can be written in the form:

$$EI_r \frac{\partial^4 y}{\partial x^4} dx = -\rho A dx \frac{\partial^2 y}{\partial t^2}. \quad 2.17$$

This equation may also be rewritten as

$$\frac{\partial^4 y}{\partial x^4} = -\frac{1}{a^2} \frac{\partial^2 y}{\partial t^2}, \quad 2.18$$

$$\text{where } a = \sqrt{\frac{EI_r}{\rho A}}. \quad 2.19$$

When a beam vibrates transversely in one of its natural modes, the deflection at any location varies harmonically with time:

$$\tilde{Y}_n(x, t) = Y_n(x) (C_{1n} \cos \omega_n t + C_{2n} \sin \omega_n t). \quad 2.20$$

Substituting Eq. 2.20 into Eq. 2.18 results in

$$\frac{d^4 Y_n(x)}{dx^4} - \frac{\omega_n^2}{a^2} Y_n(x) = 0, \quad 2.21$$

and by introducing the notation $\frac{\omega_n^2}{a^2} = k_n^4$, it can be rewritten as:

$$\frac{d^4 Y_n(x)}{dx^4} - k^4 Y_n(x) = 0. \quad 2.22$$

The general form of the solution for Eq. 2.22 is

$$Y_n(x) = C_{1n} e^{k_n x} + C_{2n} e^{-k_n x} + C_{3n} e^{jk_n x} + C_{4n} e^{-jk_n x}, \quad 2.23$$

which may be written in the equivalent form

$$Y_n(x) = C_{1n} \sin k_n x + C_{2n} \cos k_n x + C_{3n} \sinh k_n x + C_{4n} \cosh k_n x. \quad 2.24$$

This expression represents a normal function for transverse vibration of prismatic beam, which describes the relative displacement of any point on the structure as the structure vibrates in a single mode. This function is also called a Mode shape (or Eigenvector) and is associated with each natural frequency (Eigenvalue) of a structure. It is useful to write the general expression for a normal function Eq. 2.24 in the equivalent form:

$$Y_n(x) = C_{1n} (\cos k_n x + \cosh k_n x) + C_{2n} (\cos k_n x - \cosh k_n x) + C_{3n} (\sin k_n x + \sinh k_n x) + C_{4n} (\sin k_n x - \sinh k_n x). \quad 2.25$$

The constants C_{1n} , C_{2n} , C_{3n} and C_{4n} in Eq. 2.25 can be determined in each particular case from the boundary conditions at the ends of the beam. Assuming that the left end is built in for the clamped-free cantilever then:

at the fixed end the deflection and slope are equal to zero

$$(Y_n(x))_{x=0} = 0, \quad \left(\frac{dY_n(x)}{dx} \right)_{x=0} = 0,$$

and at the free end the bending moment and the shearing force both vanish, so

$$\left(\frac{d^2 Y_n(x)}{dx^2} \right)_{x=0} = 0, \quad \left(\frac{d^3 Y_n(x)}{dx^3} \right)_{x=L} = 0.$$

From the first two conditions $C_{1n} = C_{3n} = 0$ in the general solution Eq. 2.25 so that

$$Y_n(x) = C_{2n}(\cos k_n x - \cosh k_n x) + C_{4n}(\sin k_n x - \sinh k_n x). \quad 2.26$$

The remaining two conditions give the following frequency equation:

$$\cos k_n L \cdot \cosh k_n L = -1, \quad 2.27$$

it can be rewritten by denoting $\beta_n = k_n L$:

$$\cos \beta_n \cdot \cosh \beta_n = -1.$$

The consecutive roots of this equation are (Thomson 1993):

$$\beta_1=1.875; \quad \beta_2=4.694; \quad \beta_3=7.855; \quad \beta_4=10.996; \quad \beta_5=17.279.$$

The frequency of vibration of any mode will be:

$$f_n = \frac{\omega_{0n}}{2\pi} = \frac{(\beta_n)^2}{2\pi L^2} \sqrt{\frac{EI_r}{\mu}}, \quad 2.28$$

where β_n is a dimensionless parameter, which is a function of the boundary conditions applied to the beam, L is the length of the beam and $\mu = \rho A$ is the mass per unit length of the beam. If the structure vibrates only in the n_{th} mode, the deflection can be written as

$$Y_n\left(\frac{x}{L}\right) = \cosh \frac{\beta_n x}{L} - \cos \frac{\beta_n x}{L} - \frac{\cosh \beta_n + \cos \beta_n}{\sinh \beta_n + \sin \beta_n} \left(\sinh \frac{\beta_n x}{L} - \sin \frac{\beta_n x}{L} \right), \quad 2.29$$

$$\text{introducing } \sigma_n = \frac{\cosh \beta_n + \cos \beta_n}{\sinh \beta_n + \sin \beta_n}, \quad 2.30$$

Eq. 2.29, which is the characteristic function, can be simplified

$$Y_n\left(\frac{x}{L}\right) = \cosh \frac{\beta_n x}{L} - \cos \frac{\beta_n x}{L} - \sigma \left(\sinh \frac{\beta_n x}{L} - \sin \frac{\beta_n x}{L} \right). \quad 2.31$$

As shown (Eq. 2.20) the vibration function is:

$$\tilde{Y}_n(x, t) = Y_n(x) (C_{1n} \cos \omega_n t + C_{2n} \sin \omega_n t),$$

where $Y_n(x)$ is the Mode shape, that is a function only of length of a beam, and

$\tilde{Y}_n(t)$ is a function only of time. If the beam vibrates freely, then the total

transverse deformation is the sum of the modal deformations:

$$\tilde{Y}(x, t) = \sum_{n=1}^N A_n Y_n(x) \text{Sin}(2\pi f_n t + \phi_n), \quad 2.33$$

where $Y_n(x)$ is the transverse displacement associated with the n^{th} vibration mode, and ω_{0n} , A_n and ϕ_n are the natural frequency, amplitude and phase of that mode. A_n and ϕ_n are determined by the means used to set the beam in motion (Blevins, 1979).

For the case of forced vibration of a prismatic bar the differential equation of motion can be written (Volterra and Zachmanoglou 1965):

$$EI_r \frac{\partial^4 \tilde{Y}(x, t)}{\partial x^4} = p(x, t) - \rho A dx \frac{\partial^2 \tilde{Y}(x, t)}{\partial t^2}, \quad 2.34$$

Assuming that the general solution of this equation is of the form

$$\tilde{Y}(x, t) = \sum_{n=1}^{\infty} Y_n(x) f_n(t), \quad 2.35$$

where the function $Y_n(x)$ is the normal function satisfying the differential equations

$$EI_r \frac{d^4 Y_n(x)}{dx^4} = \omega_{0n}^2 \rho A Y_n(x), \quad (n = 1, 2, \dots), \quad 2.36$$

and the four boundary conditions at the ends of the bar. Substituting of Eq. 2.35 into Eq. 2.34 gives

$$EI_r \sum_{n=1}^{\infty} \frac{d^4 Y_n(x)}{dx^4} f_n(t) = p(x, t) - \rho A \sum_{n=1}^{\infty} Y_n(x) \frac{d^2 f_n(t)}{dt^2}. \quad 2.37$$

In view of Eq. 2.36, Eq. 2.37 can be written

$$\sum_{n=1}^{\infty} \omega_{0n}^2 Y_n(x) f_n(t) = \frac{1}{\rho A} p(x, t) - \sum_{n=1}^{\infty} Y_n(x) \frac{d^2 f_n(t)}{dt^2}. \quad 2.38$$

Multiplying both sides of Eq. 2.38 by $Y_m(x)$, ($m = 1, 2, \dots$), and integrating between 0 and L , and considering the fact that the functions $Y_m(x)$ satisfy the following

relations (Volterra and Zachmanoglou 1965):

$$\int_0^L Y_n(x)Y_m(x)dx = \begin{cases} =0 & \text{for } n \neq m \\ =\frac{L}{2} & \text{for } n=m \end{cases}, \quad 2.39$$

Eq. 2.38 reduces to

$$\frac{d^2 f_n(t)}{dt^2} + \omega_{0n}^2 f_n(t) = \frac{2}{\rho A} P_n(t) \quad (n = 1, 2, \dots), \quad 2.40$$

$$\text{where } P_n(t) = \int_0^L p(x, t)Y_n(x)dx, \quad 2.41$$

$p(x, t)$ is generally a function of both x and t . Eq. 2.41 is essentially the same as the differential equation for forced vibration of an undamped system with one degree of freedom.

2.5.1.1 Resonance frequency and temperature shift

It can be seen from Eq. 2.28, that Modal frequency is proportional to magnitude of Young's modulus E and on the other hand is inversely proportional to squared length of a cantilever L^2 and square root of material density $\sqrt{\rho}$. It can be shown that the length and density changes of the structure due to thermal drift have negligible effect on the value of resonance frequency of a structure, but Young's modulus dependence on temperature may be considerable in terms of obtainable measurement accuracy. The relation of Young's modulus to the temperature change was given by (Kaye and Laby 1973):

$$E = E_0(1 - \alpha_E \cdot \Delta T), \quad 2.42$$

where E_0 is Young's modulus at temperature of 15°C , α_E is temperature coefficient, and ΔT is temperature change. By differentiating Eq. 2.28 and Eq. 2.42 can be written in the form:

$$\Delta f_n(E) = \frac{\partial f}{\partial E} \cdot \Delta E = \frac{\partial f}{\partial E} \cdot \frac{\partial E}{\partial T} \cdot \Delta T = -\frac{1}{2} \sqrt{\frac{\alpha_E^2}{1 - \alpha_E \cdot \Delta T}} \cdot f_n(E) \cdot \Delta T. \quad 2.43$$

Not only frequency is so sensitive to tiny changes of Young's modulus (E) due to the temperature changes, damping factor is also strongly dependent on stiffness of the structure and thus on Young's modulus.

2.5.2 Equation of motion for Single Degree of Freedom structure

A mechanical vibratory system, which requires only one coordinate to define motion is called a single-degree-of-freedom system. For SDOF a free vibration analysis yields its natural frequency, mode shape and damping factor by solving the differential equations of motion. In order to characterise the vibration properties of a straight elastic cantilever beam under the general assumptions above and with extremely small displacements it can be approximated as a single degree-of-freedom system, for which the displacement at any instant can be specified by a single coordinate y . For SDOF the equation of forced oscillatory motion with viscous damping is given by

$$m\ddot{y} + c\dot{y} + ky = N_0 \sin \omega_f t, \quad 2.44$$

where m is the mass of the vibrating structure, c is a damping constant, κ is the stiffness constant, ω_f the angular frequency of the driving force and N_0 the amplitude of this force.

The solution is the sum of a transient term y_t and a steady state forced term y_f

$$y = y_t + y_f. \quad 2.45$$

The transient term is obtained by solving Eq. 2.44, when the right hand side is zero.

The general solution is then

$$y_t = C_1 e^{\left[-(c/2m) + \sqrt{(c/2m)^2 - (\kappa/m)}\right]t} + C_2 e^{\left[-(c/2m) - \sqrt{(c/2m)^2 - (\kappa/m)}\right]t} \quad 2.46$$

Introducing the damping constant c_c and damping factor ζ (Vierck 1979)

$$\frac{c_c}{2m} = \sqrt{\frac{\kappa}{m}} = \omega_0, \quad 2.47$$

$$\zeta = \frac{c}{c_c}, \quad 2.48$$

where c_c is the value of c for critical damping and ω_0 is natural resonance frequency and ζ is the damping factor. For weakly damped systems $c^2 < 4mk$, or $\zeta < 1$ the solution can be written:

$$\begin{aligned} y_t &= e^{-\zeta\omega_0 t} \left(C_3 \sin \sqrt{1 - \zeta^2} \omega_0 t + C_4 \cos \sqrt{1 - \zeta^2} \omega_0 t \right) \\ &= F_1 e^{-\zeta\omega_0 t} \sin(\omega_d t + \phi), \end{aligned} \quad 2.49$$

where ω_d is the angular damped frequency (Nashif *et al*, 1985). It is given by

$$\omega_d = \sqrt{1 - \zeta^2} \omega_0. \quad 2.50$$

Both F_1 and ϕ are determined by initial motion conditions. The first part, $F_1 e^{-\zeta\omega_0 t}$, represents a decaying amplitude for the trigonometric function $\sin \omega_d t + \phi$. Thus the motion is oscillatory but with an amplitude that reduces with time. For the damped system, the rate of decay of the vibration is conveniently expressed by the ratio of the amplitudes any two successive peaks in the damped motion:

$$\frac{y_j}{y_{j+1}} = \frac{F_1 e^{-\zeta\omega_0 t_j}}{F_1 e^{-\zeta\omega_0 (t_j + T)}} = e^{\zeta\omega_0 T}, \quad 2.51$$

where T is the period of the damped motion which is given by

$$T = \frac{2\pi}{\omega_d} = \frac{2\pi}{\sqrt{1 - \zeta^2} \omega_0}. \quad 2.52$$

The ratio of successive peak amplitudes is conveniently expressed as a logarithmic

decrement, δ_i ,

$$\delta_i = \ln \frac{y_j}{y_{j+1}} = \zeta \omega_0 T = \frac{2\pi\zeta}{\sqrt{1-\zeta^2}}. \quad 2.53$$

Another way of expressing the damping effect is by means of the time taken for the amplitude to decay to $e^{-1}=0.368$ of its original value F_j . This time (τ) is called the modulus of decay or decay time (Pain 1993) and the amplitude is

$$F_\tau = F_1 e^{-\zeta \omega_0 \tau} = F_1 e^{-1} \quad 2.54$$

The decay of energy is proportional to squared amplitude:

$$F_t^2 = F_1^2 e^{-(\zeta \omega_0 t)^2}, \quad 2.56$$

and may be written

$$\mathbf{E} = \mathbf{E}_1 e^{-\zeta \omega_0 t}, \quad 2.57$$

$$\text{where decay time } \tau = \frac{1}{2\zeta \omega_0}. \quad 2.58$$

The other term in Eq. 2.45 is a particular solution, which represents a part of the motion that will occur continuously while the forcing condition is present, and hence this is the steady state solution which has the form:

$$y_f = F \sin(\omega_f t - \phi_1). \quad 2.59$$

The complete solution for $\zeta < 1$ is given by:

$$y = F_1 e^{-\zeta \omega_0 t} \sin(\omega_d t + \phi) + F \sin(\omega_f t - \phi_1). \quad 2.60a$$

The form of the steady state solution is obtained by assuming a solution of the form

$$y_f(t) = C_1 \sin \omega_f t + C_2 \cos \omega_f t, \quad 2.60b$$

where C_1 and C_2 are constants. By differentiating this expression and substituting into the differential equation Eq. 2.44 the values of C_1 and C_2 can be obtained. After rearrangement into the same form as the steady state part of Eq. 2.60a, the

amplitude and phase can be shown to have the form (Vierck, 1979):

$$F = \frac{N_0}{k} \left[\frac{1}{\left(1 - \left(\frac{\omega_f}{\omega_0}\right)^2\right)^2 + \left(2\zeta\left(\frac{\omega_f}{\omega_0}\right)\right)^2} \right]^{\frac{1}{2}} = F_0 \left[\frac{1}{(1 - \mathbf{r}^2)^2 + (2\zeta\mathbf{r})^2} \right]^{\frac{1}{2}}, \quad 2.61$$

$$\tan \phi_1 = \frac{2\zeta\left(\frac{\omega_f}{\omega_0}\right)}{1 - \left(\frac{\omega_f}{\omega_0}\right)^2} = \frac{2\zeta\mathbf{r}}{1 - \mathbf{r}^2}, \quad 2.62$$

where $F_0 = \frac{N_0}{k}$, and $\mathbf{r} = \frac{\omega_f}{\omega_0}$.

These equations show that the normalised amplitude and the phase ϕ are functions only of the frequency ratio $\mathbf{r} = \omega_f/\omega_0$ and the damping factor ζ .

The form of the equations above can be seen much more physically by representing the various acceleration terms in the original equation of motion (Eq. 2.44) on a vector diagram as shown below in Fig. 2.03 (Beards 1981). Eq. 2.44 can be rewritten as

$$\ddot{y} + \gamma \cdot \dot{y} + \omega_0^2 \cdot y = \frac{N_0}{m} \sin \omega_f t, \quad 2.63$$

where $\gamma = c/m$, $\omega_0^2 = k/m$.

Using the previous form of the steady state solution $y = F_0 \sin(\omega_f t - \phi_1)$ and substituting for each term in Eq. 2.63, the vector diagram is obtained.

$$\dot{y} = -F\omega_f \cos(\omega_f t - \phi_1) = F\omega_f \sin(\omega_f t - \phi_1 + \frac{\pi}{2}), \quad 2.64$$

$$\ddot{y} = -F\omega_f^2 \sin(\omega_f t - \phi_1) = F\omega_f^2 \sin(\omega_f t - \phi_1 + \pi). \quad 2.65$$

The equation of motion (Eq.2.63) becomes:

$$F\omega_f^2 \sin(\omega_f t - \phi_1 + \pi) + \gamma F\omega_f \sin(\omega_f t - \phi_1 + \frac{\pi}{2}) + F\omega_0^2 \sin(\omega_f t - \phi_1) = \frac{N_0}{m} \sin \omega_f t \quad 2.66$$

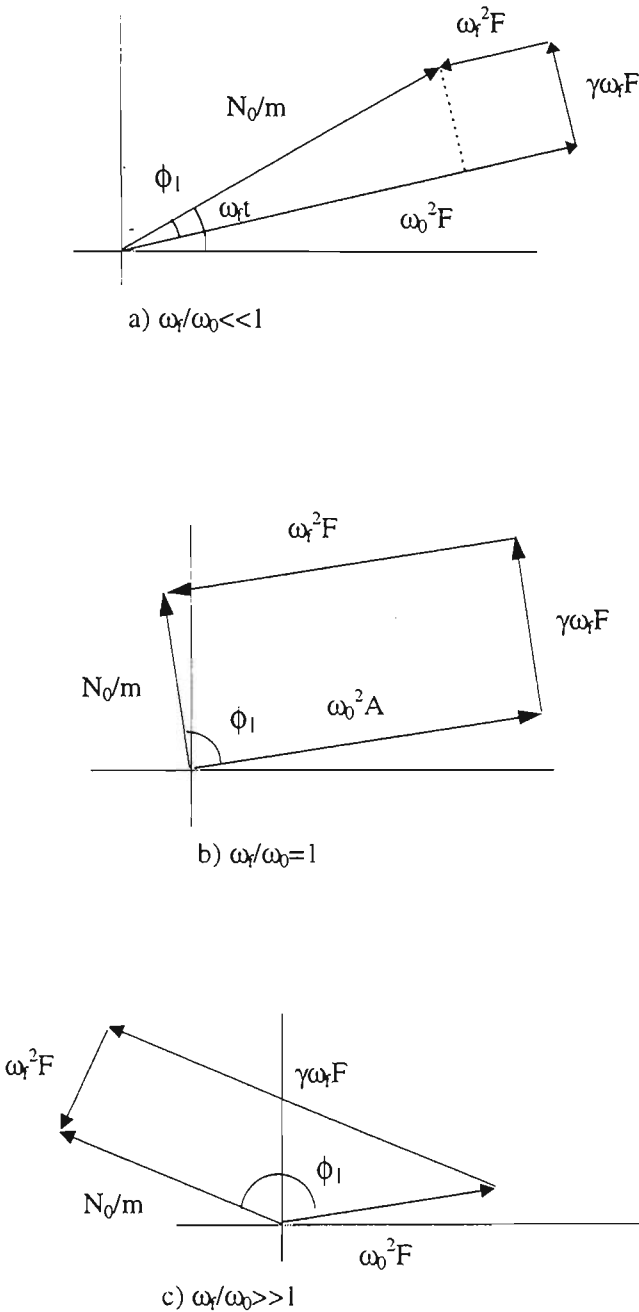


Figure 2.03: The vector relationship in damped forced vibration

As shown in Fig. 2.03 each term (Eq. 2.63) represents an acceleration at $t=0$.

The first derivative \dot{y} has amplitude $F\omega_f$ and is 90° ahead of displacement y , and that \ddot{y} has amplitude $F\omega_f^2$ and is 90° ahead of \dot{y} . From the diagram ϕ_1 must lie in the range $\pi \geq \phi_1 \geq 0$. The value of ϕ_1 and the amplitude F can be found from the triangle in the Fig.2.03(a) as:

$$F = \frac{N_0}{m} \left[\frac{1}{(\omega_0^2 - \omega_f^2)^2 + \gamma^2 \omega_f^2} \right]^{\frac{1}{2}}, \quad 2.67$$

$$\text{and } \tan \phi_1 = -\frac{\gamma \omega_f}{\omega_0^2 - \omega_f^2}, \quad 2.68$$

Corresponding equations for velocity and acceleration amplitudes can be easily found by multiplying Eq. 2.67 by ω_f and ω_f^2 respectively.

2.5.2.1 Response function for Single Degree of Freedom system

It is convenient to write the displacement, velocity and acceleration in terms of a dimensionless response function (Main 1993):

$$R(\omega_f) \equiv \frac{\gamma^2 \omega_f^2}{(\omega_0^2 - \omega_f^2)^2 + \gamma^2 \omega_f^2}. \quad 2.69$$

The displacement, velocity and acceleration amplitudes are respectively:

$$F = \left(\frac{N_0}{c \omega_f} \right) \left[R(\omega_f) \right]^{\frac{1}{2}}, \quad 2.70$$

$$\omega_f F = \left(\frac{N_0}{c} \right) \left[R(\omega_f) \right]^{\frac{1}{2}}, \quad 2.71$$

$$\omega_f^2 F = \left(\frac{N_0 \omega_f}{c} \right) \left[R(\omega_f) \right]^{\frac{1}{2}}. \quad 2.72$$

It is important to notice that in the steady state case where the response is due to the

driving term alone, the displacement, velocity and acceleration all have maximum response at slightly different driving frequencies. The displacement response curve is shown in Fig. 2.04, where the displacement amplitude peaks at the frequency slightly below the resonance ω_0 . The response curves all show large maxima at

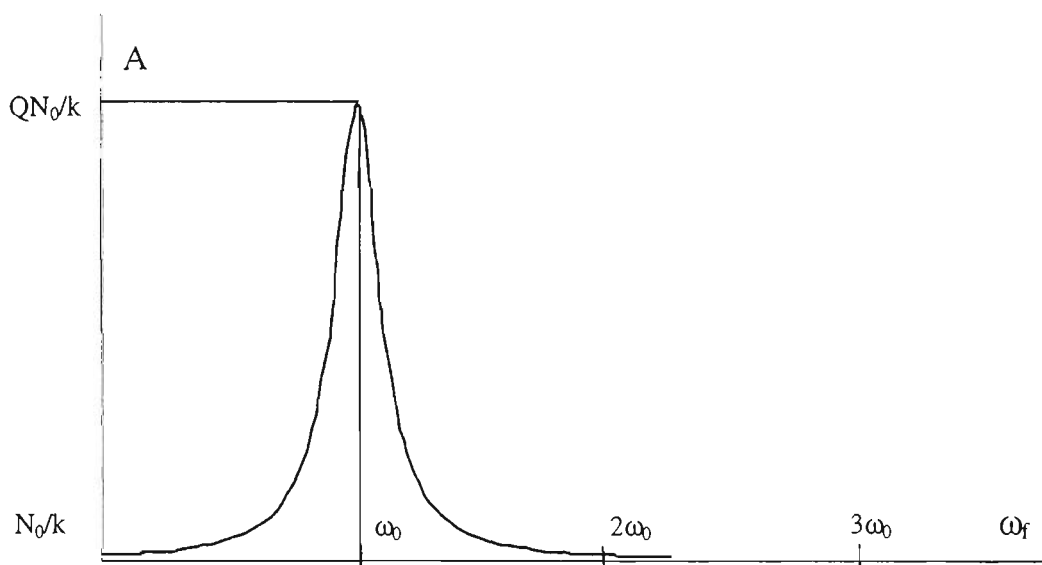


Figure 2.04: Response curve of the displacement amplitude

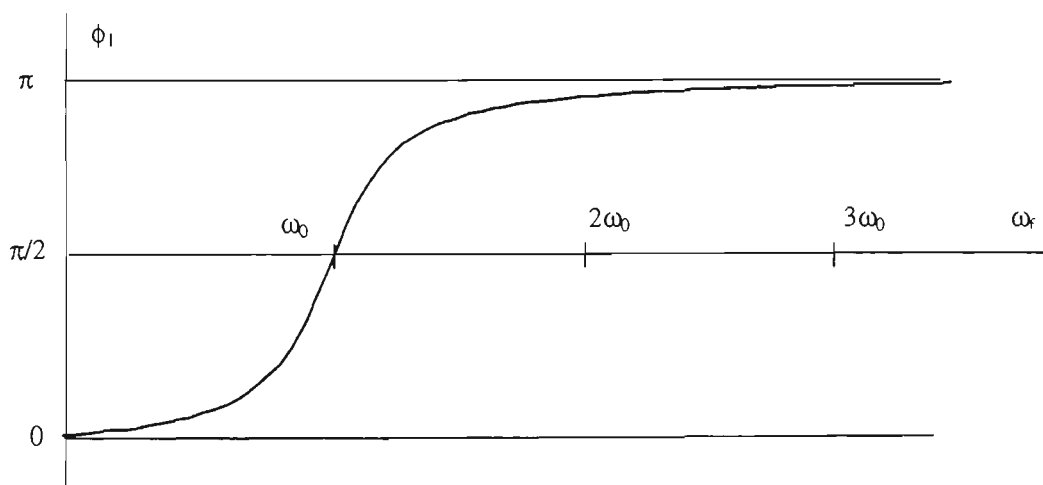


Figure 2.05: Variation of phase ϕ_1 with driving frequency

frequencies near the resonance frequency ω_0 . Since the velocity amplitude $\omega_f F$ is proportional to the square root of $R(\omega_f)$, it has its maximum value exactly at the resonance frequency ω_0 . The displacement amplitude F has ω_f in the denominator,

so F peaks at a frequency slightly below the resonance frequency and the acceleration amplitude $\omega_f^2 F$ contains ω_f in the numerator, and therefore peaks slightly above the resonant frequency ω_0 . The way, in which the phase constant ϕ_f changes with driving frequency, is shown for the same system in Fig.2.05. At the resonance frequency the phase constant is $\pi/2$, then the displacement lags the driving force by exactly 90° . Fig. 2.04 contains a resonance quality factor, Q , which is related to damping and is the measure of the lightness of damping. The quality factor Q can be expressed as the ratio of the amplitude of response at resonance to the displacement at $\omega_f=0$ if the force is applied statically (Pain 1993).

Thus from Eq.2.61 the Q factor is

$$Q(r) = \frac{F}{F_0} = \frac{1}{\sqrt{(1-r^2)^2 + (2\zeta r)^2}}, \quad 2.73$$

Plotting Q against r results in a family of curves which are dependent on ζ (Viersk 1979). In the resonance region the peak of the $Q(r)$ curve occurs to the left of the resonant value of $r=1$, for $\zeta \ll 1$ and near resonance it can be simplified as:

$$Q \approx \frac{1}{2\zeta}. \quad 2.74$$

Damping factor ζ cannot be measured directly but instead is deduced from the response curve of vibrating system. The response curve for a SDOF system (excited by a harmonic force of constant amplitude) can be plotted using the accurately measured values of displacement for all frequencies near resonance ($\omega_{\min} \leq \omega_0 \leq \omega_{\max}$), where ω_0 is the resonance frequency. The common method of determining damping from “half power bandwidth” is to measure the frequency bandwidth, between points on the response curve, for which the response is some fraction of the resonance response of the system. The usual convention is to

consider those points at frequencies where the amplitude of the response is $\frac{1}{\sqrt{2}}$ times the maximum response. The width at these points is frequently referred to as the “half-power bandwidth,” a term borrowed from the analysis of electrical systems in which amplitude is a measure of voltage and electrical power is proportional to the square of voltage.

For lightly-damped oscillators Q -factor is a measure of the sharpness of the resonance curve in the graph of power as a function of frequency ω_f , and has the value of

$$Q = \frac{\omega_0}{\gamma} = \frac{\omega_0}{\omega_2 - \omega_1}, \quad 2.75$$

where γ is the width of a power curve at half maximum height ($\gamma = \omega_2 - \omega_1$). It is also a measure of the energy stored in an oscillator compared to the rate of the energy input needed to maintain the oscillation:

$$Q = \frac{2\pi \times \Delta E}{E}, \quad 2.76$$

where ΔE is the stored energy, E is the energy input per cycle (or lost per cycle).

On the one hand the damping factor ζ can be determined by measuring the half power bandwidth

$$\frac{1}{Q} = \frac{\omega_2 - \omega_1}{\omega_0} = 2\zeta = \eta, \quad 2.77$$

where η is the loss factor. On the other hand the damping factor ζ can be found using decay time measurement. The damping factor can be determined by solving the equations Eq. 2.50 and Eq. 2.58, if decay time τ and damped frequency ω_d have been measured:

$$\zeta = \sqrt{\frac{1}{1 + \omega_d^2 \cdot \tau^2}}. \quad 2.78$$

It was shown (Main 1993) that the average power absorbed from the driving force when the system is driven with an angular frequency ω_f is

$$\mathbf{E} = \left(\frac{N_0^2}{2c} \right) R(\omega_f). \quad 2.79$$

The shape of the power absorption curve is essentially the shape of $R(\omega)$

$$\mathbf{E} = \frac{N_0^2}{2m\gamma} \left[\frac{\gamma^2 \omega_f^2}{(\omega_0^2 - \omega_f^2)^2 + \gamma^2 \omega_f^2} \right]. \quad 2.80$$

Thus γ is the size of the angular frequency range within which power is greater than half its maximum value \mathbf{E} (Fig. 2.06). It can be shown that for frequencies close to resonance ($\omega \approx \omega_0$) in a very lightly damped system, the response function may be approximated by Lorentzian lineshape (Main 1993)

$$L(\omega_f) = \frac{E_0}{1 + \left(\frac{\omega_f - \omega_0}{\gamma/2} \right)^2}, \quad 2.81$$

where E_0 is the amplitude, ω_0 is centre frequency and $\gamma/2$ is the half-width at half maximum of Lorentzian lineshape.

2.5.2.2 Energy flow in an oscillator

The maintenance of the steady-state vibration requires a sustained supply of energy by the driving force to replace the energy dissipated by the damping force. The forced term of the displacement is given by Eq. 2.59

$$y_f = F \sin(\omega_f t - \phi_1).$$

The work done against the damping force is $-F_d \Delta y$. The instantaneous power

absorption is

$$\mathbf{E} = -F_d \cdot \dot{y} = c \cdot \dot{y}^2 \quad 2.82$$

Where \dot{y} -velocity, F_d -damping force. Since the velocity \dot{y} varies harmonically and has amplitude $\omega_f F$, the average of \dot{y}^2 over a complete cycle is

$$\dot{y}^2 = \frac{1}{2} (\omega_f F)^2 = \frac{1}{2} \cdot \left(\frac{N_0}{c} \right)^2 R(\omega_f). \quad 2.83$$

Therefore

$$\langle \mathbf{E} \rangle = \left(\frac{N_0^2}{2c} \right) R(\omega_f) = \frac{N_0^2}{2m\gamma} \left[\frac{\gamma^2 \omega_f^2}{(\omega_0^2 - \omega_f^2)^2 + \gamma^2 \omega_f^2} \right]. \quad 2.84$$

The maximum value of $\langle \mathbf{E} \rangle$ reached at the resonance frequency exactly. The shape of the power absorption curve is essentially the shape of $R(\omega)$.

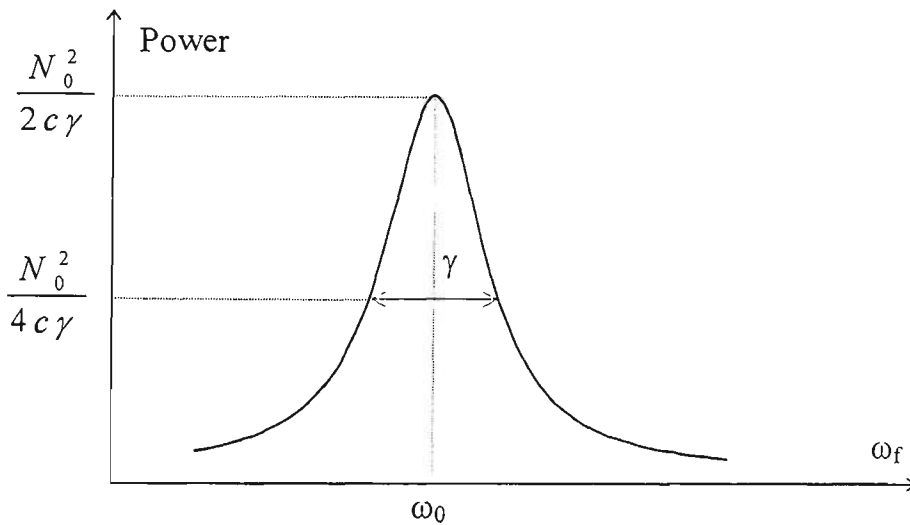


Figure 2.06: The average power absorption curve with γ (FWHM)

The average power absorbed from the driving force is proportional to the damping constant when the system is driven with an angular frequency ω_f . It can be seen from the diagram γ is the size of the angular frequency range, within which $\langle \mathbf{E} \rangle$ is

greater than half its maximum value. From Eq. 2.58 and Eq. 2.77 the width of the power absorption curve is identical with the energy decay constant for free vibrations of the system. Therefore either the measurements of resonance frequency and half power bandwidth by measuring the resonance curve or the measurements of decay time and resonance frequency permit to practically determine the damping factor of vibrating structure.

Chapter 3

EXPERIMENTAL ARRANGEMENT

Content:	Page
3.1 Introduction.....	3-2
3.1.1 The set-up diagram and description.....	3-2
3.2 Optical excitation system.....	3-4
3.2.1 Diode Laser for photothermal excitation of vibrations.....	3-4
3.2.2 Power Supply and Temperature Controller.....	3-5
3.3 Optical detection system.....	3-8
3.3.1 Interferometric sensor and homodyne technique.....	3-9
3.3.2 Signal processing.....	3-14
3.3.3 Detection electronics circuitry and feedback control. operation.....	3-15
3.4 The interferometer calibration procedure and performance.....	3-19

3.1 Introduction

All measurements described in this work were derived by using low power laser irradiation to excite vibration of a clamped-free cantilever. Cantilever was chosen as test structure because the simplicity with which it can be approximated by a concentrated mass and a single spring, representing a Single Degree of Freedom oscillator. The selected structure, an unpolished aluminium cantilever (Aluminium alloy 2024) with mass of 0.025 kg and dimensions 300 mm × 12 mm × 2.5 mm was clamped in a vice with mass of 5.28 kg. The cantilever length is much bigger than thickness ($L \gg h$); its displacement occurs in horizontal plane, that the influence of the gravitation force on flexural bending can be neglected. The aluminium has been chosen because of its large linear coefficient of expansion ($24 \times 10^{-6} \text{ K}^{-1}$) and high optical absorption. As far as the light absorption depth at optical frequencies in aluminium is roughly tens of nanometres, the calculated value of thermal diffusion length is $\sim 1.016 \text{ mm}$ (Hess 1989; Walsh and Culshaw 1991), the efficiency of optical excitation for aluminium is much higher than for stainless steel.

3.1.1 The set-up diagram and description

The vice with cantilever was mounted onto a breadboard ($\sim 40 \text{ kg}$), sitting on the top of a concrete bench ($\sim 200 \text{ kg}$). The bench with test structure was isolated of ground floor vibration by inflated tyres which were put under the legs. Apart from the cantilever mounted on translation stage the Set-Up (see Fig. 3.01) includes: the excitation part-on the right hand side of the cantilever and the optical detection part-on opposite side.

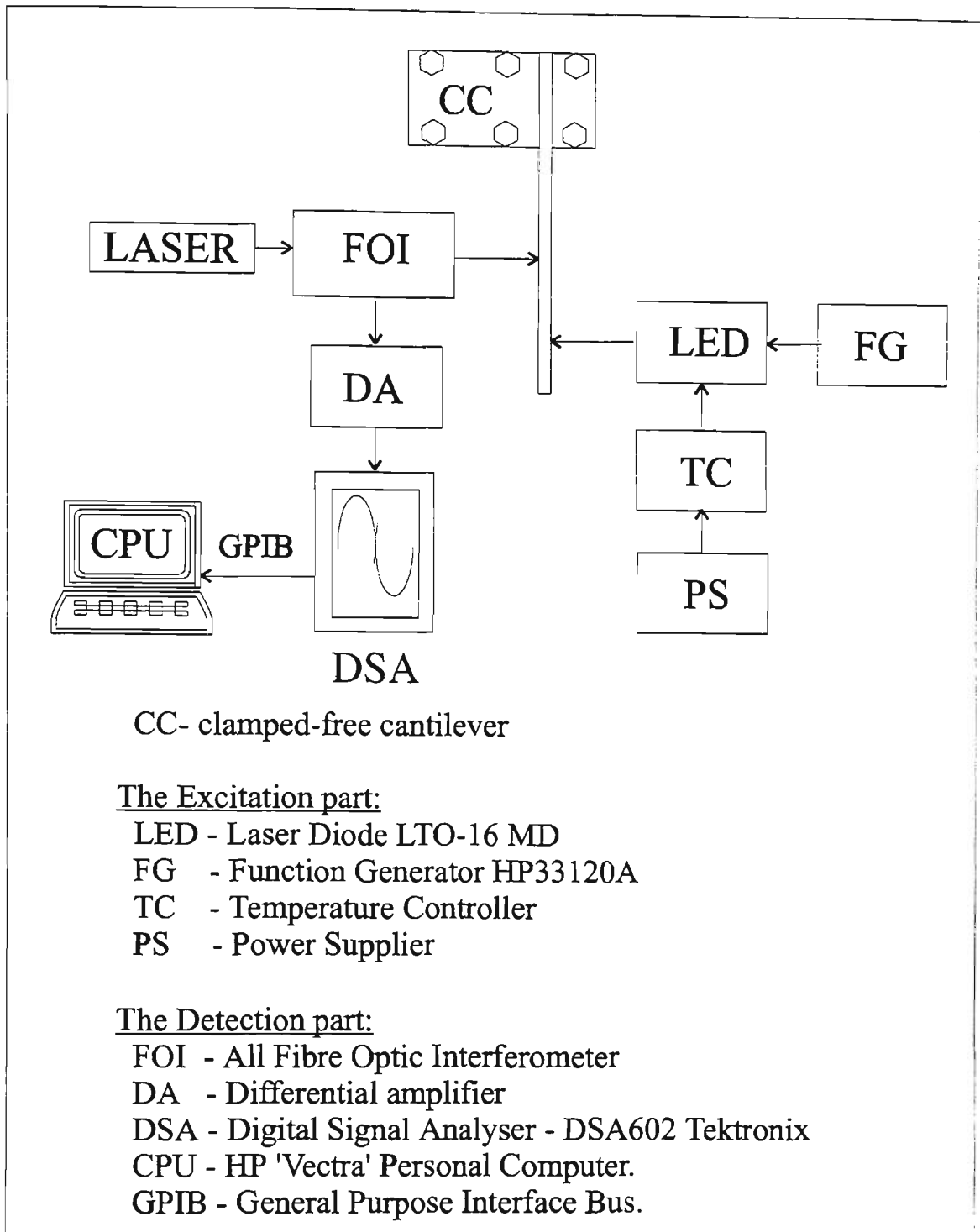


Figure 3.01: The experimental set-up diagram

3.2 Optical excitation system

The excitation part includes a low power diode laser (Sharp LT016MD), equipped with Power supply, to precisely control diode laser driving current by modulating voltage from Function Generator (HP33120A) and Temperature Controller to monitor and to keep diode laser temperature constant. Both instruments have been specifically constructed for this project.

3.2.1 Diode Laser for photothermal excitation of vibrations

A low power laser diode Sharp LT016MD, 810 nm and with 40 mW maximum output power was selected to excite vibrations in a test structure, because it is compact, provides sufficient output power and cost effective. Since the output power of a diode laser is a function of the current flowing across the active junction within a linear region of operation, the optical output can be modulated at very high frequencies and will linearly follow the analog waveform modulation of the drive current. The diode laser output power is controlled by the driver, which provides automatic power control by precise internal monitoring of the diode laser drive current. The diode laser output power was maintained at a maximum peak of 13.5 mW. By manually sweeping the laser diode modulation frequency near the calculated frequency of resonance, the cantilever has been driven into resonance. The diode laser could be positioned at any point of either side along the length of the cantilever. It was focused to a spot diameter of about 0.5 mm onto the target surface, using a 20^x microscope objective lenses. Since diode laser threshold current is dependent on temperature and assuming constant drive current, power may drop 10% per 1°C. Maintaining the power often includes the risk of

destruction. Since a diode laser operating life doubles with every 10°C reduction in temperature and conversely, halves with every 10°C increase, in addition to the power supply with precise control of driving current, a stand alone temperature controller (see Fig. 3.03) was designed to stabilise diode laser operating temperature and also to improve its reliability.

3.2.2 Power Supply and Temperature Controller

Two specific devices Power Supplier and Temperature Controller have been constructed to provide modulated output power of diode laser. The power supply circuitry (Fig. 3.02) has two current mirror sources and an operational amplifier to provide a stable voltage controlled current source. The diode laser current can be

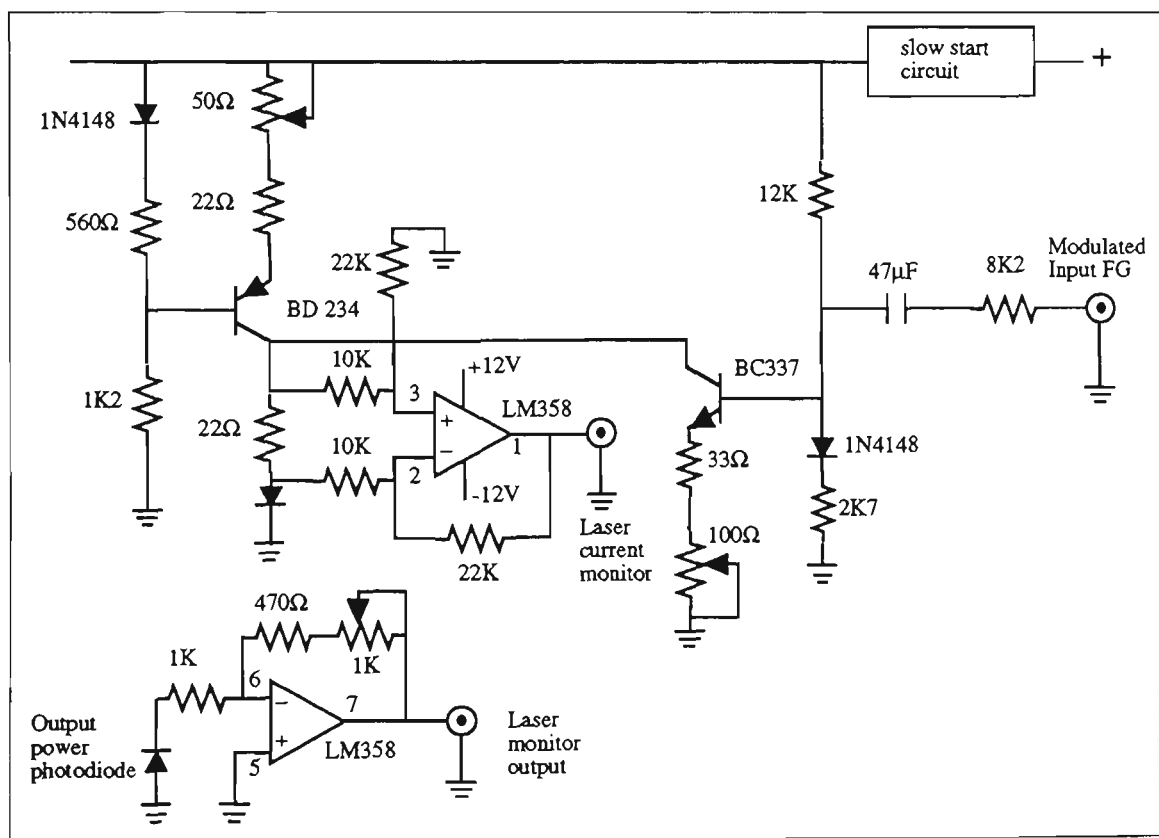


Figure 3.02: Diode laser power supply circuitry diagram

linearly modulated by any analog modulation waveform from function generator (square, sine or triangle) . The operational amplifier output voltage is used to monitor the diode laser driving current through BNC connector. The feedback signal from built-in photodiode, that senses the back facet emission from the laser, has another BNC connector to control laser diode output power. As the spikes produced even when a normal DC supply is switched on or off are sufficient to damage many diodes, the power supply also provides the automatic smooth current ramps during power-on and power-off. For all measurements in this work the diode laser was modulated using Sine waveform signal from Function Generator.

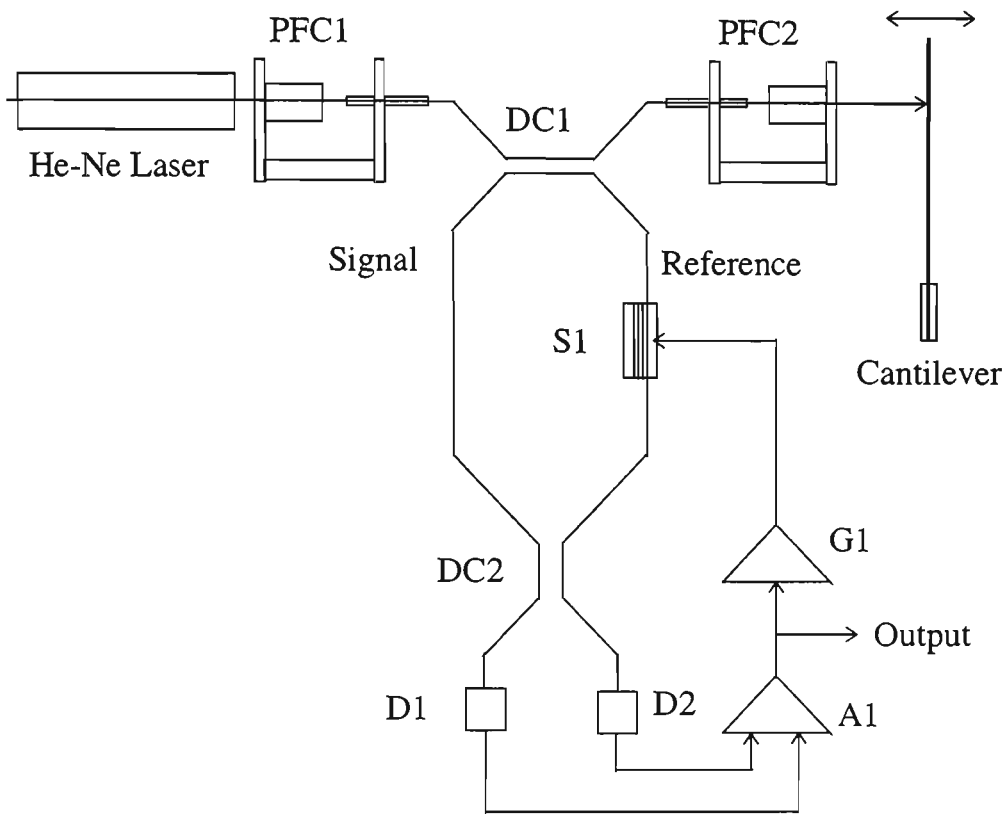
The Temperature Controller (Fig. 3.03) has been built to stabilise diode laser temperature over the range from -55°C to $+150^{\circ}\text{C}$ by accommodating an integrated circuit sensor such as Analog Device AD-590, whose output is $1\ \mu\text{A}/^{\circ}\text{K}$. The diode laser trimmed to $\pm 0.5^{\circ}\text{C}$ of calibration accuracy. The instrument displays the set point, which has been set by voltage output from the voltage follower and actual temperature in degrees of Celsius, using digital meter and LED indicators, showing less or more, than reference temperature. The diode laser has an in-built Peltier device, which was mounted in close proximity to the diode laser and which acts as a heating or cooling element, according to the direction of current flow. If the diode laser temperature falls out-of-range, then a voltage develops across the Peltier

device, that the current attempts to maintain the normal operating temperature by heating or cooling.

3.3 Optical detection system

The detection part of set-up includes the laser source, Fibre Optic Interferometer of Mach-Zehnder configuration with detection electronics (see Fig. 3.04). The Silicon detectors OPF480 convert an optical output to electrical signal, which after amplification and differentiation is transforming from time domain to frequency based by Digital Signal Analyser DSA602 with FFT display. All measurements were obtained in the form of the displacement response curves (Displacement versus Driving frequency) or as the recorded waveforms, which have been stored on disks using HP-Basic written program for data transfer from DSA to an CPU drive storage through the standard GPIB interface. Light from 632.8 nm He-Ne laser with output power of ~ 2 mW (Model-117A, Spectra Physics) is coupled into a single mode fibre by precision fibre coupler assembly Newport MF915T (PFC1). After input coupling, the light is then split into the two arms of the interferometer by a 2x2 fibre optic directional coupler (DC1) in two beams of equal intensity. First beam collimated by precision fibre coupler assembly (PFC2) is incident on the surface of the cantilever, the part of the beam reflected back into the coupler forms the signal part of light power. The reference part from the directional coupler (DC1) after being passed through the Phase shifter (S1) recombines with the signal part of the power in second fibre optic directional coupler (DC2). Any change of the distance between the sensing fibre tip and the vibrating reflective surface varies

the optical path length of the signal and the reference arms and causes phase modulation of the interferometer output signal.



PFC1/2-precision fibre couplers, DC1/2-directional couplers, D1/2-detectors,

A1-Operational Amplifier, S1-PZT stretcher, G1-integrator

Figure 3.04: The optical detection part with Mach-Zehnder interferometer as a sensor

3.3.1 Interferometric sensor and homodyne technique

Since photodetectors respond to the light irradiance, they cannot measure the difference in phase directly. But when two signals from the reference and signal arms interfere, the phase difference determines the amplitude of the light in the two fibres leaving the second directional coupler. In this way, a phase modulation of the

light in the signal fibre is converted to an amplitude modulation, whose square is then recorded as an irradiance at the detector. A key element to the interferometric sensor is the optical fibre directional coupler (3dB), its ability to convert phase shifts into amplitude variations. For these couplers if we assume the power coupling coefficients of the two couplers are K_1 and K_2 , then the output of the interferometer from the signal (E_s) and reference (E_r) arms are (Udd 1991)

$$E_r = E_0 \sqrt{K_1 K_2} \cos(\omega_{c0} t + \phi_r), \quad 3.01$$

$$E_s = E_0 \sqrt{(1 - K_1)(1 - K_2)} \cos(\omega_{c0} t + \phi_s). \quad 3.02$$

The output intensity of the interferometer can be expressed as

$$I = \langle E_r^2 \rangle + \langle E_s^2 \rangle + \langle E_r E_s \rangle, \quad 3.03$$

where $\langle \dots \rangle$ denotes a time average over a period much longer than an optical period ($2\pi/\omega_{c0}$). By combining 3.01, 3.02 and 3.03 we obtain the output from one of the interferometer arms as

$$I = I_0 \left[K_1 K_2 + (1 - K_1)(1 - K_2) + 2\sqrt{K_1 K_2 (1 - K_1)(1 - K_2)} \right] \cos(\phi_r - \phi_s) \quad 3.04$$

and for 3dB couplers $K_1 = K_2 = 1/2$, so that

$$I_1 = I_0 \left[\frac{1}{2} + \frac{1}{2} \cos(\Delta\phi) \right], \text{ where } \Delta\phi = \phi_r - \phi_s \quad 3.05$$

where $\Delta\phi = 2\pi/\lambda \cdot \Delta L$, ($\Delta L = L_r - L_s$) is the optical path length difference between the signal and reference arms of the interferometer. The output of the other arm of the 3dB coupler is complementary to Eq. 3.05:

$$I_2 = I_0 \left[\frac{1}{2} - \frac{1}{2} \cos(\Delta\phi) \right]. \quad 3.06$$

The outputs from the two ports are 180° out of phase with each other. It should be noted that two effects have been ignored in this consideration, the effects of source coherence and polarisation effects. Source coherence refers to the property of light to form interference patterns. If the light beam is divided into two, one part delayed relative to the other and then recombined, an interference pattern will form as illustrated in Fig. 3.05:

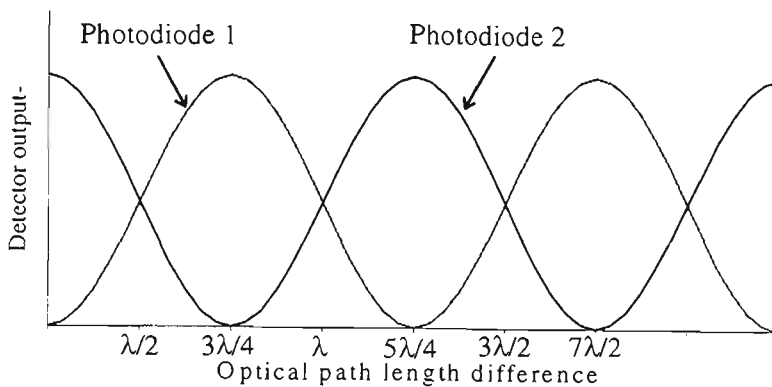


Figure 3.05: Interferometric output

After a time delay τ , there remains a definable phase relationship between the two beams. Depending on this phase relationship a range of output intensities of the two mixed beams

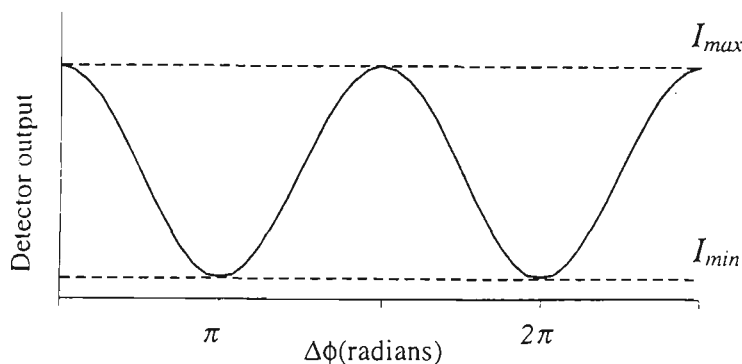


Figure 3.06: Fringe visibility in one arm of an interferometer

is obtained between minimum (out-of-phase) and a maximum (in-phase) in Fig. 3.06. To include the effects of coherence and polarisation vectors of the signal and reference beams Eq. 3.06 can be rewritten as:

$$I_2 = I_0 \left[\frac{1}{2} - \frac{1}{2} \gamma_v \cos \Theta \cos(\Delta\phi) \right], \quad 3.07$$

where γ_v is the measure of fringe visibility for a path length difference, and Θ is the angle between the two polarisation vectors. For short path length differences between the arms $\gamma_v=1$, ie. short compared to the coherence length ($L_c=c\tau_c$), for large path mismatches, τ_c is inversely related to the frequency linewidth of the laser and increases as the linewidth decreases. For larger τ_c or narrower linewidth lasers, interference patterns can be obtained for larger path length differences between the beams. Thus for sensors it implies larger path length differences may be tolerated between the signal and reference arms. Fringe visibility is defined as

$$\gamma_v = \frac{I_{\max} - I_{\min}}{I_{\max} + I_{\min}}, \quad 3.08$$

It should be mentioned here that coherence length for two types of laser sources used in this work is sufficient to match the length difference of reference and signal arms of the interferometer. For He-Ne 632.8nm “Uniphase” Laser Mode spacing

$$\Delta\nu = 438 \text{ MHz (Newport Catalogue 1995),}$$

$$\Delta\nu = c/2L_c, \text{ thus}$$

$$L_c = c/2 \cdot \Delta\nu = 3 \cdot 10^8 / 2 \cdot 438 \cdot 10^6 = 0.3425(\text{m}),$$

For He-Ne 632.8nm “Spectra Physics” 117A Model Laser Mode spacing 473.6 THz, and similar calculation gives the value of L_c more than 31 m. A very small displacements of the oscillating cantilever that is to be measured induce a very small phase change $\Delta\phi$ in the order of 10^{-4} - 10^{-6} μrad in the Eq. 3.5, which results large changes in the output intensity of the detector. For maximum fringe visibility Θ should be as small as possible and as $\Theta \rightarrow \pi/2$, total loss of the signal occurs. The sensitivity of the sensor (Eq. 3.09) is dependent on the phase difference and will be a minimum for $\Delta\phi \rightarrow 0$, which is the expected signal level.

$$\frac{dI}{d(\Delta\phi)} = \frac{d[\text{Cos}(\Delta\phi)]}{d(\Delta\phi)} = \text{Sin}(\Delta\phi) \rightarrow 0, \quad 3.09$$

This is shown in Fig. 3.07:

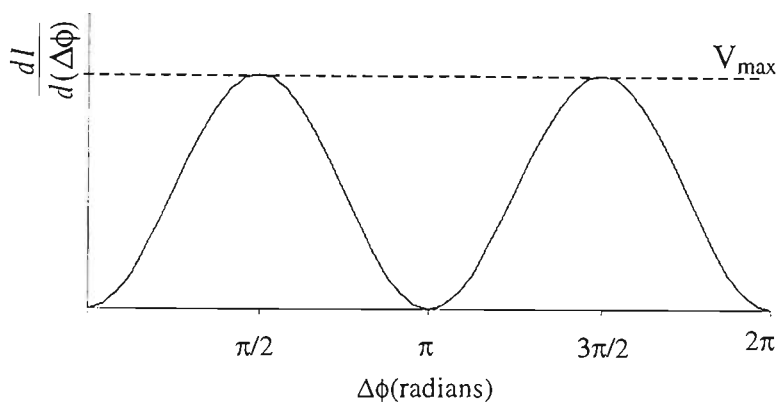


Figure 3.07: Sensitivity vs phase difference between two arms of the interferometer

From the diagram the highest sensitivity is achieved when one arm of the interferometer is set, or biased to an odd multiple of $\pi/2$, then for small excursions around this point sensitivity is maximised. This is referred as the quadrature point. Many factors such as temperature and pressure variations may cause the fibre to elongate and therefore may cause the path length difference between the reference and signal arms of the interferometer to drift with time. This will cause the sensor

phase shift $\Delta\phi$ to vary in and out of the maximum sensitivity points as $\Delta\phi$ takes on many values of π . For homodyne sensors this control is usually realised by placing a phase shifter in the reference arm to control its length. This device is fabricated by wrapping optical fibre around a piezoelectric cylinder. When excited by a feedback correction voltage the cylinder expands and stretches the fibre and consequently its increased length induces a phase shift in the light propagating in it. When the optical path length of one arm of the interferometer is modulated by a signal ϕ_s of frequency ω_s , the optical phase difference between the optical beams $\phi(t)$ may be written as

$$\phi(t) = \phi_d + \phi_s \sin \omega_s t, \quad 3.10$$

where ϕ_d is slowly varying thermal phase shift, and ϕ_s is the signal phase amplitude.

3.3.2 Signal processing

As it was shown in previous section the sensitivity of the interferometer to an induced optical phase change is not constant, due to the natural periodicity of the transfer function. This variable sensitivity is not acceptable in most sensor applications, as it causes signal fading. Linearisation of the interferometric sensor's transfer function has been achieved by a variety of different techniques. One of the most effective technique designed to recover the input signal modulating the relative phase in the interferometer $\phi_s \sin \omega_s t$ is to use a piezoelectric based fibre optic phase modulator (Jackson *et al.* 1980). In this technique the phase modulator is incorporated in the reference arm and forms part of a feedback loop to maintain

the interferometer locked at its point of maximum sensitivity (quadrature point), where $\phi_d=(2n+1)\pi/2$.

3.3.3 Detection electronics circuitry and feedback control operation

The interferometer outputs Eq. 3.05-3.06 may be rewritten (Dandridge A., 1991):

$$I_1 = \frac{I_0}{2} [1 + \text{Cos}(\phi_d + \phi_s \text{Sin} \omega_s t)], \quad 3.11$$

$$I_2 = \frac{I_0}{2} [1 - \text{Cos}(\phi_d + \phi_s \text{Sin} \omega_s t)]. \quad 3.12$$

These intensity outputs are then converted to electrical currents by a photodetector.

Differential combination of these photocurrents produces an output

$$i = \epsilon_r I_0 \text{cos}(\phi_d + \phi_s \text{sin} \omega_s t), \quad 3.14$$

where ϵ_r is the responsivity of the photodetectors,

$$\begin{aligned} \text{Cos}(\phi_d + \phi_s \text{Sin} \omega_s t) = & \left[\text{Cos} \phi_d \left(J_0(\phi_s) + 2 \sum_{n=1}^{\infty} J_{2n}(\phi_s) \text{Cos}(2n \omega_s t) \right) - \right. \\ & \left. - \text{Sin} \phi_d \left(2 \sum_{n=0}^{\infty} J_{2n+1}(\phi_s) \text{Sin}[(2n+1) \omega_s t] \right) \right], \end{aligned} \quad 3.15$$

and $J_n(\phi_s)$ is the Bessel function of order n . Under normal operating conditions ϕ_d fluctuates randomly in time due to temperature changes, causing the amplitude of the Bessel components to fluctuate in a similar manner. In order to hold the average value of $\Delta\phi = \pi/2$, that is $\Delta\phi = \phi_d + d\phi_s - \phi_c = \pi/2$, where ϕ_c is the applied control phase shift to the piezoelectric transducer. The interferometer output given by Eq. 3.04 may be written as:

$$i = \varepsilon_r I_0 \cos(\phi_d + d\phi_s - \phi_c). \quad 3.16$$

At this point i is zero at the quadrature point, and small deviations from quadrature are given by

$$\Delta(i)_{\pi/2} = -\varepsilon_r I_0 \cos(\phi_d + d\phi_s - \phi_c). \quad 3.17$$

Since this is zero at desired quadrature condition and experiences a sign change passing through quadrature, it is an ideal error signal from the view point of linear control theory. If an appropriate feedback voltage is applied to the piezoelectric element controlling ϕ_c , then ϕ_c can be made to exactly cancel $(\phi_d + d\phi_s)$, thus driving the error signal to zero. Such a feedback signal is the integral of i , amplified by an appropriate gain factor g (Eq.3.18):

$$dV_{fb} = g \int_0^{\tau} i(t') dt', \quad 3.18$$

where g is the amplifier gain. The modulating signal $\phi_s \sin \omega_s t$ can be directly recovered from the feedback signal dV_{fb} , provided ω_s is less than the bandwidth of the servo. The tracking range of active homodyne signal processing is limited by the maximum voltage generated in the feedback loop. So the drawback of this technique is that the piezoelectric phase shifter has to be periodically reset to zero when it approaches its maximum voltage and this reset may occur often if the sensor is used in non-laboratory environments. The detection electronics circuit diagram (Fig. 3.08) was built using off the shelf components. Two OPF480 silicon photodetectors were used to detect the optical signals and produce currents proportional to light intensities. They feed two NE5532 transconductance

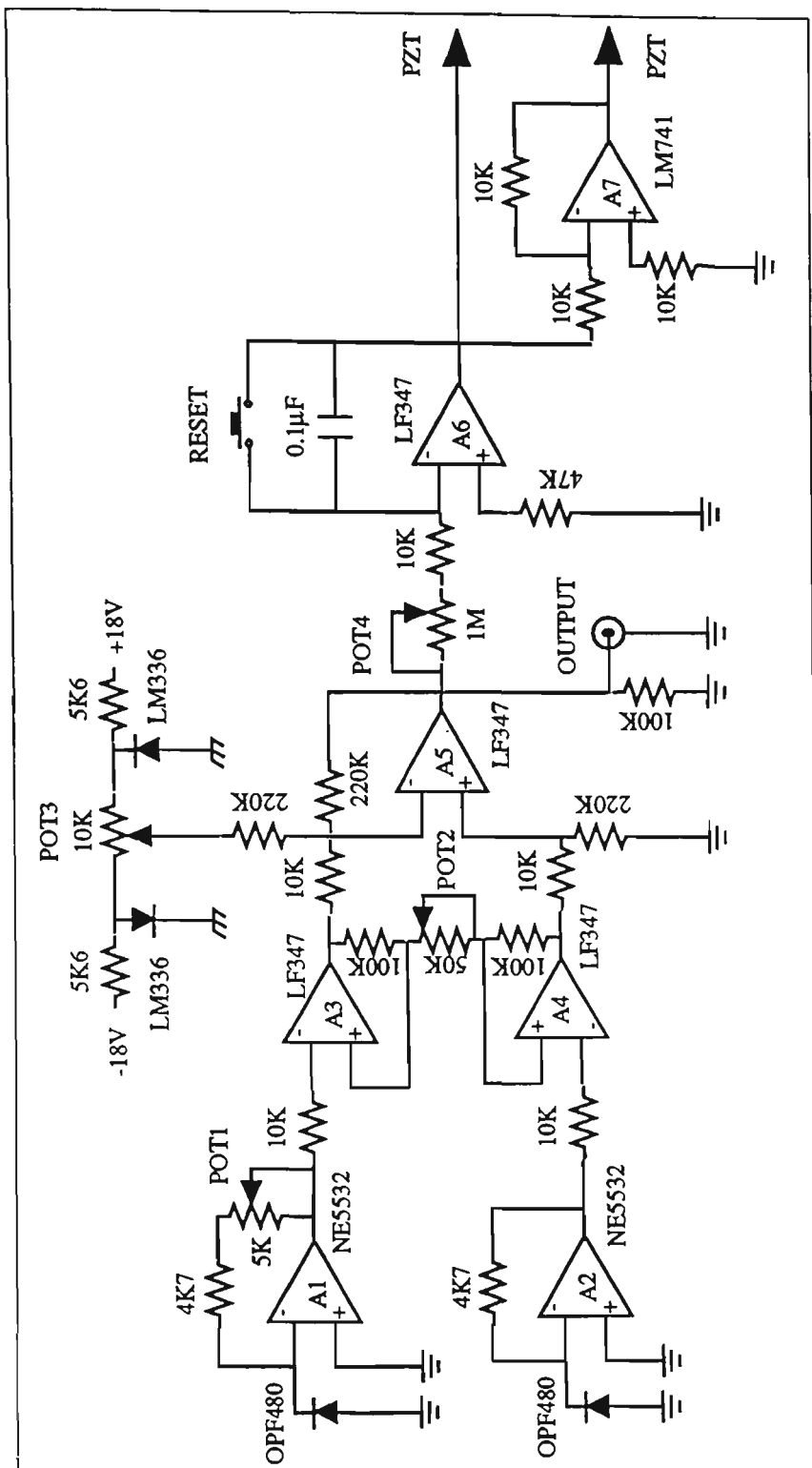


Figure 3.08: Detection electronics circuitry

amplifiers. The differential output signal after subtraction in two operational amplifiers LF347 is undergoing further amplification in third LF347 by combination of two resistances 10 ohm and 220 ohm. The integration has been implemented by the next LF347. And further on the operational amplifier LM741 provides an antiphase correction voltage. Finally the feedback correction signal has been applied to the piezoelectric shifter to track out the interferometer drift. The electronic circuitry was powered by $\pm 18\text{V}$ Laboratory DC Power Supply with dual tracking (GPQ3030). The phase shifter was fabricated by wrapping 15 turns of single mode fibre around a piezoelectric cylinder (Tokin XOZ-138) with 3.8 cm of outside diameter and piezoelectric coefficient $\sim 4 \cdot 10^{-10}$ m/volt. The optical fibre turns have been attached to the PZT using Araldite adhesive. The feedback correction voltage through the piezoelectric effect causes the radius of the cylinder to expand or contract by an amount:

$$\Delta r = d_p \cdot V_c, \quad 3.19$$

where d_p is the piezoelectric coefficient ($\sim 4.02 \cdot 10^{-10}$ m/Volt), V_c the correction signal. As the fibre is attached to the cylinder, it will be stretched by cylinder expansion (the DC level of applied voltage can be adjusted to ensure that the cylinder does not contract or compress below its rest state) and its increased length will induce a phase shift in the light propagating in it. The fibre length extension is given by

$$\Delta l = 2\pi\Delta r \cdot \frac{L}{t}, \quad 3.20$$

where L is the length of the windings on the cylinder and t is the fibre outer diameter so that $L/t=N$, the number of turns.

For $t=125 \mu\text{m}$, $\lambda= 632.8 \text{ nm}$, $N =15$ turns and using

$$\Delta\phi = \frac{2\pi}{\lambda} \Delta l, \quad 3.21$$

then $\Delta\lambda$ can be written as $\Delta\lambda=\lambda/\Delta l$, we obtain

$$\Delta l \cong (2\pi \cdot 4 \cdot 10^{-10} \cdot 15) \times V = 377 \cdot 10^{-10} \times V(\text{m}) = 0.0377 \times V(\mu\text{m}),$$

$$\Delta\phi = 2\pi(377 \times 10^{-10}/632.8) \times V(\text{rad/Volt}) = 2\pi(0.0596) \times V(\text{rad/Volt}),$$

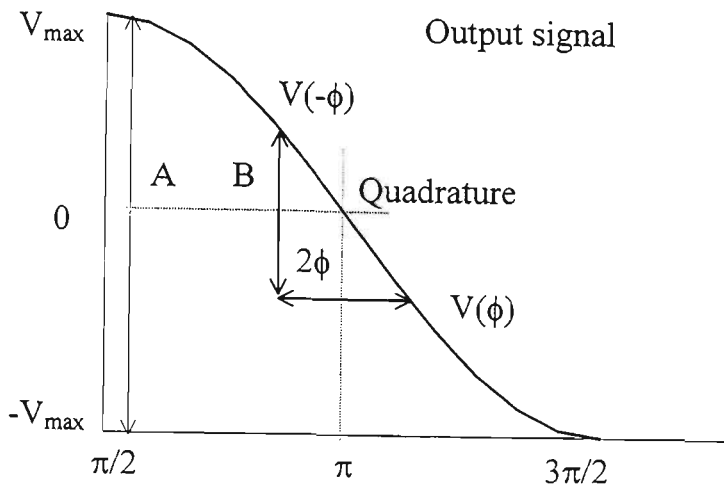
so $\Delta\phi \sim 2\pi$ phase shift can be provided by relatively small value $\sim 16.8\text{V}$ of feedback correction voltage.

3.4 The interferometer calibration procedure and performance

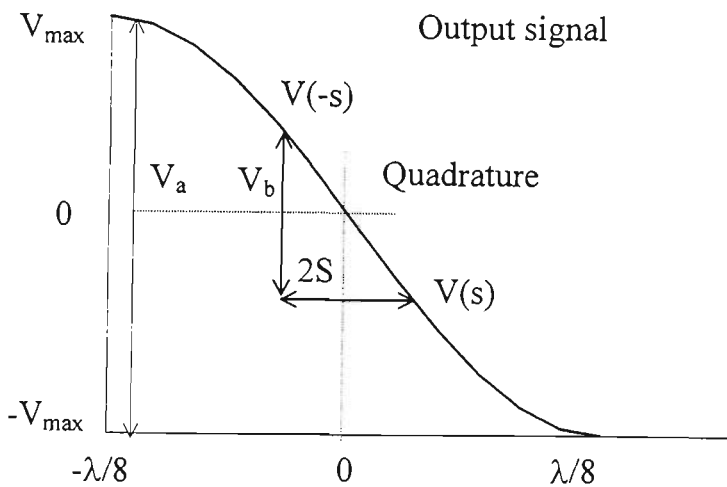
The interferometer was calibrated using a Piezoelectric mirror shaker (MB-ST/500/3) with resonant frequency $>5 \text{ kHz}$, which has been mounted onto the breadboard replacing the cantilever, that is the light reflected from the mirror was coupled back into the signal arm of the interferometer. The PZTS was biased at $+250 \text{ V DC}$. The signal frequency of 140 Hz (Sine waveform) was set to drive the mirror shaker into vibration. The AC amplitude of mirror shaker driving voltage was gradually increased from zero to maximum, when the interferometer output signal has reached 3.44 V , and any further increase in mirror shaker driving voltage resulted in the second harmonic term coming up. At this point the corresponding mirror displacement was equal to one eighth of the laser wavelength ($632.8\text{nm}/8=71.9 \text{ nm}$). With the interferometer locked into the quadrature condition the output signal $V(t)$ is given by:

$$V(t) = V_0 \text{Sin}[\pi + \phi(t)], \tag{3.22}$$

where $\phi(t)$ is the phase induced modulation due to vibration amplitude and V_0 is



A. Output signal phase difference



B. Mirror displacement amplitude.

Figure 3.09: Phase modulation and displacement amplitude

the maximum peak-to-peak output signal voltage of the interferometer as shown in

Fig. 3.09 $V_0 = 2V_a$, when $\phi(t) = \pm\pi/2$.

For any phase modulation about the quadrature point less than $\phi(t) = \pm\pi/2$, one can obtain:

$$V_b = V_a \sin(\pi - \phi) - V_a \sin(\pi + \phi), \quad 3.23$$

$$\phi = \sin^{-1}\left(\frac{V_b}{V_a}\right). \quad 3.24$$

The phase shift is related to the mirror amplitude S by $\phi=4\pi S/\lambda$, where λ is the interferometer wavelength. Therefore, the mirror amplitude can be determined by:

$$S = \frac{\lambda}{4\pi} \sin^{-1}\left(\frac{V_b}{V_a}\right). \quad 3.25$$

The displacement $\lambda/8$ was reached with a peak mirror driving voltage of 12.8 V, and the corresponding interferometer peak of output signal was 3.44 V. Then the AC component of the mirror driving voltage was gradually reduced until the interferometer output signal reached minimum of 0.032 V, which is equal to background noise level (under quiet laboratory conditions). The interferometer performance is usually measured by Noise Equivalent Displacement (NED), which is the RMS amplitude of the signal when Signal-to-noise ratio (SNR) is 1:1. It was found that in terms of minimum detectable displacement the calculated NED value is 0.17×10^{-9} m. This is the fundamental limitation for the particular interferometer. The Fibre Optic interferometer has exhibited an amplitude sensitivity of 5.3 nm/V for signal detection, based on a practical SNR of 1:1. It should be noted that minimum 32 mV noise floor level was achievable during short interval of very quiet time around midnight. The common noise floor level under noisy environmental conditions was significantly higher about 180-200 mV. When this is taken into account, the minimum practical displacement, which can be detected by the interferometer under these conditions is about an order of

magnitude greater than NED. The bandwidth of the detection electronics was measured as 200 KHz.

Chapter 4

EXPERIMENTAL RESULTS AND DISCUSSION

Content:	Page
4.1 Introduction.....	4-2
4.1.1 Response function in vibration analysis and processing of measured data.....	4-3
4.1.2 The accuracy of resonant frequency measurement.....	4-4
4.2 Description of the procedure used for measurements.....	4-6
4.3 Response measurements with a rigid cantilever securely fastened to the mounting bench.....	4-10
4.3.1 Response measurements under favourable laboratory (Conditions A).....	4-11
4.3.1.1 Resonance measurements for Mode1.....	4-12
4.3.1.2 Resonance measurements for Modes 2-5.....	4-19
4.3.1.3 Vibration parameters obtained using Lorentzian fits for Modes 1-5.....	4-24
4.3.1.4 Decay time measurements by waveform sampling: Modes 1-3.....	4-26
4.3.1.5 Variations in resonant frequency due to temperature changes.....	4-35
4.3.2 Day time measurements under less favourable laboratory conditions (Conditions B and C).....	4-36
4.4 Measurements with increased damping.....	4-44
4.5 Summary.....	4-50

4.1 Introduction

In general a three-dimensional structure can be characterised by physical properties such as the Young's modulus, shear modulus, bulk modulus and mass distribution (Nashif *et al.*, 1985). If a force vector $\bar{N}(t)$ is applied at an arbitrary point 1(x_1, y_1, z_1), it will generate a response vector \bar{F} at an arbitrary point 2(x_2, y_2, z_2). The magnitude of \bar{F} will be proportional to the magnitude of $\bar{N}(t)$ for a linear system, but the direction of \bar{F} will depend on physical properties of the structure and the three components of \bar{N} (N_x, N_y, N_z). Similarly a moment $\bar{M}(t)$, comprising three components M_x, M_y, M_z , will have a corresponding response vector \bar{F} . The principle of superposition applies for linear systems so that responses from two or more inputs may be added as vectors. The usual aim of vibrational analysis is to predict \bar{F} given \bar{N} or \bar{M} . For stationary structures, which do not rotate, the amplitude of the harmonic response $\bar{F}(t)$ can increase infinitely at some specific frequencies unless non-linear factors such as damping come into play to limit the amplitude. This limitation occurs through finite levels of energy dissipation, at one or more points in the structure, which increase with the second or greater power of amplitude. For low levels of damping, the specific frequencies at which high resonant amplitudes occur are called the natural frequencies of the structure. These frequencies and the corresponding distributions of amplitude are global properties, which do not depend on the exact points at which \bar{N} (or \bar{M}) are applied. The amplitude distributions at the natural frequencies are known as the natural modes of vibration.

4.1.1 Response function in vibration analysis and processing of measured data

The transverse vibration of a cantilever shows a harmonic response at some point caused by a single harmonic force or bending moment (e.g. a thermal bending moment produced by absorption of laser energy) applied to the structure at some other point. As seen in Chapter 2, the variation of the response with driving frequency can be described in terms of a normalised response function or response curve ($R(\omega)$) which is approximately Lorentzian for small deviations between driving frequency and resonant frequency. As shown in Eq. 2.70 - 2.72, only the squared velocity response strictly follows a Lorentzian function. The squared displacement and acceleration responses contain an extra ω^2 term in the denominator and numerator respectively. Generally, these variations are not significant for small deviations from resonance. They are even less significant if one is only trying to determine small shifts in the maxima of the response curves. However, they were allowed for in the data processing since the fundamental resonant frequency of the cantilever used was only about 22.5 Hz. The optical fibre interferometer measures displacement amplitude and the data is processed by first squaring the measured response for a particular frequency, then multiplying by ω^2 and then fitting a Lorentzian curve to the processed data using curve fitting software (TableCurve 2D). This software determined the central frequency ω_0 and half power bandwidth (HPBW) γ of the resonance together with their standard deviations. This processed data is proportional to $(\omega A)^2$ and so it just represents the power as a function of frequency. In the figures of this Chapter, measured and

processed data are distinguished by the units on the ordinate axes (voltage or power).

4.1.2 The accuracy of resonant frequency measurement

In the early measurements using the low power optical excitation and sensing technique, Philp and Booth (1994) determined the resonant frequency from the peak in the amplitude response as measured by the interferometer. They measured the frequencies to an accuracy of ± 0.5 Hz. This was the stability of the simple oscillator used to modulate the laser diode. For the results presented in this chapter, the amplitude resolution was higher since the interferometer was more sensitive (low noise electronics) and it used a shorter wavelength laser (633 nm instead of 1523 nm). In addition the frequency resolution possible was very much higher as the laser diode was modulated using an oscillator with a frequency resolution of 10 μ Hz (or 10 digits) and a stability of better than 2 ppm/ $^{\circ}$ C.

In general very small changes in physical or mechanical properties of the structure will cause changes in vibrational parameters such as natural frequency, damping and vibrational profile. The actual vibrational profile of a vibrating structure is difficult to measure accurately and so measurements of this have not been attempted in this thesis. However, resonant frequency and damping are relatively easily measured and this chapter examines the accuracy with which each of these parameters can be determined from the optical measurements. Resonant frequency has been measured in two ways. The first involves slowly stepping the frequency of the laser diode excitation through resonance while recording the amplitude of the resulting vibration at each frequency. In this way the resonance curve can be

plotted and the resonance frequency determined from the maximum of the curve. The second method involved tuning the LD modulation to obtain maximum response (resonance), driving the structure to vibrate by excitation at this frequency, then turning off the excitation and recording the slowly decaying vibration as a function of time (over a large number of cycles). The resonant frequency can be determined by fitting a damped sine wave to this data and determining the frequency of this wave. The damping can be determined from the decay constant of this damped free vibration data or from the HPBW of the resonance curves. Clearly the accuracy with which measurements can be made will depend on the resolution of the interferometer and data recording system and, in the case of the resonance curve measurements, the frequency stability and resolution of the function generator used to modulate the laser diode.

For the case of the resonance curve measurements, the question arises as to how small a change in resonant frequency can one determine? This will depend on the sharpness of the resonance. One conservative estimate of the minimum frequency shift which can be detected is obtained by considering the shift to be readily resolved if it is at least equal to the full-width of the resonance. This situation is shown schematically in Fig. 4.01. Two frequencies ω_1 and ω_2 can be resolved if the difference $(\omega_2 - \omega_1)$ is at least equal to the half power bandwidth, γ . Clearly, measurement of small frequency shifts will require high- Q , low-loss resonances. While the last statement is always likely to be true, the minimum frequency shift which can be detected is considerably better than that shown in Fig. 4.01 if one knows the functional form of the resonance curve. Fitting of the known Lorentzian curve to the resonance data allows one to estimate the resonance frequency

parameter to an accuracy which is determined by the number of data points, the signal-to-noise ratio of the measurements and the stability of the resonance being measured (drift). This chapter presents measurements with and without the fitting of the Lorentzian curve to show the magnitude of the improvement, which is obtainable when the functional form is known.

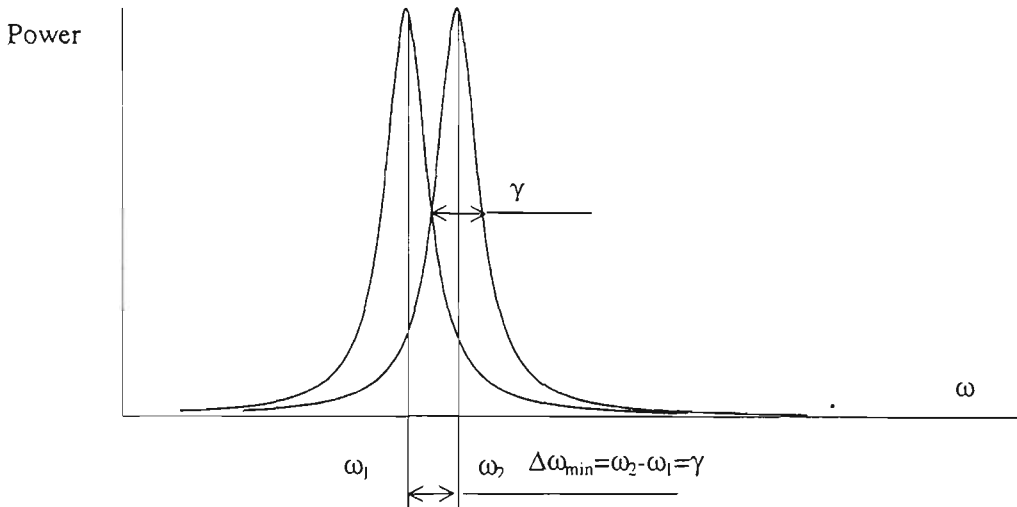


Figure 4.01: The resolution of two adjacent frequencies or a frequency shift.

4.2 Description of the procedure used for measurements

The laser diode excitation system, the fibre interferometer and the cantilever structure used for measurements were described in Chapter 3. Chapter 2 briefly discussed modal shapes but did not discuss the implications of the vibration profiles in terms of optimum position for excitation and displacement measurement so that many modes can be simultaneously excited and recorded. This section discusses this aspect and also describes the manner in which the measurements were made.

As has previously been stated, most of the experimental results described in this thesis were obtained in the form of cantilever displacement amplitude data as a function of driving frequency. The laser diode was sinusoidal-modulated at an appropriate frequency with a peak-to-peak output of up to about 25 mW. This beam was focused using a 20× microscope objective to a centrally-located spot of about 0.4 mm^2 area on the surface of the cantilever at a suitable distance from the clamp. Initially the natural frequencies of first five vibration modes were calculated by Eq. 2.28 using physical and mechanical properties of the cantilever material (Aluminium Alloy-2024). These parameters are summarised in Table 4.01. The values of calculated natural frequencies of Modes 1-5 are given in Table 4.02.

Table 4.01: The properties of the cantilever material (Aluminium Alloy-2024)

No	Property	Symbol	Numerical value
1	Density	ρ	$2770 \text{ kg}\cdot\text{m}^{-3}$
2	Thermal conductivity	k	$177 \text{ W}\cdot\text{m}^{-1}\cdot\text{K}^{-1}$
3	Thermal diffusivity	α	$73\times 10^{-6} \text{ m}^2\cdot\text{s}^{-1}$
4	Specific heat	c_p	$875 \text{ J}\cdot\text{kg}^{-1}\cdot\text{K}^{-1}$
5	Young's Modulus	E	$7.31\times 10^{10} \text{ Pa}$

Table 4.02: The calculated Modal resonance frequencies of the cantilever

Mode No	Calculated resonance frequency f_0 , Hz
M1	23.52
M2	147.39
M3	412.70
M4	808.72
M5	1336.87

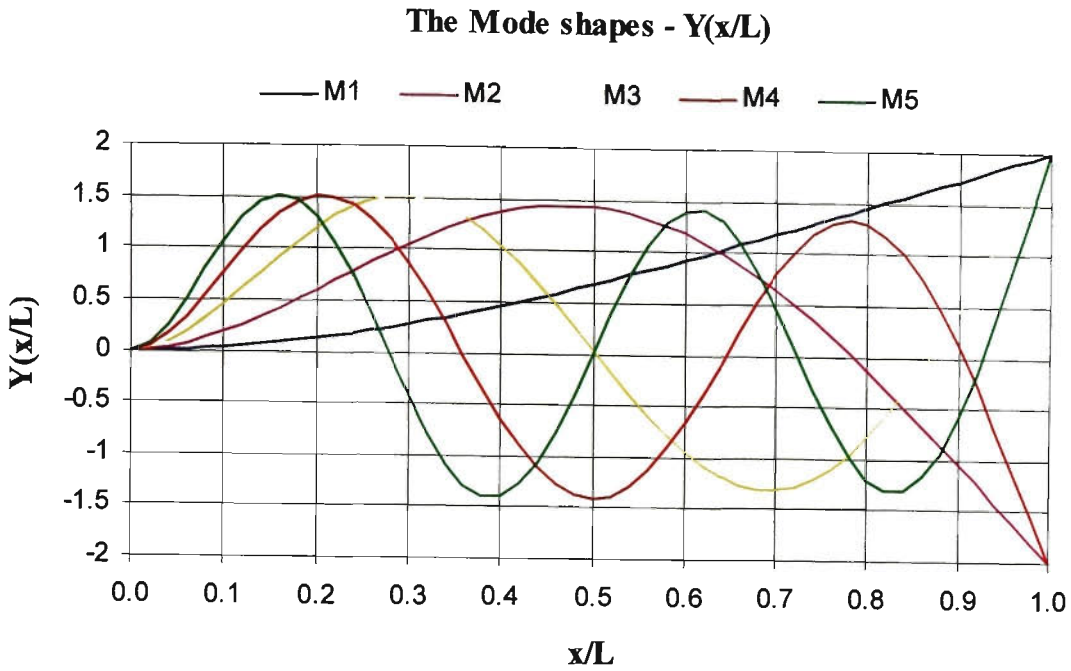


Figure 4.02 (a): The displacement profile $Y(x/L)$ (Modes 1-5) for clamped-free cantilever

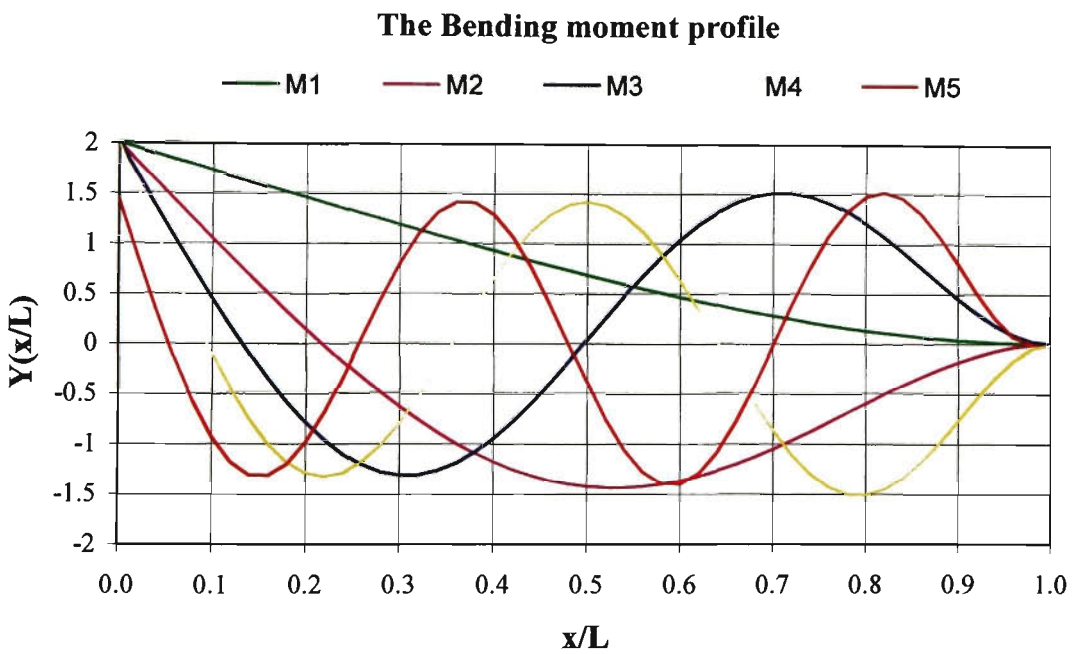


Figure 4.02 (b): The bending moment profile $Y''(x/L)$ for a clamped-free cantilever (Modes 1-5)

It was found by Philp (1993) that the bending moment induced by optical excitation of a clamped-free cantilever is directly proportional to the second derivative, d^2y/dx^2 , of the displacement profile. Thus the maximum bending moment for a specific mode of vibration is achieved when the laser beam is directed exactly at the antinodes of the second derivative of the displacement amplitude (Eq. 2.24). The displacement mode shapes (or the displacement profiles) and the corresponding bending moment profiles for the first five modes are shown in Figures 4.02 (a) and 4.02 (b).

The node and antinode positions of the displacement profile and of the bending moment profile were calculated using the mode shape (Eq. 2.31) for the particular vibration modes given in Table 4.03.

Table 4.03: The bending moment profile and the displacement profile antinode locations of the cantilever for five vibration modes

Mode Number	Antinode locations of the bending moment (displacement) profile			
	1	2	3	4
M1	-	-	-	-
M2	0.52L (0.48L)	-	-	-
M3	0.30L (0.30L)	0.70L (0.70L)	-	-
M4	0.22L (0.20L)	0.50L (0.50L)	0.80L (0.78L)	-
M5	0.18L (0.16L)	0.38L (0.38L)	0.62L (0.62L)	0.84L (0.82L)

4.3 Response measurements with a rigid cantilever securely fastened to the mounting bench

With the cantilever beam rigidly fastened in the steel jaws of the mounting vice and the vice rigidly mounted to the bench on which the equipment stands, the structure has very high- Q , low-loss η resonances and the HPBW of the resonance peaks is very small. This allows detection of small changes in the natural resonance frequency. Experimental studies to date (Philp and Booth, 1994) used a square wave LD modulation waveform with 50% duty cycle. Some initial experiments using the HP33120A function generator and the laser diode were conducted to work out the most efficient modulation waveform (sine, square or triangular) and duty cycle (e.g. 25%, 33%, 40% and 50%) for excitation of vibration. It was found that for a fixed modulation amplitude, a sinusoidal waveform gave the largest amplitude excitation. The background "noise" was also smaller with sinusoidal excitation, presumably because there was less excitation of higher harmonics and hence there was less "interference" due to other vibrations. Despite the use of a vibration isolation table and a protective box to reduce the effects of air currents, the interferometer is sensitive enough to still pick up low frequency environmental noise which is always present in daytime. This noise arises from building vibrations (due to on road traffic and functioning of service equipment such as lifts, air conditioning structures etc), residual air current effects and acoustic vibrations. In general this environmental noise is at low frequencies. However, it is common to see transient peaks in the spectrum at frequencies in the region of the fundamental resonant frequency of the cantilever (22.5 Hz). For example transient peaks commonly occurred at frequencies in the region of 8 Hz, 9 Hz, 12 Hz and 18 Hz. The random variations in amplitude of this environmental noise affects the

stability of the magnitude of the modal peak in interferometer output signal, especially for low frequency modes of cantilever vibration. For this reason the first series of measurements was carried out during a very quiet time at night and averaging was used.

The following sections report measurements of the natural resonant frequency and the half-power bandwidth of the resonance for the first five vibrational modes. These measurements were carried out under three different environmental conditions which are typical of a laboratory environment. These conditions were meant to be typical of what may be called "favourable", "intermediate" and "noisy" laboratory conditions. The first (conditions A) involved measurements made late at night with vibration isolation for the laboratory bench, air current isolation with a box to cover the cantilever and with the air conditioning system turned off to reduce air currents and mechanical vibration. The second set of measurements (conditions B) was made during daytime with vibration isolation (but not air current) and the air conditioning system running. The final series of measurements (conditions C) were made during daytime with air conditioning running and with no vibration or air current isolation.

4.3.1 Response measurements under favourable laboratory conditions

The measurement conditions were:

- The experimental set-up was mounted on a vibration isolation bench. The bench was of heavy concrete construction and was isolated by placing the inflated tyres under the bench legs.

- The air-conditioning plant (with fan) was turned off. This is the most significant building plant noise source.
- The experimental set-up, including the laser diode, coupler, cantilever and the interferometer with output coupler, was enclosed in an airflow protection box.
- The traffic on road was rare and there were a very few units of building service equipment operating at this time.

4.3.1.1 Resonance measurements for Mode 1

The central resonance frequency for mode 1 was about 22.5 Hz and the width was of the order of 0.1 Hz. Thus to obtain resonance curves, it was only necessary to step the frequency over a range of about 0.5 Hz to 1 Hz. Generally a range of 1 Hz was used although sometimes larger ranges were used to record background noise levels as well as the resonance data. For nighttime measurements, the interferometer output signal at frequencies well away from resonance ("noise") is very small, being around 30 - 40 mV compared to a peak signal of several volts. When stepping the LD modulation through the resonance, the increment used between two adjacent frequencies was variable, depending on the change of signal amplitude displayed on the FFT output. Frequency steps were chosen manually so that there was a small but significant change in output signal level after each step. In regions of high slope, the modulation frequency step was generally 0.01 Hz. A typical record of a resonance profile included three sequential scans through the resonance; an initial scan in one direction, followed immediately by one in the reverse direction and then a further scan in the initial direction. The second and

third scans were carried out using the same frequency settings as the initial one. This overall scan process could take up to 2 hours due to the large number of frequencies, the averaging and the data storage of all the individual traces. Clearly, over this long time interval there were issues of changes in environmental parameters such as temperature. This was the reason for the three scans. During the quiet night time measurements, the fluctuations between successive readings at a particular frequency could be up to about 50 mV at points near resonance. Even though the signals are very much larger than this, such fluctuations do determine the accuracy with which the central frequency can be determined. Averaging reduces these fluctuations to around 20 mV. The FFT frequency resolution was set at 0.012 Hz for low frequency vibration modes (1-3) and at 0.032 Hz for high frequency vibration modes (4-5). Data recorded in the personal computer was initially processed using spreadsheet software (Excel) so that plots of power rather than amplitude were obtained (this involved squaring the data and multiplying by ω_r). These resonance (power) profiles were exported into a commercial curve fitting program (TableCurve 2D) and a Lorentzian curve was fitted to the data to give both central frequency and half-power bandwidth together with their standard errors. Fig. 4.03 gives an example of the resonance (power) data for mode 1. This data is simply plotted using Excel to join successive points and a Lorentzian curve has not been fitted to the data. The labels on the data curves (eg. NDB25) are simply the scan data file names and the reason for the difference in the second scan label is that it was recorded in two separate data files. Clearly the data from successive scans are very similar and environmental drift effects are small during these quiet nighttime conditions. In order to demonstrate this point, the values of

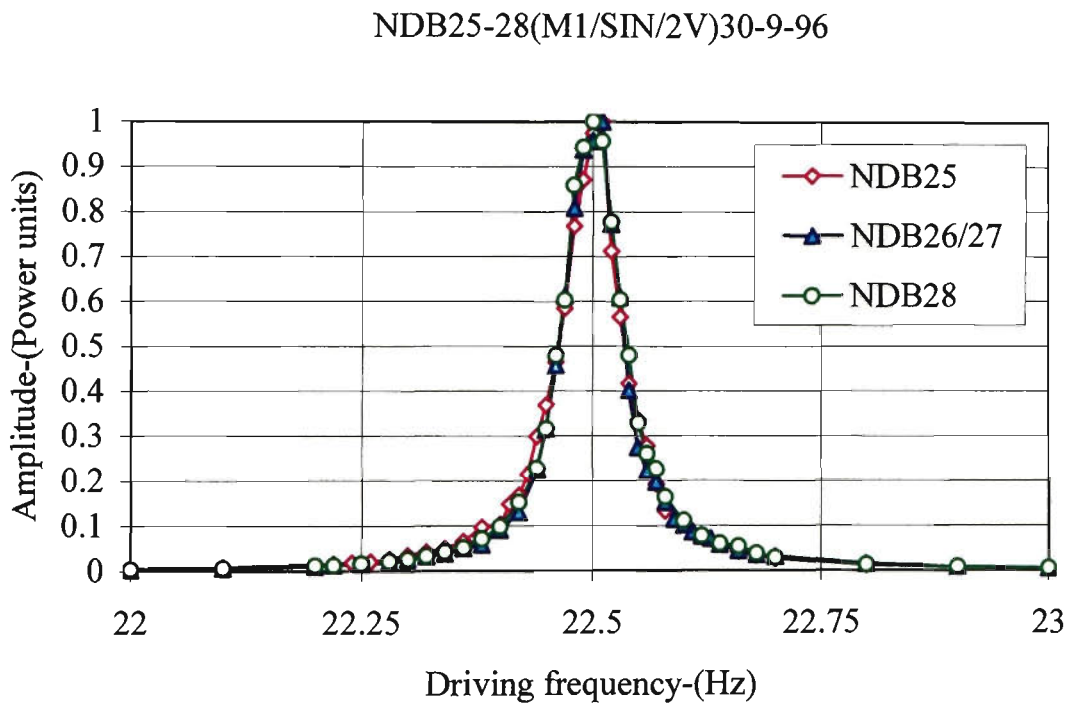
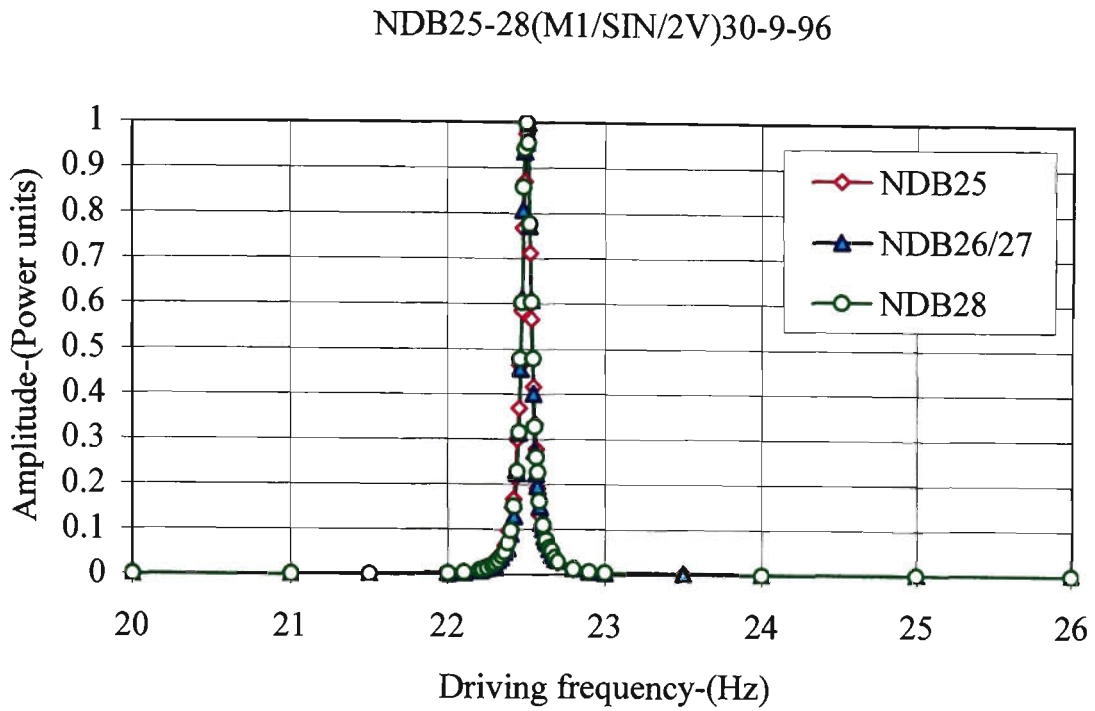


Figure 4.03: The resonance response curves for Mode 1 (the lower graph is an expanded version of the central region of the upper one). This data is plotted using MS Excel to join successive points

resonance frequency, half power bandwidth and Q obtained from these individual scans are tabulated in Table 4.04. Even though no curves have been fitted to the data, the central frequency is constant to within one scan step frequency interval (0.01 Hz).

Table 4.04: The displacement response curve parameters for Mode 1 under favourable laboratory conditions (3 data files of Fig. 4.03)

Series No	File name	Resonance frequency f_0 , Hz	Half-power bandwidth γ , Hz	Quality factor, Q	Ampl., V
Model					
1	NDB 25	22.51	0.071	317.0	2.85
2	NDB 26/27	22.50	0.064	351.6	2.70
3	NDB 28	22.50	0.076	296.1	2.64

Figure 4.04 shows the data points from the first scan of Fig. 4.03 together with the Lorentzian fit obtained using TableCurve. For this figure only one scan has been included as separate curves are needed for each scan and the curves are too similar to be resolved when more than one is plotted on a single figure. Figures 4.05 and 4.06 show similar fits to the data of the second and third scans of Fig. 4.03. The advantage of using TableCurve fits is that one can get best-fit precise numerical values of modal resonance frequency and half-power bandwidth. The parameters c and d in title lines of Fig. 4.04 - Fig. 4.06 represent the numerical values of resonant frequency and the half-width-at-half-maximum of the power resonance curve for the fundamental vibration mode. The vibration parameters obtained from the Lorentzian curve fitting are summarised in Table 4.05. It can be seen from the table that the numerical values of resonance frequency and half power bandwidth between three scans are in very good agreement. The standard error values for resonance frequency and for half power bandwidth are within a few ten thousandths and within one thousandth of a Hertz respectively. The uncertainties

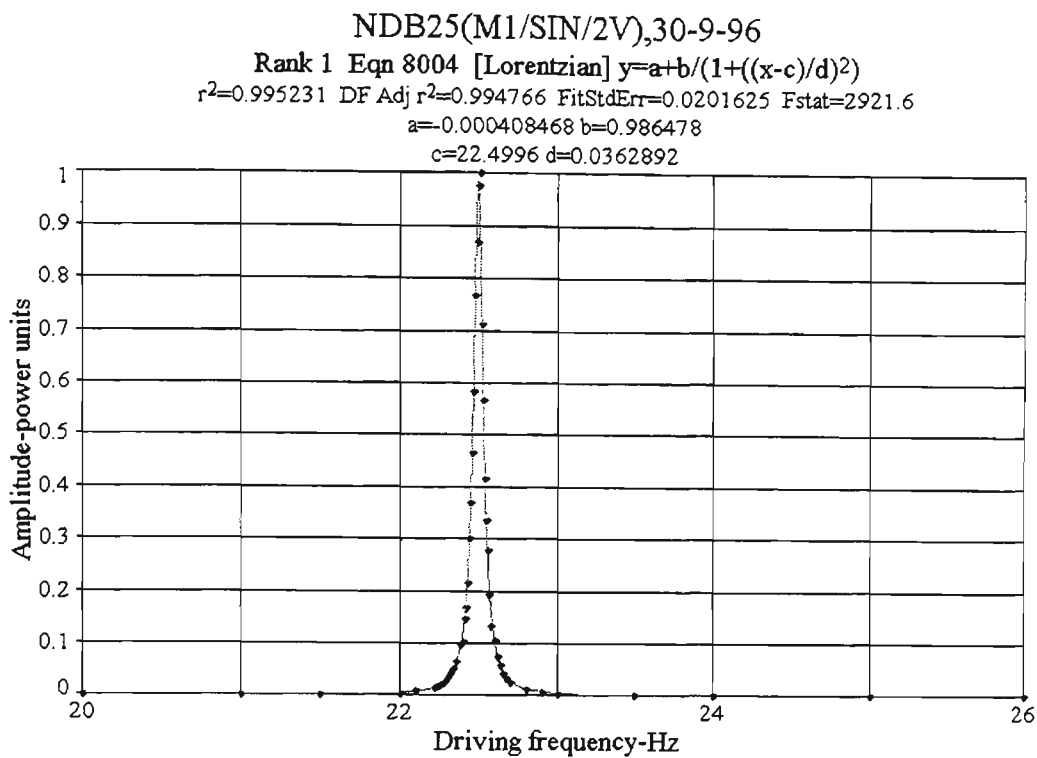


Figure 4.04: Lorentzian curve fit to the power resonance data points for the first scan of Mode 1 (NDB 25)

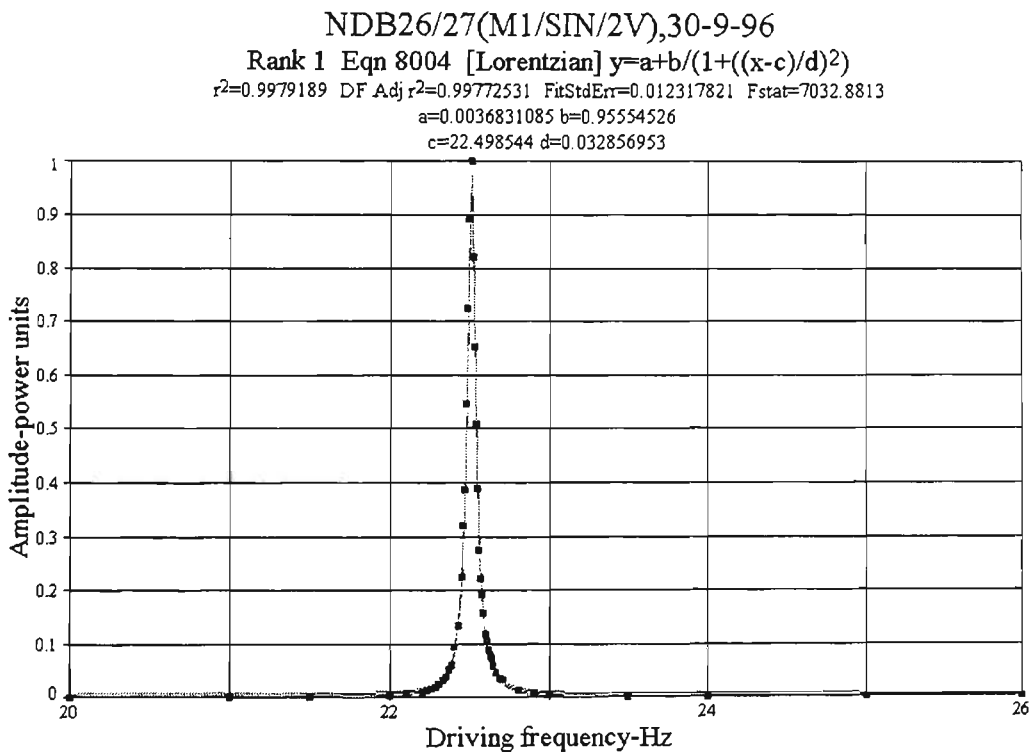


Figure 4.05: Lorentzian curve fit to the power resonance data points for the second scan of Mode 1 (NDB 26/27)

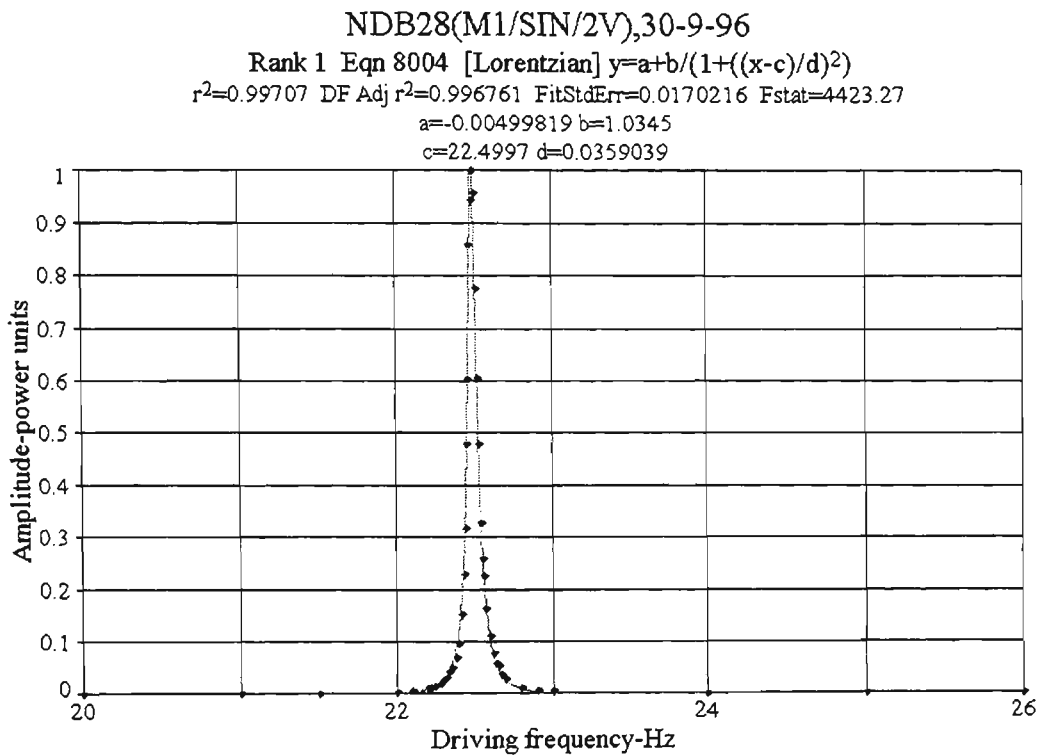


Figure 4.06: Lorentzian curve fit to the power resonance data points for the third scan of Mode 1 (NDB 28)

Table 4.05: The vibration parameters: resonant frequency, half power bandwidth and Q -factor from Lorentzian fits to the experimental response data for Mode 1

No.	File name	Frequency f_0 , Hz	Std error δf , Hz	Curve width γ , Hz	Std error $\delta \gamma$, Hz	Damping factor, ζ	Error, $\delta \zeta$
1.	NDB 25	22.4992	0.0003	0.0744	0.0011	0.00165	0.00002
2.	NDB 26/27	22.4985	0.0003	0.0657	0.0009	0.00146	0.00002
3.	NDB 28	22.4993	0.0004	0.0727	0.0014	0.00162	0.00003

of these measurements are small enough to calculate values of damping factor ζ (using Eq. 2.77) to an accuracy of about 1%. These calculated values of damping factor are also given in Table 4.05. A second order vibrating system with small amplitude of vibration and light damping ($\zeta < 0.1$) should behave linearly and have a damping factor which does not depend on vibration amplitude (Ch. 2). These conditions are certainly satisfied in the present experiments as the amplitude of vibration with laser diode excitation is very small and the measured ζ values of the

cantilever are about two orders of magnitude less than 0.1. Thus the three values of ζ in Table 4.05 should agree within experimental error. This is clearly not the case since the values differ by about ten times the standard error. A similar problem occurs with the resonant frequency and half-power bandwidth (which depend on ζ). The origin of this problem lies in temperature variations during the measurements. It takes about 40 - 45 minutes to measure and to record a displacement response curve. During this time some of the environmental parameters, such as room temperature in the laboratory, can vary. In fact the room temperatures was monitored during the above measurement series (~2 hours) and a variation of 0.4-0.5 °C was observed. If we substitute the values of resonant frequency $f_1(E)=22.5$ Hz of Mode 1 and temperature change $\Delta T = 0.4^\circ\text{C}$ into Eq. 2.43 we obtain a value for frequency shift produced by the temperature dependence of Young's modulus as

$$\Delta f_1(E) = -\frac{1}{2} \cdot \frac{4.8 \cdot 10^{-4}}{\sqrt{1 - 4.8 \cdot 10^{-4} \cdot 0.4}} \cdot 22.5 \cdot 0.4 = 0.0022 \text{ Hz} .$$

The observed resonant frequency variation of about 0.0008 Hz would be explained by a temperature change of the cantilever of slightly over 0.1 °C. Thus the variations in measured resonant frequency in Table 4.05 are considered to be real and produced by ambient temperature variations during the measurement period. If the temperature of the cantilever can be maintained constant, then the technique of scanning the modulation frequency through the resonance and fitting a Lorentzian curve can produce resonance frequencies to at least within the standard errors given in Table 4.05 (if the temperature did not vary then the standard errors may have been even less). Hence the fractional error of the frequency measurement of the fundamental mode is potentially at least 2×10^{-5} . This fractional error is dependent

on the frequency resolution of the FFT of the DSA. For the measurements of the fundamental mode, the FFT resolution was 0.012 Hz. If the temperature was controlled so that constant temperature of the vibrating structure was assured, then the fractional error may be further reduced but this would probably require the frequency resolution of the FFT to be decreased to a figure below 0.012 Hz. It is also worth noting that the changes observed in resonant frequency are significantly greater than those produced by the stability of the LD modulation oscillator (better than 2 ppm / °C).

4.3.1.2 Resonance measurements for Modes 2-5

Measurements for the higher modes were carried out in a similar manner to those for mode 1. However, the magnitude of the thermally induced bending moment and hence the amplitude of the LD-induced vibration decreases as the modulation frequency is increased (Philp, 1993; Philp and Booth, 1994). Hence the vibration amplitudes for mode 5 were something like 30 times less than those of mode 2 and so the set-up was carefully adjusted to try to ensure that the best possible signal-to-noise ratios were achieved. For maximum vibration amplitude it was necessary to carefully focus the LD onto the surface of the cantilever and to ensure that the excitation was applied at an antinode of the vibration profile for each particular mode. Thus the LD was re-positioned for each modal resonance measured. The calculated positions of the antinodes (distance from the clamp) used for excitation were 0.52 L, 0.70 L, 0.50 L and 0.38 L for modes 2 to 5 respectively (L = 300 mm; see Table 4.03). The actual positions for maximum displacement amplitude were found to be within 2 mm of these calculated positions. In addition to these adjustments, the LD power was increased for modes 2 - 5 compared to that used for

mode 1 by doubling the modulation voltage applied to the laser drive circuit. This increased the peak-to-peak power from about 13 mW to 25 mW. Two additional adjustments had to be made before running higher mode measurements. As the locations of the vibration antinodes along the length of the cantilever vary for each mode, the laser diode had to be adjusted so that the radiation was incident at a convenient antinode of the bending moment profile. In addition, refocussing on the cantilever surface was required to optimise the vibration amplitude.

The normalised resonance response curves (converted to power units) for Modes 2-5 are shown in Figures 4.07-4.10.

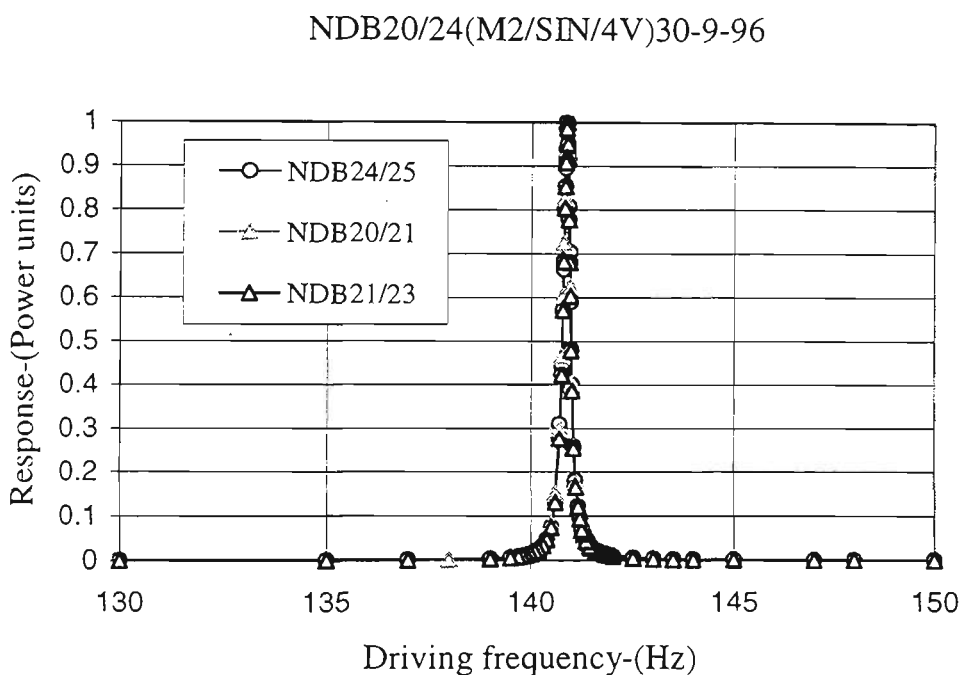


Figure 4.07: The response curves for Mode 2. The figure includes data for three separate scans through the resonance

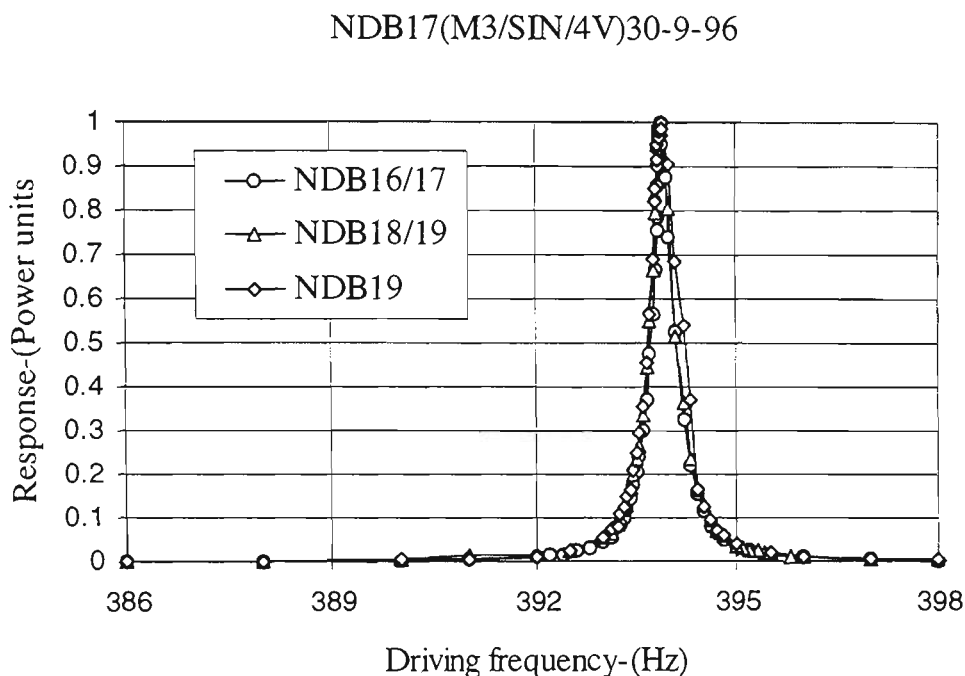


Figure 4.08: The response curves for Mode 3. The figure includes data for three separate scans through the resonance

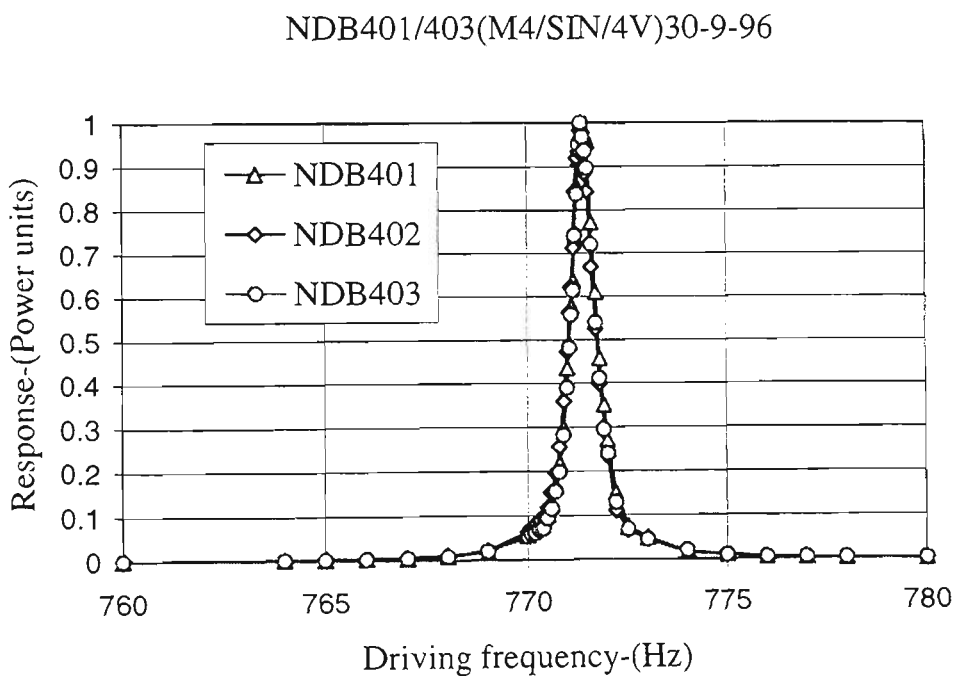


Figure 4.09: The response curves for Mode 4. The figure includes data for three separate scans through the resonance

NDB501/503(M5/SIN/4V)28-9-96

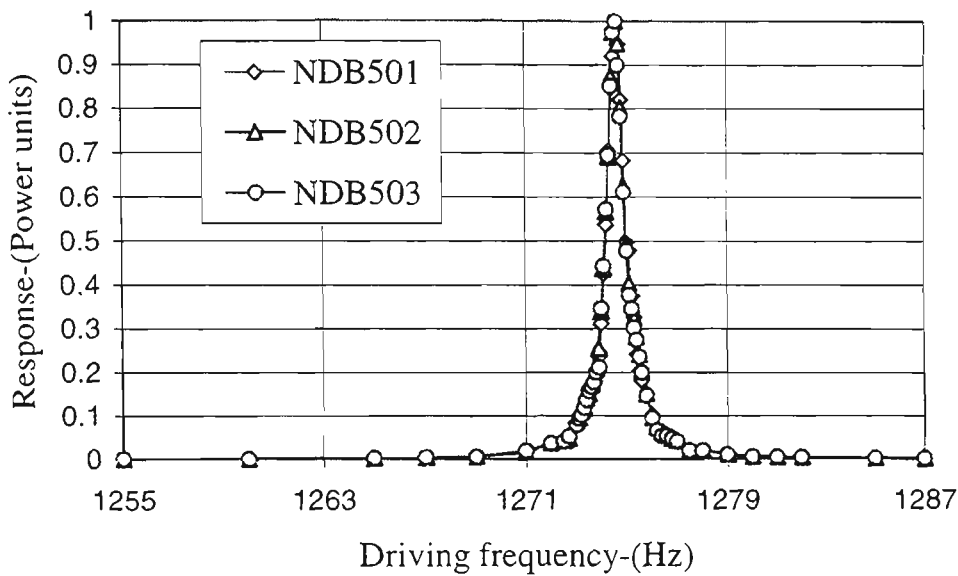


Figure 4.10: The response curves for Mode 5. The figure includes data for three separate scans through the resonance

As before, the conversion to power units has been done by squaring the amplitude data and multiplying by the driving frequency ω_f (see Eq. 2.71). Approximate values for the resonant frequency, half-power bandwidth (FWHM) and Q for Modes 2-5 have been determined by inspection of the data plotted in Figures 4.07 - 4.10 and these values are summarised in Table 4.06. Table 4.06 also includes the amplitude of the measured peak vibration for each mode. This highlights the general decrease in excitation efficiency as the modulation frequency is increased. These values are dependent on the care which is used in optimising the setup for each mode. Much greater care was taken with optimising mode 5 (compared to the other modes) as the amplitude of the resonance vibration was relatively low.

Table 4.06: Approximate vibration parameters obtained from inspection of the displacement response curves for Modes 2-5 (Figures 4.07 - 4.10)

Scan No	File name	Resonance frequency f_0 , Hz	Curve width γ , Hz	Quality factor, Q	Peak Amplitude, V
Mode2					
1	NDB 21	140.88	0.21	660.2	2.88
2	NDB 22	140.87	0.21	663.2	2.90
3	NDB 24	140.88	0.21	663.0	2.92
Mode3					
1	NDB 16	393.88	0.40	983.2	0.67
2	NDB 17	393.88	0.43	913.0	0.63
3	NDB 19	393.88	0.49	810.6	0.58
Mode4					
1	NDB 401	771.35	0.71	1079.3	0.058
2	NDB 402	771.35	0.70	1096.6	0.065
3	NDB 403	771.35	0.67	1152.1	0.059
Mode5					
1	NDB 501	1274.6	0.82	1546.8	0.073
2	NDB 502	1274.6	0.84	1512.5	0.075
3	NDB 503	1274.6	0.84	1526.1	0.076

It is clear from Table 4.06 that as the modal resonance frequency increases, so does the half-power bandwidth. However, the Q is increasing with resonant frequency and this is consistent with a decrease in the damping factor, ζ , with frequency. If frequency shifts produced by external influences are proportional to the resonant frequency, then one might expect that, given a proper choice of spectral resolution, the increase in Q with modal frequency would imply that small influences would be more easily detectable using higher order modes. However, one also has to consider the decrease in excitation efficiency for higher order modes. The accuracy with which the various vibration parameters can be determined for the higher order modes is investigated further in the next section using Lorentzian fits to the resonance data.

4.3.1.3 Vibration parameters obtained using Lorentzian fits for modes 1-5

Table 4.07 summarises the results of Lorentzian fits to the data of the scans for all of the modes (1 - 5). As was the case with the mode 1 results discussed earlier, the variation between scans is considerably greater than the standard error of the fit for a particular scan. For example, the spread of resonant frequencies for modes 2 - 5 is about 5 to 20 times greater than the standard errors. The fractional errors in the determination of resonant frequency for a single scan for modes 2 - 5 are all around $(2 - 4) \times 10^{-6}$ which is somewhat better than the value of about 2×10^{-5} which was obtained for mode 1. These figures are an order of magnitude less than the

Table 4.07: Vibration parameters obtained from a Lorentzian fit to the scan data of Modes 1-5 under favourable laboratory conditions - Conditions "A"

No.	File name	Frequency f_0 , Hz	Std error δf_0 , Hz	Width γ , Hz	Std error $\delta \gamma$, Hz	Damping factor ζ	Std. error $\delta \zeta$	Ampl., V
Mode 1								
1	NDB 25	22.4992	0.0003	0.0744	0.0011	0.00165	0.00002	2.85
2	NDB 26	22.4985	0.0003	0.0657	0.0009	0.00146	0.00002	2.70
3	NDB 28	22.4993	0.0004	0.0727	0.0014	0.00162	0.00003	2.64
Mode 2								
1	NDB 21	140.8675	0.0003	0.2160	0.0012	0.00077	0.000004	2.88
2	NDB 22	140.8703	0.0005	0.2128	0.0017	0.00076	0.000006	2.90
3	NDB 24	140.8713	0.0004	0.2154	0.0015	0.00076	0.000005	2.92
Mode 3								
1	NDB 16	393.9132	0.0015	0.4066	0.0050	0.00052	0.000006	0.67
2	NDB 17	393.8953	0.0013	0.4314	0.0041	0.00055	0.000005	0.63
3	NDB 19	393.9127	0.0012	0.4711	0.0040	0.00060	0.000005	0.58
Mode 4								
1	NDB 401	771.4113	0.0025	0.6965	0.0087	0.00045	0.000006	0.058
2	NDB 402	771.3597	0.0025	0.6976	0.0091	0.00045	0.000006	0.065
3	NDB 403	771.3949	0.0027	0.6501	0.0095	0.00042	0.000006	0.059
Mode 5								
1	NDB 501	1274.6054	0.0044	0.8810	0.0154	0.00035	0.000006	0.073
2	NDB 502	1274.5864	0.0048	0.8691	0.0169	0.00034	0.000007	0.075
3	NDB 503	1274.5794	0.0053	0.8546	0.0186	0.00034	0.000007	0.076

fractional errors determined from the variations between scans, which are all between 1×10^{-5} and 4×10^{-5} . Similar conclusions apply to the other parameters included in the table. The results for mode 2 are consistently slightly better, than those of the other modes, but with only three scans per mode the statistics are not good enough to support a conclusion that such a difference is significant. Given the spread of parameters obtained between scans, there was little point in including data from a greater number of scans when the temperature of the cantilever was not controlled. The origin of this variation between scans is again considered to be temperature fluctuations of the cantilever during the measurements. As explained earlier, variations in cantilever temperature affect the stiffness of the cantilever and hence the Young's modulus and modal resonant frequency. Table 4.08 summarises the frequency shifts of the various modes due to a temperature variation of between $0.1 \text{ }^\circ\text{C}$ and $1 \text{ }^\circ\text{C}$. The variations in modal resonant frequency of all the scans included in Table 4.07 can be explained by a total temperature variation of less than $0.5 \text{ }^\circ\text{C}$. This is less than the maximum measured room temperature fluctuation during a series of scans of $0.6 \text{ }^\circ\text{C}$. Thus the fluctuations of the measured parameters between scans are considered to be consistent with cantilever temperature variations and in an uncontrolled environment this certainly represents a limitation to the possible measurement accuracy. In a temperature-controlled environment (ΔT at best about $\pm 0.01 \text{ }^\circ\text{C}$), the resonant frequency can be measured to about three parts per million. This figure is limited by the temperature fluctuations during the time of a single scan. This uncertainty in measured modal resonant frequency determined from fitting Lorentzian curves to the scans is

between two and three orders of magnitude less than the half-power bandwidths of the resonances.

Table 4.08: Changes in modal resonant frequency due to temperature drift

No	Temperature drift, °C	Resonant frequency shift, Hz				
		$f_1=$ 22.4992	$f_2=$ 140.8703	$f_3=$ 393.9127	$f_4=$ 771.3949	$f_5=$ 1274.5864
1	0.1	0.0005	0.0034	0.0095	0.0186	0.0307
2	0.4	0.0024	0.0151	0.0420	0.0822	0.1358
3	1.0	0.0060	0.0378	0.1049	0.2055	0.3395

The data presented in this section has all been for a very lightly damped system so that half-power bandwidths were small and accurate measurements could be made of modal resonant frequency. Under these conditions, five modes were able to be optically excited with reasonable vibration amplitude and measured. In more heavily damped systems, the decrease in amplitude may be such that fewer modes can be useable using the scanning technique.

4.3.1.4 Decay time measurements by waveform sampling: Modes 1-3

In preceding section the damping factor ζ was deduced using the values of resonance frequency and half-power bandwidth, which were obtained from measurement of the response curve followed by a Lorentzian fitting procedure. Another common way to determine the structural damping is by measuring the time taken for the amplitude of the vibration to decay by a factor of e . As was shown in Chapter 2 (Sec. 2.5.1) free vibration after removal of excitation must continue until damping brings the system to the rest in a finite time. The first part of the transient term, $F_1 e^{-\zeta \omega t}$, in Eq. 2.49 represents a decaying amplitude for the harmonic function

$\text{Sin}(\omega_d t + \phi)$. By digitally recording the vibration amplitude waveform over a period long enough to see significant decay and then fitting this data with an equation of the form of Eq. 2.49, the two parameters ζ and ω_d can be determined. This fitting procedure will also give an estimate of the standard error of the parameters. This procedure was carried out and the results are described in this section. Values of parameters were obtained in two ways. Firstly, ζ was obtained by fitting the term $F_1 e^{-\zeta \omega_n t}$ to the envelope of the decay waveform. The second method used a fit of the damped sinusoid to the entire waveform to give both ω_d and ζ . For both methods it is important that a reasonable number of data points are recorded for each vibration cycle. It should be noted that this measurement technique produces ω_d rather than ω_n . For the very lightly damped structures currently under investigation this is not a significant problem as the two parameters differ by only about one part in 10^6 . This type of measurement was more sensitive to the signal-to-noise as no data averaging was possible. In general, the signal to noise affected the standard error of the fits but for signal-to-noise values below a certain limit, reasonable fits were simply not possible. For the lower frequency modes (1 and 2) where the signal-to-noise is relatively high, the technique worked well. Mode 3 measurements were made with some difficulty and only values of ζ were obtained. However, it was not possible to make measurements using modes 4 and 5.

The decay waveform of the particular mode of vibration was recorded after the response curve measurements have been completed and before the laser diode has been re-positioned and re-focused to excite the next mode. Measurements were

made by either turning on the laser diode using CW sinusoidal modulation and switching off the modulation after equilibrium had been reached or by using a "burst mode" feature to give a finite number of modulation cycles. Both methods were equivalent and produced similar results and the burst mode was the most convenient. In the burst mode of operation, the number of cycles of modulation was generally set to 500 and this was more than enough to set up steady state conditions for all modes. The number of data points recorded for the vibration waveform was 4096 for mode 1, 8,192 for mode 2 and mode 3. Recordings of the waveforms used approximately 4 point per vibration period for all three modes.

The vibration parameters and their standard errors were obtained from the data by fitting mathematical relationships using TableCurve 2D software. Damped sinusoid equations were fitted to the entire data sets to obtain values of ω_d and ζ for each vibration record. To obtain ζ , 25 - 30 representative peak data points were selected for the fitting of the exponentially-decreasing amplitude function to the envelope of the decay waveform. The TableCurve software provided a simple way of choosing suitable points from the graphical display of the vibration waveform records.

Figure 4.11 shows a typical decay envelope for mode 1 and superimposed is a decaying exponential with decay time derived from fitting the data. With the timescale used for the display, the sinusoidal nature of the waveform is not discernible. The fit of the exponential decay to the envelope is clearly not ideal and the reason for this is the noise superimposed on the signal waveform. Table 4.09 summarises the decay time data obtained from fits similar to Fig. 4.11 for the

modes 1 - 3. The table shows data for three separate waveform records per mode to give the standard error for each fit and also show the reproducibility of the data. As with the data for ζ contained in Tables 4.05 and 4.07, the measured values of decay time differ by about 2 - 6 times the standard error. While some of the spread may be due to the selection of the 25 - 30

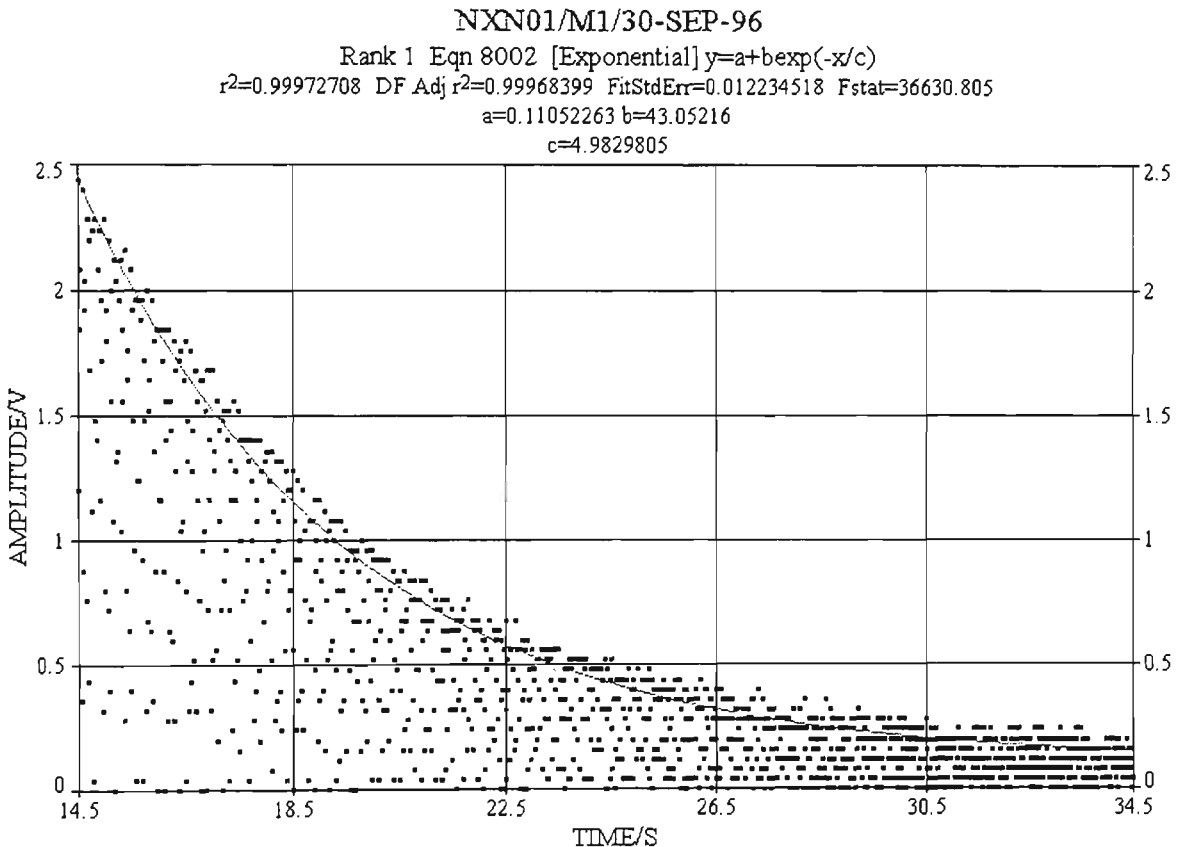


Figure: 4.11: Vibration amplitude decay waveform (displacement) for mode 1. The record is 4096 data points long and is recorded at about 4 points per period. The superimposed exponential has a decay time obtained by fitting a single exponential decay to 25 - 30 peak data points of the decay waveform

data points for the fit, the basic reason for the fluctuation in values from one record to another is again considered to be temperature variations of the cantilever between records.

Table 4.09: Decay time data obtained using an exponential function $\exp(-t/\tau_{exp})$ fit to the envelope of the recorded waveforms of Modes 1-3

Record No.	File name	Decay time τ_{exp} , s	Std. Error $\delta\tau_{exp}$, s
Mode 1			
1	NXN01	4.983	0.053
2	NXN02	5.752	0.063
3	NXN03	5.444	0.057
Mode 2			
1	NXN3	1.828	0.036
2	NXN4	2.057	0.054
3	NXN04	2.037	0.060
Mode 3			
1	NXN07	0.677	0.010
2	NXN08	0.746	0.020
3	NXN7	0.734	0.013

The second method of obtaining the vibration parameters, by fitting a damped sinusoid to the entire data set, provides values of ζ which have much smaller standard errors for single scans. A typical fit of this type for mode 1 is shown in Figures 4.12 and 4.13. These figures show the data on timescales which are appropriate to displaying the decay and also the harmonic vibration over a small number of periods. Figure 4.13 makes it clear that the fit obtained is excellent provided one fits with 5 variable parameters - offset, amplitude, decay constant, damped frequency and phase. As explained earlier, this type of fit was only possible for the first two modes as reasonable fits were not possible with higher order modes due to the reduced signal amplitude and relatively poor signal-to-noise ratio. The data obtained for the first two modes is summarised in Table 4.10.

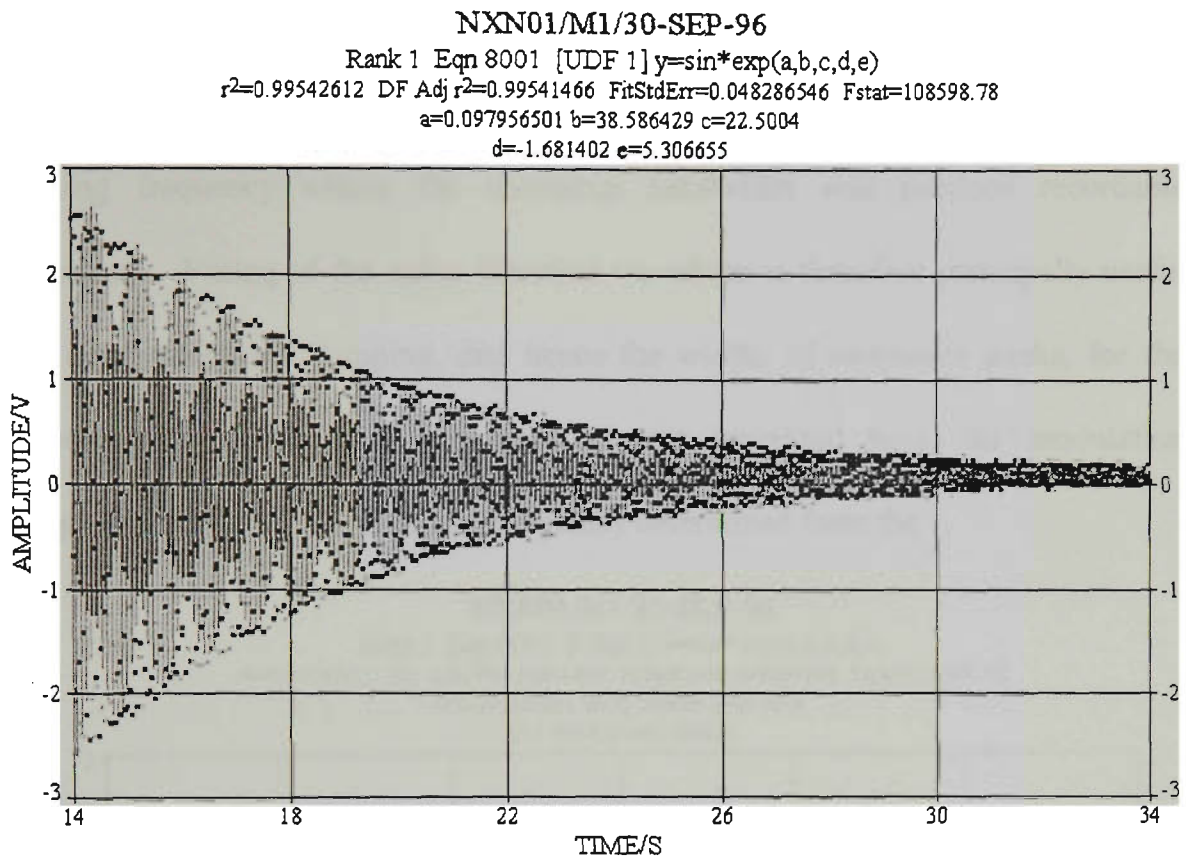


Figure 4.12: Vibration waveform (displacement) for mode 1 together with a fit to the data using an equation of the form $y = a + be^{-t/e} \sin(2\pi ct + d)$

While the values of decay time in Table 4.10 have smaller standard errors than was the case for the previous data of Table 4.09, the variation of values between records is of similar magnitude and the variations are again substantially greater than the standard errors. This is again consistent with a variation between records which is due to temperature variations. It is evident from Table 4.10 that the fitting of a damped sinusoid to the entire vibration waveform record is a more satisfactory way (compared to fitting only the envelope) of obtaining vibration parameters for modes where the signal-to-noise allows this approach. This method has the added advantage over the resonance scan method, described in section 4.3.1.1 and 4.3.1.2, that the measurement can be completed very quickly and requires only a time comparable with the decay time of the mode. However, one needs to first determine the resonant frequency reasonably accurately for this method as the

frequency of the decaying waveform is always that of the applied modulation. This method is not useful for very accurate determination of resonant frequency as any forcing frequency within the resonance bandwidth will produce recordable vibrations. Fitting of the entire vibration waveform is therefore principally useful for determining the damping, and hence the widths of resonance peaks, for the lowest order modes. For the measurements presented here, the modulation frequency was set to the resonant frequency determined from the

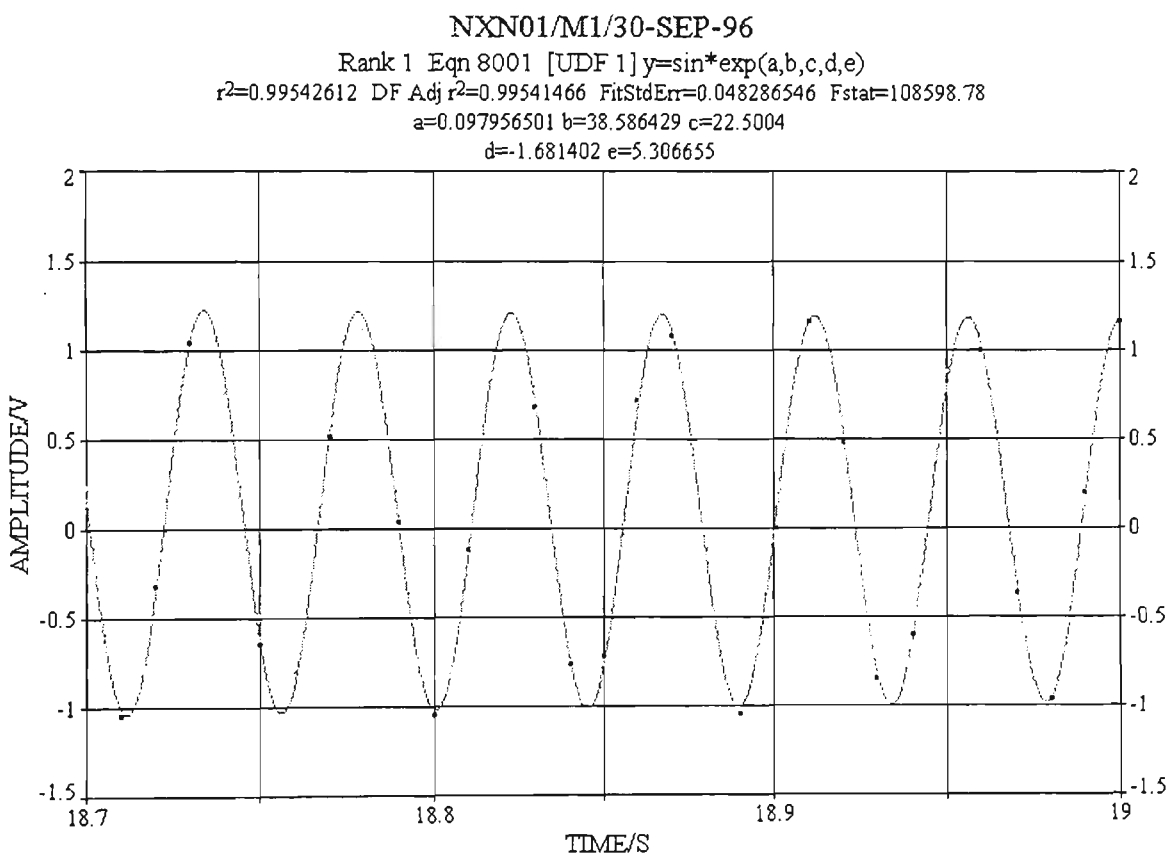


Figure 4.13: Vibration waveform (displacement) for mode 1 together with a fit to the data using an equation of the form $y = a + be^{-t/e} \sin(2\pi ct + d)$

Lorentzian fits to the scan data and the existence of maximum vibration amplitude was checked immediately prior to the measurement.

Table 4.10: Values of damped resonant vibration frequency and decay time for modes 1 and 2 obtained from fitting an equation of the form $y = a + be^{-t/\tau} \sin(2\pi ct + d)$ to the measured decay waveforms

No	File name	Decay time τ , s	Std.error $\delta\tau$, s	Resonance frequency f_d , Hz	Std.error δf_d , Hz
Mode1					
1	NXN 01	5.3067	0.0164	22.5004	0.0001
2	NXN 02	5.2415	0.0163	22.5000	0.0001
3	NXN 03	5.2127	0.0167	22.5007	0.0001
Mode2					
1	NXN 3	1.7786	0.0040	140.7785	0.0002
2	NXN 4	1.9674	0.0049	140.8556	0.0002

It is interesting to compare the data obtained from the Lorentzian fits to the scans (Table 4.07) with that obtained from the damped harmonic decays. To facilitate this comparison, Table 4.11 shows, in addition to the resonant frequency, values of damping factor and half-power bandwidth derived from the decay data of Table 4.10. In general the data of Tables 4.07 and 4.11 agree quite well. The slight difference in resonant frequency may be due to the fact that the scan data and the decay data were recorded at different times. The standard errors in frequency determined from a single record of the decay data are somewhat less than those obtained from a single scan. Both sets of data show variations of frequency between measurements, which are substantial, compared to the standard errors. The standard errors of the decay-derived values of ζ and γ for a single record are about 5 times smaller than those obtained from the scan data. While the actual values of these two parameters are about the same for the two methods, the values are consistently lower for the decay-derived data. The variation of these parameters between separate records is about 2% and 10% for modes 1 and 2 respectively for the decay-derived data and the corresponding figures for the scan-

derived data are about 11% and 2%. For the scan-derived values of ζ and γ , the variations arise from the fits which are probably affected by variations of frequency with temperature during the scan. For the decay-derived values of ζ and γ , the variations between records are directly attributable to variations in the fitted values of decay time. For both methods, it is clear that when the temperature is not controlled it is possible to make much more accurate measurements of resonant frequency than other vibration parameters associated with damping or energy loss. The fractional variations of the former are about three orders of magnitude smaller than those of the latter. Hence, for a sensitive measurement of changes (other than those due to temperature) in vibration parameters in high-Q structures where the temperature is not controlled, it is best to measure changes in resonant frequency. If the temperature is controlled and one wishes to make measurements of damping or energy loss related parameters for lower order modes, the lower standard errors obtained with the harmonic decay method would suggest that this may be the better method to use.

Table 4.11: Calculated values of damping factor and half-power bandwidth using the decay time measurements of Table 4.10

No	File name	Resonance frequency f_d , Hz	Std.error δf_d , Hz	Damping factor, ζ	Error, $\delta\zeta$	Half-power bandwidth γ , Hz	Error, $\delta\gamma$, Hz
Mode 1							
1	NXN 01	22.5004	0.0001	0.00133	0.000004	0.0600	0.0002
2	NXN 02	22.5000	0.0001	0.00135	0.000004	0.0607	0.0002
3	NXN 03	22.5007	0.0001	0.00136	0.000004	0.0611	0.0002
Mode 2							
1	NXN 3	140.7785	0.0002	0.00064	0.000001	0.1790	0.0004
2	NXN 4	140.8556	0.0002	0.00057	0.000001	0.1618	0.0004

4.3.1.5 Variations in resonant frequency due to temperature changes

In earlier sections, fluctuations in resonant frequencies have been observed which are greater in magnitude than the standard errors of the fits (either fits to the scans or fits to the decay data). These fluctuations have been ascribed to changes in the temperature of the cantilever, which affects its stiffness and therefore the modal resonant frequencies. It was not easy in an environment where the temperature could not be controlled to carry out a careful measurement of the variation of modal resonant frequency with temperature. However, it was considered necessary to check that the magnitude of the temperature-induced changes were roughly in agreement with those previously predicted from the thermal variation of Young's modulus. In order to do this the cantilever arrangement and a small hotplate were enclosed in a box and measurements were made over a period in excess of 1 hour as the hotplate raised the air temperature from about 20 °C to 30 °C. A thermocouple attached to a second cantilever was also included inside the box to provide approximate temperatures for the cantilever, which was vibrating. During this time, the temperature and resonant frequency were constantly changing and so measurements were made by fixing the driving frequency at the initial resonant frequency of the first mode (about 22.5 Hz) and monitoring the decrease in amplitude of the excitation as the resonant frequency was lowered due to the rise in temperature. The principle of this measurement is illustrated in Figure 4.14.

For a Lorentzian lineshape, the amplitude (power) of the resonant vibrations should decrease to about 20% of its peak value when the resonant frequency shifted by one half-power-bandwidth (about 0.06 Hz). A decrease in power amplitude to this level was obtained in about 3 °C and hence the thermal resonant frequency change

was about $0.02 \text{ Hz } ^\circ\text{C}^{-1}$. This figure is about a factor of three higher than the figure of $0.006 \text{ Hz } ^\circ\text{C}^{-1}$, which was obtained previously (see Table 4.08). The difference between these two numbers is not significant as both are only approximate. The important point is that quite small temperature fluctuations in the environment are sufficient to produce easily observed shifts in the frequencies of the resonant modes.

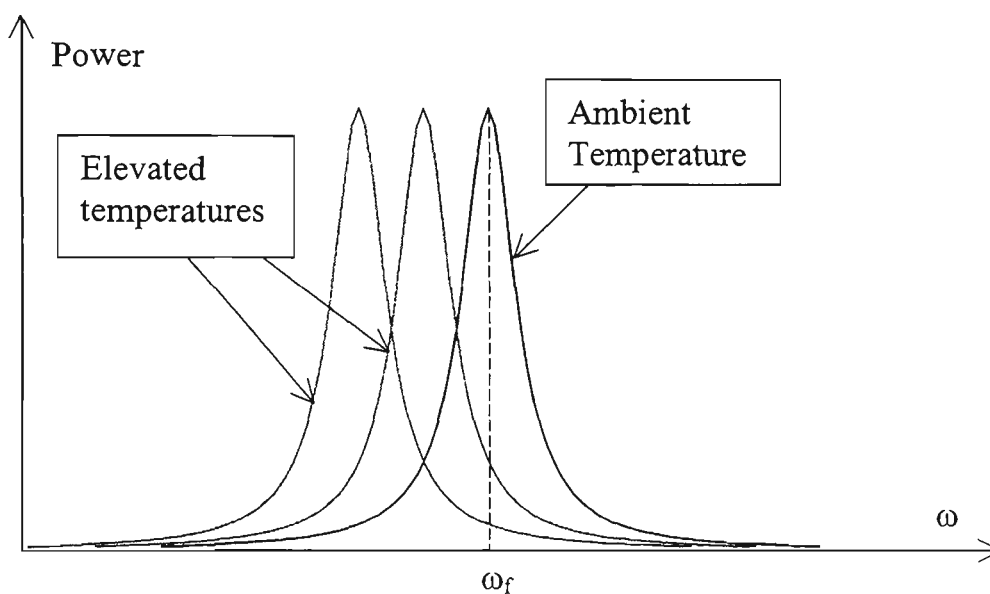


Figure 4.14: Illustration of the resonance frequency shift due to the temperature change. ω_f is the driving frequency of laser modulation

4.3.2 Day time measurements under less favourable laboratory conditions (Conditions B and C)

All measurements reported previously have been carried out under quiet nighttime conditions with vibration (air support) and air current (box) isolation. These were the best conditions available in the laboratory. The results presented in this section are for what have been called "intermediate" and (relatively) "noisy" laboratory conditions (conditions B and C). These conditions are typical of what can be achieved in a normal laboratory with little effort. For conditions B, the air conditioner was operating and the measurements were made during daytime hours.

The vibration isolation was maintained but the simple air current isolation was removed. Conditions C measurements were also made during daytime and for these measurements the air conditioner was operating and vibration and air current isolation were removed.

To demonstrate the effects of varying conditions on the recorded waveforms, Figure 4.15 shows a long-term record of the mode 1 vibration under steady modulated-laser excitation for the three different environmental noise conditions. Despite the visual aliasing effects evident under conditions A, the amplitude of the vibration can be seen to be quite constant over a 40-second period. Fitting of a sinusoidal vibration under these conditions gives excellent correlation coefficients and small standard errors. In contrast, under conditions C, the figure shows obvious random noise-induced vibrations superimposed on the 22.5 Hz oscillations which are thermoelastically excited. These obvious random effects have periods ranging from about 0.25 s to 2 s. There are also other higher frequency noise contributions which are not evident in a figure such as this. Fitting of a sinusoid to a waveform such as shown in Figure 4.15 (C) produces much lower correlation coefficients and larger standard errors in the fitted parameters.

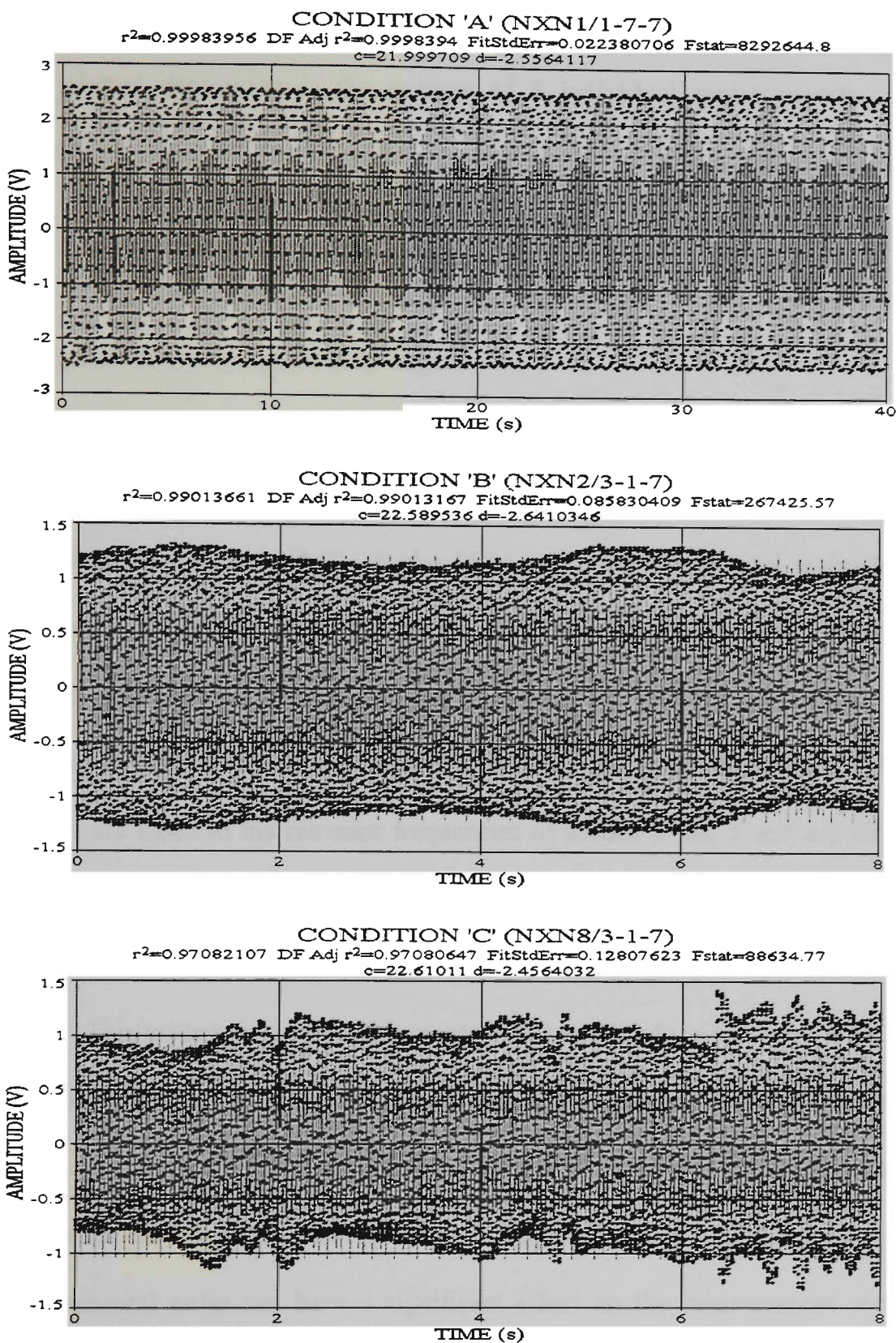


Figure 4.15: Vibration amplitude (displacement) waveforms during steady state excitation for mode 1 under conditions A, B and C. The narrow spikes evident outside the vibration envelope in, for example, the waveform for conditions C, show the fitted sinusoid

Figure 4.16 shows scan data recorded under conditions A, B and C. For these data, each plotted data point is the average of 5 individual measurements at that particular frequency. The degradation in the quality of the resonance curves with additional noise is very obvious. The fitting of Lorentzian profiles to scans such as those in Figures 4.16 (B) and 4.16 (C) is still possible but the standard errors of the fitted parameters are significantly larger.

Figure 4.17 shows examples of the measured FFT noise spectra for the two extreme conditions (A and C). It should be noted that the vertical scales for the two spectra differ by a factor of about 4. For conditions A, there is a reasonably uniform noise floor together with a number of peaks in the spectrum. These peaks can vary in frequency from one record to another. The peaks at around 22 Hz and 141 Hz are close to the resonant frequencies of modes 1 and 2 and are likely to have been "amplified" by resonance in the structure. The main effect of the environmental noise under conditions C is to increase the vibrations below about 25 Hz. This leads to a significant increase in the amplitude of the vibrational noise at frequencies close to the mode 1 resonance. These noise-induced vibrations are not phase-related to the driving oscillation and so they give rise to the random modulation effects evident in Figure 4.15. Figures 4.15 to 4.17 demonstrate that environmental noise can have a significant effect on the measurement accuracy which is possible for modal resonant frequencies using the optical excitation and sensing technique. All the measurements reported in this thesis are for very small laser excitation powers. Under noisy conditions, the accuracy of measurements can

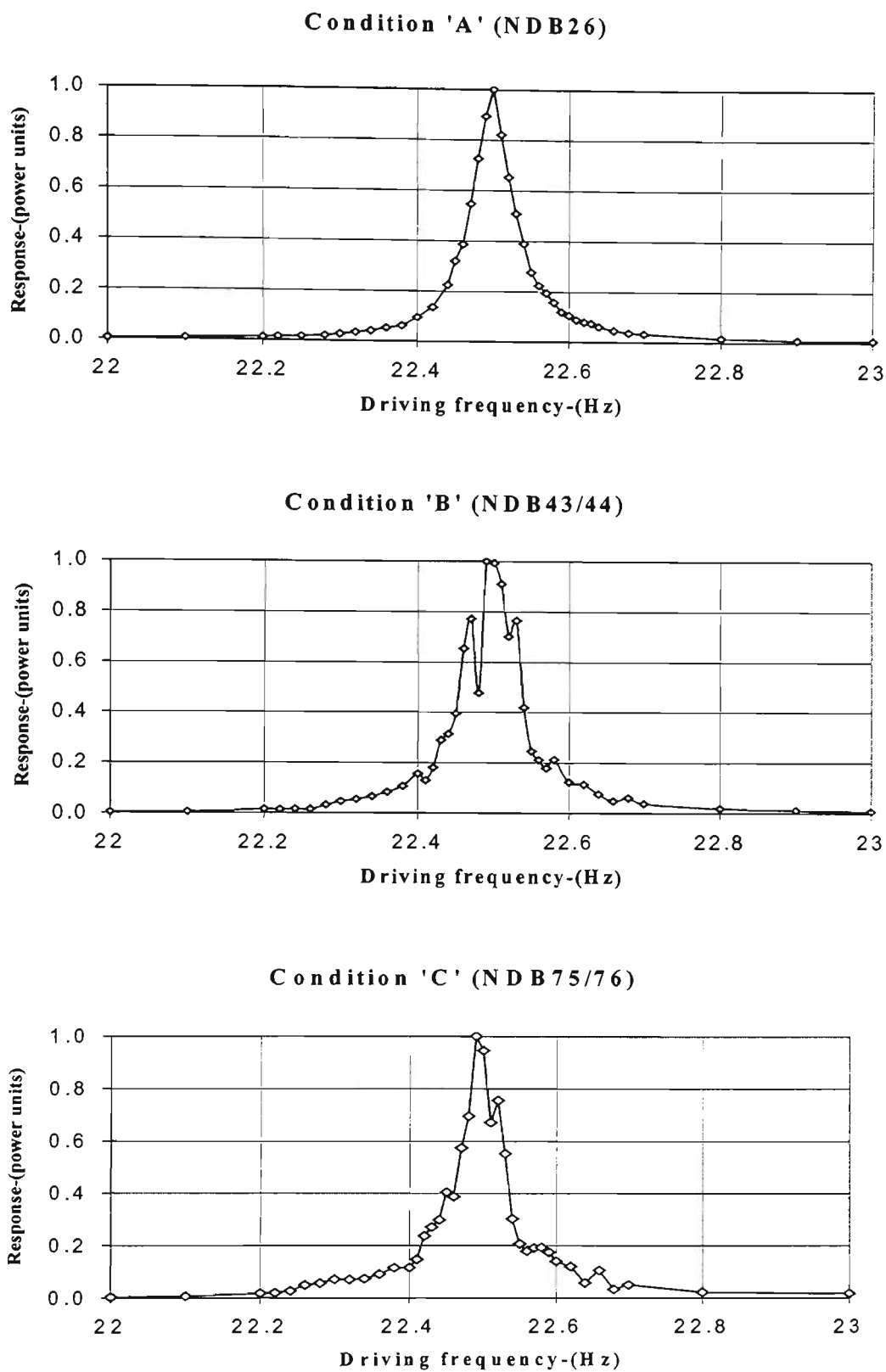
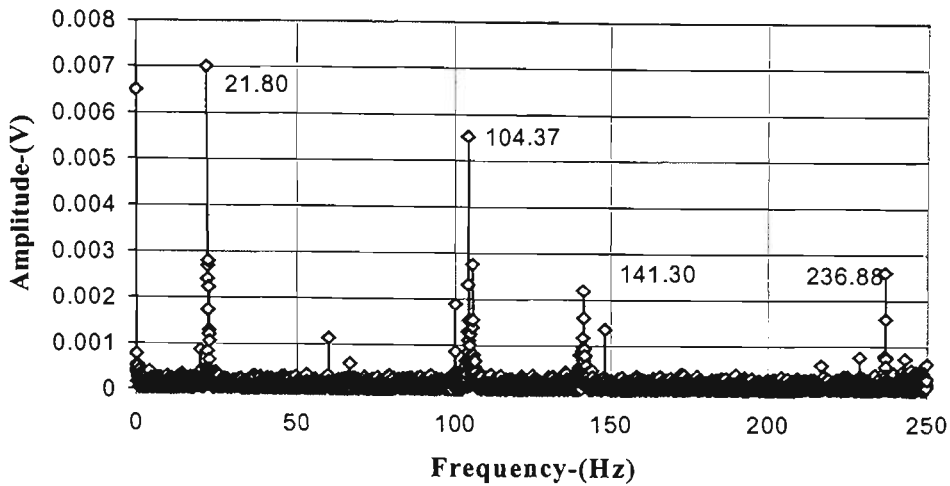


Figure 4.16: Scan data under conditions A, B and C. The data points are the average of 5 measurements at each frequency

Noise spectrum: quiet time (NXN13A/29-12-6)



Noise spectrum: daytime (NXN13/6-1-7)

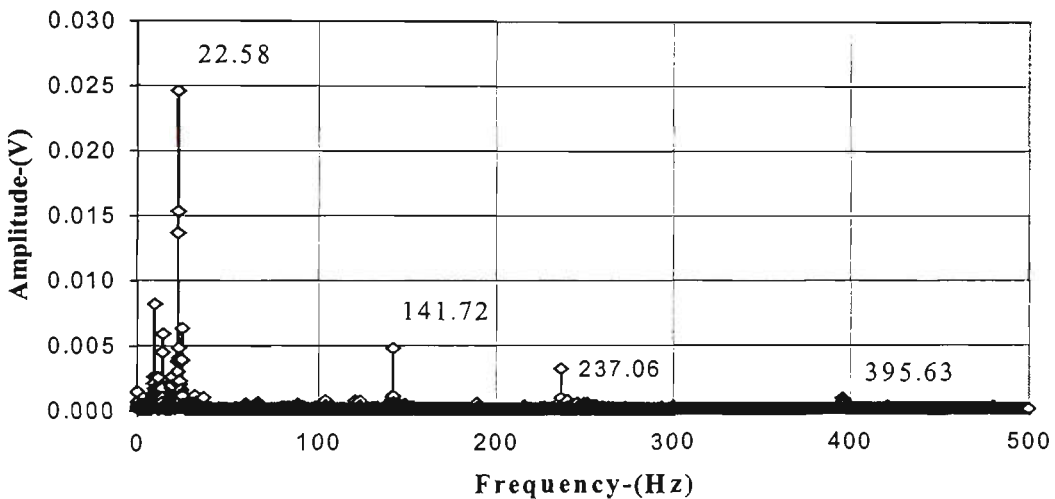


Figure 4.17: FFT noise spectrums for conditions A and C

be improved by increasing the power of the modulated laser source. Tables 4.12 and 4.13 summarise the results of Lorentzian fits to scan data for conditions B and C respectively. As with previous tables, for simplicity some of the data within the table is quoted to more decimal places than are significant. This data can be directly compared with similar data for conditions A, which was previously given in Table 4.07.

Table 4.12: Vibration parameters obtained from Lorentzian fits to the scan data of Modes 1-5 under conditions B

No.	File name	Frequency f_0 , Hz	Std error δf_0 , Hz	Width γ , Hz	Std. Error $\delta\gamma$, Hz	Damping factor, ζ	Error $\delta\zeta$
Mode 1							
1	NDB 43	22.4982	0.0016	0.0806	0.0057	0.00179	0.00013
2	NDB 45	22.4904	0.0007	0.0896	0.0026	0.00199	0.00006
3	NDB 48	22.4994	0.0004	0.0624	0.0014	0.00139	0.00003
Mode 2							
1	NDB 50	140.8839	0.0014	0.2091	0.005	0.00074	0.00002
2	NDB 52	140.9094	0.0013	0.2041	0.0048	0.00072	0.00002
3	NDB 54	140.8735	0.0007	0.2128	0.0028	0.00076	0.00001
Mode 3							
1	NDB 55	394.0245	0.0033	0.5343	0.0123	0.00068	0.00002
2	NDB 57	394.0250	0.0013	0.4720	0.0046	0.00060	0.00001
3	NDB 59	393.9887	0.0038	0.4986	0.0130	0.00063	0.00002
Mode 4							
1	NDB 401	771.7032	0.0061	0.7320	0.0218	0.00047	0.00001
2	NDB 402	771.5979	0.0118	0.6834	0.0440	0.00044	0.00003
3	NDB 403	771.6211	0.0039	0.8287	0.0144	0.00054	0.00001
Mode 5							
1	NDB 501	1272.881	0.0076	1.1934	0.0275	0.00047	0.00001
2	NDB 502	1272.929	0.0073	1.1157	0.0263	0.00044	0.00001
3	NDB 503	1272.961	0.0066	1.0819	0.0237	0.00042	0.00001

Table 4.14 compares the scan data for the three different environmental conditions. This table shows the spread of both the resonant frequencies and half-power bandwidths determined from the three scans for each of the modes together with the average of the standard errors for these parameters for the three scans of each mode. With data for only three scans for each mode it is not possible to draw conclusions which are highly quantitative. The variation from one scan to another is such that meaningful statistics would require presentation of data from a much larger number of scans for each mode. Nevertheless, there is a very significant difference between the data obtained under conditions A and that obtained under the other two conditions. The fluctuation in the resonant frequencies between scans and the standard errors of the fits are very much greater for conditions B and

Table 4.13: Vibration parameters obtained from Lorentzian fits to the scan data of Modes 1-5 under conditions C

No.	File name	Frequency f_0 , Hz	Std error δf_0 , Hz	Width γ , Hz	Std. error $\delta\gamma$, Hz	Damping factor, ζ	Error $\delta\zeta$
Mode 1							
1	NDB75	22.4962	0.0011	0.0700	0.0037	0.00156	0.00008
2	NDB77	22.4973	0.0006	0.0672	0.0020	0.00149	0.00004
3	NDB79	22.4964	0.0009	0.0628	0.0029	0.00140	0.00006
Mode 2							
1	NDB69	140.9435	0.0028	0.2614	0.0079	0.00093	0.00003
2	NDB71	140.9085	0.0016	0.1864	0.0056	0.00066	0.00002
3	NDB73	140.9303	0.0017	0.1512	0.0057	0.00054	0.00002
Mode 3							
1	NDB64	394.0146	0.0037	0.5591	0.0143	0.00071	0.00002
2	NDB67	393.9929	0.0012	0.4426	0.0039	0.00056	0.00000
3	NDB69	394.0236	0.0016	0.4693	0.0054	0.00060	0.00001
Mode 4							
1	NDB41TD	771.8552	0.0108	0.8522	0.0362	0.00055	0.00002
2	NDB42TD	771.8525	0.0101	0.8549	0.0338	0.00055	0.00002
3	NDB43TD	771.8550	0.0052	0.7460	0.0172	0.00048	0.00001
Mode 5							
1	NDB51TD	1274.746	0.0125	1.0140	0.0436	0.00040	0.00002
2	NDB52TD	1274.791	0.0224	1.2220	0.0843	0.00048	0.00003
3	NDB53TD	1274.891	0.0102	0.9500	0.0332	0.00037	0.00001

C than they are for conditions A. This is particularly so for the lower frequency modes. The data does not support a significant difference between conditions B and C although visual observations of the fluctuations in amplitude of the real-time FFT displays on an oscilloscope, suggested that the vibration data for conditions C were in fact very much less stable than that of conditions B. The fitted resonance frequency and standard errors in these fits are dependent on just how much the environmental noise affects the signals during the times of the scans. Clearly, for a given environmental noise condition, the fluctuations between the fits and the standard errors could be reduced if the signal-to-noise was increased by increasing the thermoelastic excitation (using a higher power modulated laser). Thus the data presented in Tables 4.07, 4.12 and 4.13 are merely representative of what can be

achieved under typical environmental conditions with low power laser diode excitation. Hence it was not considered necessary to try to present statistically-significant data.

For conditions A, it was found that decay time measurements by waveform sampling (and fitting of a damped sinusoid) were more sensitive to signal-to-noise than were the scan measurements. Thus such decay data could only be presented for the two lowest order modes which had the highest signal-to-noise ratios. Under conditions B and C, it was not possible to obtain decay time data in this way as the waveforms were simply not sufficiently stable. Similarly, reasonable fits of the decay envelope which were carried out for 3 modes under conditions A were also not possible under conditions B and C.

Table 4.14: Comparison of vibration data obtained from scans under conditions A, B and C (Tables 4.07, 4.12 and 4.13)

M No	Resonance frequency						Half power bandwidth					
	$f_{max}-f_{min}$, Hz			Std. error, Hz			$\gamma_{max}-\gamma_{min}$, Hz			Std. error, Hz		
	A	B	C	A	B	C	A	B	C	A	B	C
M1	0.0008	0.0102	0.0011	0.0003	0.0009	0.0009	0.0087	0.0272	0.0036	0.0011	0.0032	0.0029
M2	0.0038	0.0259	0.0350	0.0004	0.0011	0.0020	0.0032	0.0087	0.1102	0.0015	0.0042	0.0064
M3	0.0179	0.0363	0.0307	0.0013	0.0028	0.0022	0.0645	0.0623	0.1165	0.0044	0.0097	0.0079
M4	0.0516	0.1053	0.0827	0.0026	0.0073	0.0087	0.0475	0.1453	0.1089	0.0091	0.0267	0.0291
M5	0.0260	0.0800	0.1450	0.0048	0.0072	0.0150	0.0264	1.1115	0.2720	0.0170	0.0258	0.0682

4.4 Measurements with increased damping

Results presented so far have all been for very high Q resonances with very low damping factors. Damping factors and half-power bandwidths for Mode 1- have been of the order of 0.0014-0.0016 and of 0.06-0.07 Hz respectively. With a

recording FFT bandwidth of the DSA of 0.012 Hz, 5-6 data points can be measured within the half-power bandwidth of the displacement response curve for Mode 1. In order to see the effect of increased loss and also an increase in the bandwidth to resolution ratio, measurements were also made with rubber pads inserted between the cantilever and the jaws of the clamp. Two sets of measurements were made with different clamping tension. The effect of reducing the clamping tension is to increase the loss since the rubber is then less rigid. In the data presented below, the two sets of data are labelled R1 and R2, with R2 representing the more lossy mounting arrangement.

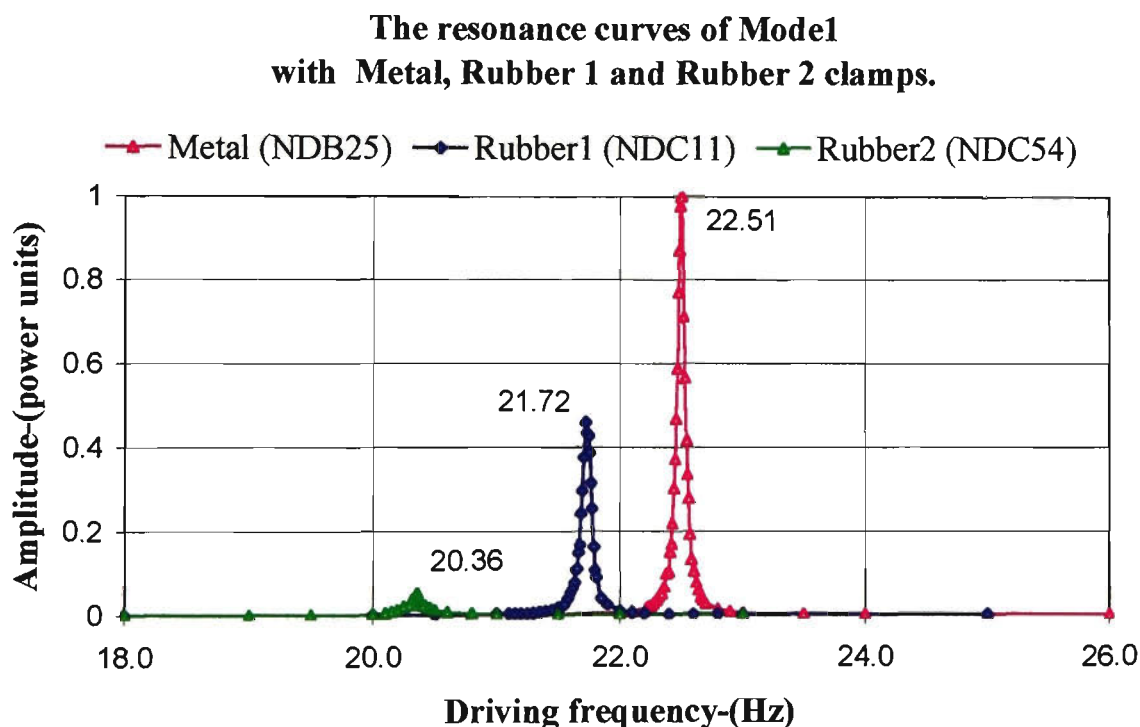


Figure 4.15: Mode 1 resonance (power) for a 300 mm aluminium cantilever using a metal clamp and also with the inclusion of rubber pads under different clamping tension (R1 and R2)

Figure 4.15 shows the effect of the rubber pads on the resonance. This figure shows three separate scans through the mode 1 resonance. All scans were done under conditions A. From right to left, these scans correspond to a metal clamp

(similar to previous condition A data), R1 and R2. The shift in resonant frequency and the decrease in vibration amplitude (power) is very evident from this figure. The amplitude changes are shown in the figure and these have implications for the signal to noise of the measurements. The frequency shifts were about 0.8 Hz for R1 and 2.2 Hz for R2.

For both R1 and R2, data was recorded using both the scan method and also using a damped harmonic fit to decay data. Table 4.15 shows the scan-derived data for the cantilever with rubber R1 included in the clamp arrangement. Tables 4.16 and 4.17 show the decay-derived data with rubber R1 and the damping and half-power

Table 4.15: Vibration parameters obtained from a Lorentzian function fit to the experimental response data for modes 1-5 with rubber pads in clamp (R1)

No.	File name	Frequency f_0 , Hz	Std. error δf , Hz	Width γ , Hz	Std. error $\delta \gamma$, Hz	Damping factor, ζ	Error $\delta \zeta$	Ampl., V
Mode 1								
1	NDC6	21.7250	0.0008	0.0886	0.0027	0.00204	0.00006	1.93
2	NDC8	21.7253	0.0004	0.0810	0.0015	0.00186	0.00003	1.93
3	NDC9	21.7229	0.0009	0.0883	0.0033	0.00203	0.00008	1.89
Mode 2								
1	NDC11	136.1593	0.0022	0.4841	0.0074	0.00178	0.00003	1.35
2	NDC12	136.1687	0.0017	0.4984	0.0059	0.00183	0.00002	1.35
3	NDC15	136.1724	0.0022	0.4810	0.0077	0.00177	0.00003	1.41
Mode 3								
1	NDC18	380.9964	0.0067	1.4907	0.0274	0.00196	0.00004	0.11
2	NDC20	380.9777	0.0087	1.5750	0.0365	0.00207	0.00005	0.12
3	NDC21	380.9603	0.0159	1.2830	0.0623	0.00168	0.00008	0.12
Mode 4								
1	NDC4A	746.9408	0.0457	3.2201	0.1959	0.00216	0.00013	0.04
2	NDC4B	746.9359	0.0490	3.1152	0.2088	0.00209	0.00014	0.04
3	NDC4C	747.2804	0.0465	3.2936	0.2024	0.00220	0.00014	0.05
Mode 5								
1	NDC5A	1234.9835	0.0924	6.1058	0.3898	0.00247	0.00016	0.08
2	NDC5B	1234.6955	0.0355	6.7116	0.1629	0.00272	0.00007	0.08
3	NDC5C	1234.4301	0.0393	6.6184	0.1767	0.00268	0.00007	0.07

Table 4.16: Decay time and resonance frequency determined from fitting an equation of the form $y = a + be^{-t/\tau} \sin(\omega_d t + \phi)$ to recorded decay waveforms, (R1)

No	File name	Decay time τ , s	Std.error $\delta\tau$, s	Resonance frequency f_d , Hz	Std.error δf_d , Hz
Mode1					
1	NXN1R	3.7469	0.0155	21.7316	0.0002
2	NXN2R	3.3994	0.0140	21.7317	0.0002
Mode2					
1	NXN3R	0.6794	0.0021	136.1642	0.0005
2	NXN4R	0.6691	0.0014	136.1633	0.0005
3	NXN5R	0.6815	0.0010	136.1637	0.0003

Table 4.17: Calculated values of damping factor and half-power bandwidth using the data of Table 4.16, (R1)

No	File name	Resonance frequency f_d , Hz	Std.error δf_d , Hz	Damping factor, ζ	Error, $\delta\zeta$	Half-power bandwidth γ , Hz	Error, $\delta\gamma$, Hz
Mode 1							
1	NXN1R	21.7316	0.0002	0.00195	0.000008	0.0850	0.0004
2	NXN2R	21.7317	0.0002	0.00215	0.000009	0.0936	0.0004
Mode 2							
1	NXN3R	136.1642	0.0005	0.00172	0.000005	0.4685	0.0010
2	NXN4R	136.1633	0.0005	0.00175	0.000004	0.4757	0.0010
3	NXN5R	136.1637	0.0003	0.00172	0.000003	0.4671	0.0007

Table 4.18: The vibration properties obtained from Lorentzian function fit to the experimental response data, Modes 1-5, (R2)

No.	File name	Frequency f_0 , Hz	Std. error δf , Hz	Width γ , Hz	Std. error $\delta\gamma$, Hz	Damping factor, ζ	Error $\delta\zeta$	Ampl., V
Model1								
1	NDC53	20.3637	0.0024	0.1409	0.0089	0.00346	0.00022	0.835
2	NDC54	20.3477	0.0035	0.1362	0.0124	0.00335	0.00030	0.638
3	NDC55	20.3405	0.0044	0.1658	0.0165	0.00408	0.00041	0.504
Mode 2								
1	NDC41	127.0954	0.0107	1.3478	0.0435	0.00530	0.00017	0.170
2	NDC43	127.1267	0.0158	1.4829	0.0657	0.00583	0.00026	0.197
3	NDC45	127.1039	0.0158	1.4585	0.0654	0.00574	0.00026	0.176
Mode 3								
1	NDC49	356.9241	0.0228	3.6094	0.0966	0.00506	0.00014	0.049
2	NDC51	357.1066	0.0381	4.822	0.1639	0.00675	0.00023	0.036
3	NDC52	357.0961	0.0255	4.7046	0.1082	0.00659	0.00015	0.039

Table 4.19: The decay time and resonance frequency obtained from the transient term $y = F_1 e^{-\zeta \omega_0 t} \sin(\omega_d t + \phi)$ fit to recorded waveforms, (R2)

No	File name	Decay time τ , s	Std.error $\delta\tau$, s	Resonance frequency f_d , Hz	Std.error δf_d , Hz
Mode1					
1	NXN11	1.7841	0.0058	20.3605	0.0003
2	NXN12	1.6872	0.0093	20.3595	0.0005
3	NXN4*	1.7874	0.0138	20.3951	0.0007
Mode2					
1	NXN2*	0.2602	0.0014	127.873	0.0034
2	NXN1*	0.2451	0.0023	127.910	0.0061

Table 4.20: The calculated values of damping factor and half-power bandwidth using the parameters from the transient function $y = F_1 e^{-\zeta \omega_0 t} \sin(\omega_d t + \phi)$ fit to waveform record, Modes 1-2, (R2)

No	File name	Resonance frequency f_d , Hz	Std.error δf_d , Hz	Damping factor, ζ	Error, $\delta\zeta$	Half-power bandwidth γ , Hz	Error, $\delta\gamma$, Hz
Mode 1							
1	NXN11	20.3605	0.0003	0.00438	0.00001	0.1784	0.0006
2	NXN12	20.3595	0.0005	0.00463	0.00003	0.1887	0.0010
3	NXN4*	20.3951	0.0007	0.00437	0.00003	0.1781	0.0014
Mode 2							
1	NXN2*	127.873	0.0034	0.00478	0.00003	1.2233	0.0066
2	NXN1*	127.910	0.0061	0.00508	0.00005	1.2987	0.0122

bandwidth calculated from this data. Tables 4.18, 4.19 and 4.20 show similar data for rubber R2 included in the clamp. Table 4.21 compares the above data for the three cases (A, R1 and R2). It can be seen that the γ values are larger for R1 and R2 as are the standard errors of the fits. The γ values increase with mode frequency but for the cases where the rubber is included this increase is faster than it is with the data obtained using the metal clamp (A). Similar trends can be seen with the values of the damping factor (ζ) in the tables. ζ decreases with mode frequency for the metal-clamped data, is approximately constant with mode frequency for the R1 data and is increasing with mode frequency for the R2 data.

The frequency shifts observed with the introduction of the rubber are very large. These values can be seen from the tables and for mode 1 are clearly shown in Figure 4.18. For mode 1, the change in frequency from metal clamp to R1 was about 0.8 Hz and from metal clamp to R2 was about 2.15 Hz. These shifts are far too large to be accounted for by damping changes. Using Eq. 2.50 and the ζ values from the tables, these shifts would be expected to be about 0.00005 Hz for metal-R1 and 0.0002 Hz for metal-R2. These measured shifts are probably due to a change in effective length of the cantilever when supported in the rubber mountings. The use of rubber in the jaws of the chuck would tend to shift the zero displacement point of the cantilever (effective clamp point) away from the edge of the metal jaws (the clamp position without rubber). A calculation of the change in clamp point required to produce the measured frequency shifts gives about 9.8 mm for the effective length change produced by the change in clamp tension between

Table 4.21: Comparison of half power bandwidths and standard errors for vibration data using metal (A) and rubber (R1 and R2) clamps. All data was obtained under Conditions A

No	Half power bandwidth (average) γ , Hz					Std. error, Hz					
						Resonance frequency			HPBW		
	Metal (A)	R1	A-R1 %	R2	A-R2 %	A	R1	R2	A	R1	R2
M1	0.0710	0.0860	21	0.1476	>207	0.0004	0.0007	0.0034	0.0012	0.0025	0.0126
M2	0.2147	0.4878	127	1.4297	>665	0.0004	0.0020	0.0141	0.0015	0.0070	0.0582
M3	0.4364	1.4496	232	4.3786	>1000	0.0013	0.0104	0.0288	0.0044	0.0420	0.1229
M4	0.6814	3.2096	371			0.0026	0.0471		0.0091	0.2024	
M5	0.8682	6.4786	646			0.0048	0.0557		0.0170	0.2432	

R1 and R2 (these points were chosen for the calculation as the cantilever arrangement was not otherwise disturbed between these two settings). This shift in effective clamp point is also surprisingly large but the same value is obtained using the frequency data for each mode and so the data are certainly consistent with this interpretation.

For the rubber-clamped data, as with previous results, decay time measurements can only be successfully carried out with the lowest frequency modes. With the reduction of vibration amplitude, which accompanies the increased loss, the signal-to-noise ratio is such that it has been possible to use the direct decay time measurement technique only with the two lowest order modes. The results obtained with the decay data for these two modes give quite similar ζ values to the scan data but the standard error in individual fits is lower. The spread in values from one measurement to another is similar for decay and scan techniques.

4.5 Summary

The results presented in this chapter have demonstrated that a moderately large structure, such as a 300 mm cantilever, can be excited to vibrate thermoelastically using a low power laser diode source. The optical fibre interferometer has been successfully used to remotely monitor these vibrations so that the whole excitation and sensing system involves no physical contact with the structure. Experiments have been conducted to determine the accuracy with which the various vibration parameters (resonant frequency, half power bandwidth and damping factor) can be measured for the purposes of modal analysis. A number of different measurement

techniques have been assessed and their performance with lightly-damped structures quantified.

The basic measurements were carried out using very high Q resonances under quiet nighttime conditions and it was shown that resonant frequency measurements give the smallest fractional errors and are the most suitable measurements for detecting small changes in resonance conditions. Measurements were carried out under conditions where the temperature of the structure was not controlled and it was found that small changes in ambient temperature had a significant effect on the resonant frequency. Thus very accurate measurements of vibration parameters require careful control of the temperature of the structure.

The effects of environmental noise on the accuracy with which vibration parameters can be determined was assessed by carrying out the measurements under a range of environmental conditions typical of those found within a laboratory environment. Finally some measurements were carried out with increased damping to show the effects of increased loss on the technique.

Chapter 5

CONCLUSION

Content:	Page
5.1 Conclusion.....	5-2

5.1 Conclusion

The objectives of the work described in this thesis were outlined in Chapter 1. Basically, these were to:

- Construct an optical system suitable for making very accurate and sensitive non-contact measurements of modal frequencies and other modal oscillation parameters of transverse mechanical vibrations in small to medium size structures.
- Investigate the advantages and disadvantages of alternative ways of making measurements of modal oscillation parameters which can be used to characterise the structure.
- Determine the accuracy with which the system can make measurements of the modal oscillation parameters. A high-Q resonant structure was required for these measurements so that the parameters being measured would be reasonably sharply defined.
- Determine the origin of the effects which are responsible for the ultimate limitation to the measurement accuracy.

All these objectives have been achieved. The optical fibre interferometer was actively stabilised using a PZT modulator and achieved an RMS NED of 0.17 nm in a 200 kHz bandwidth. This NED figure could be improved by reducing the bandwidth but such a change was not necessary for the present measurements as

the sensitivity was more than adequate. The interferometer performance could also be improved by using a high power laser light source to increase the signal. This was not attempted as it was felt more important to assess the performance which could be achieved with a small and relatively inexpensive system.

The structure used in the study was a clamped-free aluminium cantilever of dimensions 300 mm x 12 mm x 2.5 mm. This was mounted in a large steel vice which was solidly bolted to a concrete table which could be isolated from building vibrations with the use of rubber tubes under the legs. The overall cantilever structure had very low loss and Q factors in the range of about 350 - 1500 for the various modes. The temperature of the cantilever was not controlled and was subject to ambient temperature variations in the laboratory. The cantilever arrangement was such that it could be substantially isolated from air current movements using a covering box.

Measurements were made using the first 5 transverse vibrational modes of the cantilever at frequencies between 22.5 Hz and 1275 Hz. These measurements were affected by environmental noise and the effect of this was evident from measurements conducted under three sets of environmental conditions which corresponded to "quiet", "intermediate" and "noisy" laboratory situations. Measurements were also conducted with slightly more lossy mountings (lower Q) involving rubber sandwiched between the metal clamp and cantilever. Even with the lower Q, all measurements were conducted in the low-loss lightly-damped regime ($\zeta < 0.1$).

Vibration measurements were made in two different ways:

- The first involved scanning the excitation through resonance and measuring the resonance response as a function of excitation frequency (scan-based method). With this method some averaging was possible at each frequency to reduce the effects of environmental noise. The resonant frequency and its standard error are obtained from a Lorentzian fit to the power resonance curve.
- The second involved excitation of steady-state structural vibration at the resonant frequency followed by free decay after the excitation was removed (decay-based method). This permitted measurement of the decay time by fitting an exponential to the decay envelope. Alternatively, measurement of both the damped oscillation frequency and the decay time was possible by fitting a damped sinusoid to the recorded decay waveform.

Whatever the method of making the measurement, the vibrating structure was finally characterised by the resonant frequency and/or a loss parameter. This latter parameter depended on the type of measurement being conducted and was either the half power bandwidth for scan-based measurements or decay time for decay-based measurements. In either case the measured parameter could be converted to a damping factor (ζ). Any calculation of ζ requires a knowledge of the resonant frequency and hence the accuracy of ζ is limited by the accuracy of the resonant frequency determination. This limitation does not apply if the bandwidth or decay time is used directly as loss parameters.

The best performance of the system is obtained under "quiet" environmental conditions. Despite the fact that the excitation efficiency decreased by about a factor of 50 as the LD modulation frequency was increased to tune to different modes, the resonant frequency could be determined to an accuracy of about $3 - 10 \times 10^{-6}$ for all modes using the data from a single scan. No significant difference in fractional uncertainty can be discerned between the modes since the excitation conditions were not identical for all modes. There was however a significant variation in modal resonant frequency measured in consecutive scans of a particular mode. This difference which was generally about 10 times greater than the standard error of the resonant frequency determined from a single scan. This difference was ascribed to ambient temperature fluctuations of less than $0.5\text{ }^{\circ}\text{C}$ between scans. This lack of temperature control of the vibrating structure and exposure to ambient temperature fluctuations turned out to be the major factor which limited the accuracy of measurements of all vibration parameters. The fractional error for the half power bandwidth obtained from a single scan was only about 10^{-2} and hence this parameter can not be determined with an accuracy which is even close to that which can be obtained for the resonant frequency. Hence if one is trying to sense small changes in resonance parameters as a means of detecting changes in the structure under investigation, then resonant frequency is the best parameter to measure. Under quiet environmental conditions, the scan method can be used for all 5 modes with similar accuracy. However, the signals are much stronger for lower frequencies and so in general it is probably preferable to use the first few modes for scan measurements.

Decay time measurements had the advantage that they could be carried out much more simply and quickly than scan ones. However they were much more sensitive to the signal-to-noise ratio of the data as no averaging was possible. Even under quiet conditions, only three modes could be measured using the envelope method and two using the damped sinusoid fit. When the method could be used, the accuracy of the decay time was about 1% for the envelope method and about 0.2% for the damped sinusoid fit. The damped frequency could be measured to about $1 - 5 \times 10^{-6}$ in the latter case but interpretation of this as the resonant frequency depended on careful adjustment of the LD modulation to the centre of the resonance before the measurement was made. Any measurement of decay time requires first a reasonable knowledge of the resonant frequency so the LD modulation can be adjusted so that significant amplitude vibrations are obtained. To the extent that ζ varies slowly with frequency, the need for an accurate resonant frequency is reduced if one is calculating ζ .

Under conditions where there is greater environmental noise, the fractional errors in the measurements becomes larger and so the measurements are a less sensitive indicator of the state of the structure under investigation. Reliable decay measurements were not possible under conditions B and C. Scan measurements were still possible for all modes. With increasing loss, the amplitude of the vibrational resonance decreased sharply. Hence useful measurements of more heavily-damped structures require the use of lower order modes and also possibly higher power diode laser excitation (or excitation with other lasers). When all factors are considered, the first couple of modes are the most suitable for practical resonance measurements.

The most significant limitation to the accuracy of measurements is ambient temperature fluctuations. Temperature control of the structure is possible but the attachment of electrical elements for this purpose may affect the resonances being measured and runs counter to the philosophy of making fully remote measurements. Control of the temperature of the environment is possible but the accuracy, which can be achieved, is often limited in practical situations. For the present structure, the basic reason for the temperature sensitivity is due to a change in stiffness caused by the temperature variation of the Young's modulus. This effect is calculated to produce a change in resonant frequency of about $0.03\% \text{ } ^\circ\text{C}^{-1}$ for all modes.

This technique can clearly be used for remote NDT applications within the limitations pointed out above. The actual limitations depend on the nature of the structure and the environment. Structures with high frequency resonances or those with higher loss resonances are more difficult to excite and will in general have poorer signal-to-noise ratios for the measurements. Similarly, use of the technique is more difficult in noisy environments. In very noisy environments it may be that there is sufficient environmental excitation of the resonance modes to allow some measurements without LD excitation although such measurements are likely to have relatively poor accuracy. Measurements with less ideal structures or in very noisy environments would benefit from higher power laser sources for the interferometer and for excitation.

LIST OF SYMBOLS

α_E	temperature coefficient
α_t	thermal expansion co-efficient
α_s	absorption coefficient
A	cross sectional area
β_n	dimensionless parameter ($\beta_n = k_n L$)
β	homodyne efficiency
$\gamma = \omega_2 - \omega_1$	half power bandwidth
γ_f	fringe visibility
Γ	surface reflectivity
δ	penetration depth of the light
δ_s	skin depth
δ_t	logarithmic decrement
ϵ	dielectric constant
ϵ_r	responsivity of a photodetector
$\epsilon_s(\chi)$	thermal strain
ζ	damping factor
η	loss factor
Θ	angle between two polarisation vectors
k	stiffness constant
λ	wavelength
$\mu = \rho A$	mass per unit length of a beam

$\Delta\nu$	source mode spacing
ρ	mass density
σ_n	dimensionless parameter
τ	decay time
τ_c	source coherence time
χ	distance from the mid-plane
ϕ_n	phase angle
ϕ_c	control phase shift
ϕ_d	thermal phase shift
ϕ_s	signal phase amplitude
$\Delta\phi$	phase angle change
ω_{c0}	circular frequency of the light
ω_{0n}	natural circular frequency
ω_d	damped natural circular frequency
ω_f	forced circular frequency
ω_s	signal modulation frequency
A_n	generalised amplitude
b	dimension, width of a beam
B_{1n}, B_{2n}	general constants
c	damping constant
c_c	critical damping constant
c	velocity of light
C_{1n}, C_{2n}	general constants
d_p	piezoelectric co-efficient

E	Young's (Elasticity) modulus
E_s	signal output of interferometer
E_r	reference output of interferometer
\mathbf{E}	energy
$\Delta\mathbf{E}$	stored energy
f_c	characteristic frequency
f_n	frequency of n^{th} mode
$F_n, F(x)$	force
F_0	force amplitude
g	amplifier gain
h	dimension, thickness of a beam
i	output current
$I(t), I_{max}$	surface irradiance
I_r	moment of inertia of area
I, I_1, I_2	output intensity
I_0	initial output intensity
$J_n(\phi_s)$	Bessel function of order n
k	thermal diffusivity
K	thermal conductivity
K_1, K_2	power coupling coefficients
L, l	length of a beam
L_c	source coherence length
L_r	optical path length of the reference arm
L_s	optical path length of the signal arm
ΔL_t	linear thermal expansion

$\Delta L=L_r-L_s$	optical path length difference
m	mass
$M(t)$	bending moment
N_o	force amplitude reference
n	refraction index
$p(x,t)$	force, function of position and of time
$P(t)$	force, function of time only
$P(x)$	force, function of position only
$P(\chi)$	force as a function of distance from the mid-plane
Q	quality factor
r, r_s	radius
r	frequency ratio $r=\omega/\omega_0$
$R(\omega)$	response function
S	mirror displacement amplitude
t	time
t°	temperature (C°)
T°	temperature (K°)
$T(\chi)$	temperature as a function of distance from the mid-plane
ΔT	temperature change
$U(x,y,z,t)$	heat function
$V(t)$	output voltage signal
V_a	interferometer peak signal
V_b	reduced interferometer signal
V_c	correction signal

V_s	shear force
dV_{fb}	feedback control signal
$w(t)$	normalised laser pulse shape
$y(t)$	displacement as function of time
\dot{y}	velocity
\ddot{y}	acceleration
$y_i(t)$	transient vibration term
$y_f(t)$	forced vibration term
$Y(x)$	displacement as function of position only
$\tilde{Y}(x, t)$	displacement as a function of position and of time

REFERENCES

- Aamodt, L. C. and Murphy, J. C. 1982. Effect of 3-D heat flow near edges in photothermal measurements. *Applied Optics*, 21: 111 - 115
- Adams, R. D. and Bacon, D. G. C. 1973. Measurement of flexural damping capacity and dynamic Young's modulus of metals and reinforced plastics. *Journal of Physics D: Applied Physics*, 6: 27 - 41
- Adams, R. D. and Coppendale, J. 1976. Measurement of elastic moduli of structural adhesives by a resonant bar technique. *Journal of mechanical engineering science*, 20: 93 - 100
- Alexander, J. C. and Nurmikko, A. V. 1973. Excitation of thin elastic membranes by momentum transfer of laser light. *Optics Communications*, 9: 404 - 406
- Allocca, J. A. and Stuart, A. 1984. *Transducers: Theory and Applications*. Reston Publishing Company, Inc., Virginia, USA
- Ameri, S., Ash, E. A., Neuman, V. and Petts, C. R. 1981. Photo-displacement imaging. *Electronics Letters*, 17: 337 - 338
- Andres, M. V., Foulds, K. W. H. and Tudor, M. J. 1986. Optical activation of a silicon vibrating sensor. *Electronics Letters*, 22: 1097 - 1099
- Aprahamian, R. and Evensen, D. A. 1970. Applications of holography to dynamics: high frequency vibration of plates. *Transactions of the ASME: Journal of Applied Mechanics*, 12: 1083-1090
- Askriba, S., Cussen, L. D. and Szajman, J. 1996. A novel technique for the measurement of stress in thin metallic films. *Measurement Science and Technology* 7: 939 - 943

- Barber, A. 1992. Handbook of noise and Vibration control. Elsevier Advanced Technology, Oxford
- Beards, C. F. 1981. Vibration Analysis and Control System Dynamics. Ellis Horwood Ltd., Chichester, England
- Bell, A.G. 1880. On the production and reproduction of sound by light. *American Journal of Science*, 20: 305-324,
- Blevins, R. D. 1979. Formulas for Natural frequencies and Mode shape. Van Nostrand Reinhold Company, N.Y., USA
- Bray, D.E. and McBride, D. (eds.) 1992. NDT techniques. John Wiley & Sons, Inc., N.Y., USA
- Buchhave, P. 1975. Laser Doppler vibration measurements using variable frequency shift. *DISA Information Bulletin*, 18: 15 - 20
- Carslaw, H. S. and Jaeger, J. C. 1959. Conduction of Heat in Solids. Clarendon Press, Oxford
- Charpentier, P., Lepoutre, F. and Bertrand, L. 1982. Photoacoustic measurements of thermal diffusivity description of the "drum effect". *Journal of Applied Physics*, 53: 608 - 614
- Chitnis, V. T., Kumar, S. and Sen, D. 1989. Optical fibre sensor for vibration amplitude measurement. *Journal of Lightwave Technology*, 7: 687 - 691
- Churenkov, A. V. 1993. Photothermal excitation and self-excitation of silicon microresonators. *Sensors and Actuators A*, 39: 141 - 148

- Crosbie, R. A., Dewhurst, R. J. and Palmer, S. B. 1986. Flexural resonance measurements of clamped and partially clamped discs excited by nanosecond laser pulses. *Journal of Applied Physics*, 59: 1843 - 1848
- Dakin, J. and Culshaw, B. (eds.) 1988. *Optical Fibre Sensors: Principles and Components* (v.1). Boston: Artech, USA
- Dakin, J. and Culshaw, B., (eds.) 1989. *Optical Fibre Sensors: Systems and Applications* (v.2). Norwood, MA: Artech, USA
- Dandridge, A. and Goldberg, L. 1982. Current induced frequency modulation in diode lasers. *Electronics Letters*, 18: 302 – 304
- Dandridge, A. 1991. *Fibre optic sensors based on the Mach-Zehnder and Mickelson Interferometers: Fibre Optic Sensors: An Introduction for Engineers and Scientists*. (Ed. by E. Udd), John Willey & Sons, Inc., N.Y., USA
- Dandridge, A., Tveten, A. B., Miles, R. O. and Giallorenzi, T. G. 1980. Laser noise in fibre-optic interferometer systems. *Applied Physics Letters*, 37: 526 – 528
- Dandridge, A. and Tveten, A. B. 1981. Noise reduction in fibre-optic interferometer systems. *Applied Optics*, 20: 2337 – 2339
- Deferrary, H. A. and Andrews, F. A. 1966. Laser Interferometric Technique for Measuring Small-Order Vibration Displacements. *Journal of Acoustic Society of America*, 39: 979 - 980
- Deferrary, H. A., Darby, R. A and Andrews, F. A. 1967. Vibration Displacement and Mode-Shape Measurement by a Laser Interferometer. *Journal of Acoustic Society of America*, 42: 982 - 990

- Dowling, N. E. 1993. Mechanical behaviour of materials: Engineering methods for deformation, fracture and fatigue. Prentice Hall, Inc., USA
- Duggan, T. V. 1964. Stress Analysis and Vibrations of Elastic Bodies. Heywood Book, London, UK
- Ewins, D. J. 1995. Modal Testing: Theory and Practice. Research Studies Press Ltd., England
- Greenwood, J. C. 1988. Silicon in mechanical sensors. *Journal of physics E: Scientific instruments*, 21: 1114 - 1128
- Hane, K. and Hattori, S. 1990. Photothermal bending of a layered sample in plate form. *Applied Optics*, 29: 145 - 150
- Hane, K., Hattori, S. and Kanie, T. 1988. Photothermoelastic probing for a clamped plate form. *Applied Optics*, 27: 386 - 392
- Hess, P. (ed.) 1989. Photoacoustic, Photothermal and Photochemical Processes at Surfaces and in Thin Films. Springer-Verlag Berlin Heidelberg, Germany
- Jackson, D. A. and Jones, D. C. 1989. Interferometers Optical Fibre Sensors: Systems and Applications. Vol.2, Artech House, USA
- Jackson, D. A., Dandridge, A. and Sheem, S. K. 1980. Measurement of small phase shifts using a single-mode optical-fibre interferometer. *Optics Letters*, 5: 139 - 141
- Jackson, D. A., Priest, R., Dandridge, A. and Tveten, A. B. 1980. Elimination of drift in a single-mode optical fibre interferometer using a piezoelectrically stretched coiled fibre. *Applied Optics*, 19: 2926 - 2929

- Jenkins, D. F. L., Cunningham, M. J., Clegg, W. W. and Bakush, M. M. 1995. Measurement of the modal shapes of inhomogeneous cantilevers using optical beam deflection. *Measurement Science and Technology*, 6: 160 - 166
- Jones, E. D. 1971. Ultrafast laser-induced stress waves in solids. *Applied Physics Letters*, 18: 33 - 35
- Jones, R. E., Naden, J. M. and Neat, R. C. 1988. Optical-fibre sensors using micromachined silicon resonant elements. *IEE Proceedings*, 135: 353 – 358
- Kalnins, A. and Dym, C. L. 1976. *Vibration Beams, Plates and Shells*. Dowden, Hutchinson & Ross, Inc., Stroudsburg, Pennsylvania, USA
- Karner, C., Mandel, A. and Trager, F. 1985. Pulsed laser photothermal displacement spectroscopy for surface studies. *Journal of Applied Physics A: Solids and Surfaces*, 38: 19 - 21
- Kaye, G. W. C. and Laby, T. H. 1973. *Tables of Physical and Chemical Constants*. Longman, London
- Koss, L. L. and Tobin, R. C. 1983. Laser induced structural vibration. *Journal of Sound and Vibration*, 86: 1 - 7
- Laming, R. I., Gold, M. P., Payne, D. N. and Halliwell, N. A. 1986. Fibre-optic vibration probe. *Electronics Letters*, 22: 167 - 168
- Lee, Y. H., Shin, Y. D. and Lee, K. H. 1994. Measurement of Young's moduli for film and substrate by the mechanical resonance method. *Journal of Applied Physics*, 75: 5913 – 5915
- Lewin, A. C., Kersey, A. D. and Jackson, A. D. 1985. Non-contact surface vibration analysis using a monomode fibre optic interferometer

- incorporating an open-air path. *Journal of Physics E: Scientific Instruments*, 18: 604 - 608
- Main, I.G. 1993. *Vibrations and Waves in physics*. Cambridge University Press, Cambridge, England
- McGonnagle, W. J. 1961. *Nondestructive testing*. McGraw-Hill Book Company, USA
- Nagy, K., Dousis, D. A. and Finch, R. D. 1978. Detection of flaws in railroad wheels using acoustic signatures. *Transactions of the ASME: Journal of Engineering for Industry*, 100: 459 - 467
- Nashif, A. D., Jones, D. I. G. and Henderson J. P. 1985. *Vibration damping*. John Wiley & Sons, Inc., USA
- Opsal, J. and Rosencwaig, A. 1982. Thermal wave depth profiling: Theory. *Journal of Applied Physics*, 53: 4240 - 4246
- Pain, H. J. 1993. *The Physics of Vibrations and Waves*. John Wiley & Sons, Chichester, England
- Pernick, B. J. 1973. Self-Consistent and Direct Reading Laser Homodyne Measurement Technique. *Applied Optics*, 12: 607 - 610
- Philips, G. J. 1992. Fibre Optics displacement sensors for dynamic measurements. *Sensors*, 9: 26 - 30
- Philp, W. R. and Booth, D. J. 1991. Laser excitation of transverse mechanical vibrations in structures. *Proceedings 'NDT' 91*, National Conference, August, Melbourne
- Philp, W. R. and Booth, D. J. 1994. Remote excitation and sensing of mechanical resonances in structures using laser diodes and an optical fibre

- interferometer. *Journal of Measurement Science and Technology*, 5: 731-735
- Philp, W. R., Booth, D. J. and Perry, N. D. 1993. A model for laser-induced excitation of vibrations in structures using intensities below the surface ablation threshold. *Proceedings Australian Conference on Laser Optics and Spectroscopy*, December, Melbourne
- Philp, W. R., Booth, D. J. and Perry, N. D. 1995. Single-pulse laser stimulation of structural vibration using power densities below the surface ablation threshold. *Journal of Sound and Vibration*, 185: 643-654
- Philp, W. R. 1993. Modal Analysis of Laser vibrated structures. Ph.D Thesis, Victoria University of Technology, Melbourne
- Ready, J. F. 1965. Effects Due to Absorption of Laser Radiation. *Journal of Physics*, 36: 462 - 468
- Ready, J. F. 1971. Effects of High-Power Laser Radiation. Academic Press, NY, USA
- Ready, J. F. 1974. Impulse produced by the interaction of CO₂ TEA laser pulses. *Applied Physics Letters*, 25: 558 - 560,
- Rosencwaig, A. and Gersho, A. 1976. Theory of the photoacoustic effect with solids. *Journal of Applied Physics*, 47: 64 – 69
- Rousset, G., Bertrand, L. and Cielo, P. 1985. A pulsed thermoelastic analysis of photothermal surface displacements in layered materials. *Journal of Applied Physics*, 57: 4396 – 4405

- Rousset, G., Lepoutre, F. and Bertrand, L. 1983. Influence of thermoelastic bending on photoacoustic experiments related to measurements of thermal diffusivity of metals. *Journal of Applied Physics*, 54: 2383-2391
- Scruby, S. B., Dewhurst, R. J., Hutchins, D. A. and Palmer, S. B. 1980. Quantitative studies of thermally generated elastic waves in laser-irradiated metals. *Journal of Applied Physics*, 51: 6210-6216
- Sheem, S. K., Giallorenzi, T. G. and Koo, K. 1982. Optical techniques to solve the signal fading problem in fiber interferometers. *Applied Optics*, 21: 689 – 693
- Sudarshanam, V. S. 1992. Minimum detectable phase shift in spectrum-analysis techniques of optical interferometric vibration detection. *Applied Optics*, 31: 5997 - 6002
- Timoshenko, S., Young, D. H. and Weaver, W.J. 1974. *Vibration problems in engineering*. John Wiley & Sons, Inc., USA
- Thomson, W. T. 1993. *Theory of vibration with applications*. Chapman & Hall, London, England
- Tudor, M. J., Andres, M. V., Foulds, K. W. H. and Naden, J. M. 1988. Silicon resonant sensors: interrogation techniques and characteristics. *IEE Proceedings*, 135: 364 – 368
- Udd, E. (ed.) 1991. *Fibre Optic Sensors: An Introduction for Engineers and Scientists*. John Wiley & Sons, Inc., NY, USA
- Vencatesh, S. and Culshaw, B. 1985. Optically activated vibrations in a micromachined silica structure. *Electronics Letters*, 21: 315 - 317
- Vierck, R. K. 1979. *Vibration Analysis*. Harper & Row, Publishers Inc., N.Y, USA

- Volterra, E. and Zachmanoglou, E. C. 1965. Dynamic of Vibrations. Charles E. Merrill Books, Inc, Columbus, USA
- Walsh, D. and Culshaw, B. 1991. Optically Activated Silicon Microresonator Transducers: an Assessment of Material Properties. *Sensors and Activators A*, 25-27: 711 - 716
- Walsh, D., Uttamachandani, D. and Culshaw, B. 1990. Optically activated microresonator sensors. *IEE Colloquium on 'Microsensors' (Digest No. 057)*, 4/1 – 6
- White, N. M. and Brignell, J. 1995. Excitation of thick-film resonant sensor structures. *IEE Proceedings: Science, Measurement and Technology*, 142: 244 – 248
- White, R. M. 1963. Generation of elastic waves by Transient Surface Heating. *Journal of Applied Physics*, 34: 3559 - 3567
- Xu, Y. and Nashif, A. 1996. Measurement, Analysis and Modeling of the Dynamic Properties of Materials, *Sound and Vibration* 7: 20 – 23
- Zhang, L. M., Uttamchandani, D. and Culshaw, B. 1989. Transient excitation of silicon microresonator. *Electronics Letters*, 25: 149 - 150